

A search for signatures of quasar evolution: Comparison of the shapes of the rest-frame optical/UV continua of quasars at $z > 3$ and $z \sim 0.1$ ¹

Olga Kuhn², Martin Elvis³, Jill Bechtold⁴, and Richard Elston⁵

ABSTRACT

For 15 bright ($V < 17.5$), high redshift ($z > 3$) quasars, we have obtained infrared spectra and photometry, and optical spectrophotometry and photometry, which we use to construct their spectral energy distributions (SEDs) from $\lambda_{rest} \sim 1285 - 5100\text{\AA}$. High resolution spectroscopy for 7 enable measurements of their continua shortwards of Ly α , and L' detections of 4 of these extend their SEDs redwards to $\lambda_{rest} \sim 7500\text{\AA}$. We examine the optical/UV continuum shapes, and compare these to those of a set of 27 well-studied low redshift ($z \sim 0.1$) quasars (Elvis et al. 1994a) which are matched to the high redshift ones in *evolved* luminosity.

Single power law fits to the average fluxes within a set of narrow, line-free, windows between 1285\AA and 5100\AA , but excluding the $2000 - 4000\text{\AA}$ region of the FeII+BaC ‘small bump’, are adequate for most of the objects.

For both the high and low redshift samples, the distributions of spectral indices, α_{ouv} ($F_\nu \sim \nu^{\alpha_{ouv}}$) span a wide range, with $\Delta\alpha_{ouv} \sim 1$. The cause of such diversity is investigated, and our analysis is consistent with the conclusion of Rowan-Robinson (1995): that it arises from differences in both the emitted continua themselves and in the amounts of intrinsic extinction undergone.

The mean (median) optical/UV spectral indices for the high and low redshift samples are $-0.36(-0.41)$ and $-0.32(-0.30)$, respectively. A Student’s *t*-test indicates that these do not differ significantly, and a K-S test shows likewise for the distributions. Assuming the optical/UV continuum derives from accretion, the similarity of the spectral indices at high and low redshift is inconsistent with models which interpret the statistical evolution as resulting from a single generation of slowly dimming quasars, and instead

¹Work reported here was based on observations obtained with the Multiple Mirror Telescope, a joint facility of the Smithsonian Institution and the University of Arizona and at CTIO and KPNO which are operated by the Association of Universities for Research in Astronomy Inc., under a cooperative agreement with the National Science Foundation as part of the National Optical Astronomy Observatories.

²Joint Astronomy Centre, 660 N. A‘ohoku Place, University Park, Hilo, HI 96720; e-mail: o.kuhn@jach.hawaii.edu

³Harvard-Smithsonian Center for Astrophysics, 60 Garden St., Cambridge, MA 02138; elvis@cfa.harvard.edu

⁴Steward Observatory, University of Arizona, Tucson, AZ 85721; jill@as.arizona.edu

⁵Department of Astronomy, University of Florida, Gainesville, FL 32611; elston@astro.ufl.edu

favors those involving multiple generations of short-lived quasars formed at successively lower luminosities.

A clear difference between the high and low redshift samples occurs in the region of ‘small bump’. The power law fit residuals for the low redshift sample show a systematic excess from $\sim 2200 - 3000\text{\AA}$; but this feature is weak or absent in the high redshift sample. Further study is needed to determine what is responsible for this contrast, but it could reflect differences in iron abundance or FeII energy source, or alternatively, an intrinsic turnover in the continuum itself which is present at low but not at high redshift.

Subject headings: quasars:general — galaxies: active, evolution

1. Introduction

It has been well established that the population of quasars undergoes strong evolution (Schmidt 1968, Schmidt & Green 1983, Marshall 1985, and others). However, not until the last 10-15 years, with the technological advances leading to larger or deeper surveys (*e.g.* AAT, Boyle, Shanks & Peterson 1988; LBQS, Hewett, Foltz & Chaffee 1995; Edinburgh quasar survey, Goldschmidt et al. 1992; HES, Wisotzki et al. 2000; 2dF, Boyle et al. 2000), has it been possible to probe the manner of evolution. A key development was the discovery of a break in the luminosity function (LF; Koo & Kron 1988, Boyle, Shanks & Peterson 1988, but see Hawkins & Véron 1993, 1995). By tracking this feature with redshift, it was determined that the evolution of the luminosity function (at least up to $z \sim 2$) was well described as pure luminosity evolution (PLE; Boyle, Shanks & Peterson 1988, Boyle et al. 1991). Results from later surveys indicated the need for a more complex model such as luminosity dependent density evolution (LaFranca & Cristiani 1997, Köhler et al. 1997, Goldschmidt & Miller 1998, Wisotzki 2000, but see Londish, Boyle & Schade 2000). But though the exact form of evolution may be uncertain, the general model is of positive luminosity evolution up to $z \sim 2$. At redshifts between 2 and 3, the evolution slows or stops (Boyle et al. 1991, Hewett, Foltz & Chaffee 1993), and at $z \gtrsim 3$ the number density declines (Warren, Hewett & Osmer 1994, Kennefick, Djorgovski & de Carvalho 1995, Schmidt, Schneider & Gunn 1995), perhaps signaling this as the initial epoch of quasar formation (Warren, Hewett & Osmer 1994). Pei (1995a), by extrapolating a model of the luminosity function evolution, projects the initial formation redshift to $z \sim 5.2 - 5.5$, though it may be significantly higher, as suggested by the spectrum of the recently discovered $z = 5.8$ quasar, SDSS1044-0125 (Fan et al. 2000).

One goal of these efforts to pin down the luminosity function evolution is a better understanding of the quasars’ physical evolution; but as yet, the questions of how quasars form and evolve, what triggers the activity and how long it lasts remain. Cavaliere et al. (1988) outlined three modes of quasar evolution which can explain the statistical luminosity evolution: first, the most direct interpretation assumes continuous evolution of a single generation over timescales long

compared to the Hubble time; second is recurrent activity of relatively short duration; and the third involves multiple generations of galaxies which undergo a brief active (quasar) phase. These are distinguished by their predictions for quasar activity or remnants of it in the nearby universe. The discoveries of massive dark objects or black holes in the centers of many nearby ellipticals (Richstone et al. 1998, Magorrian et al. 1998) argue against continuous evolution, which would predict a smaller fraction of these (Salucci et al. 1999).

Most of the physical evolution models proposed recently focus on the quasar phenomenon as a short-lived recurrent or single event (*e.g.* Haehnelt & Rees 1993, Haehnelt, Natarajan & Rees 1998, Siemiginowska & Elvis 1997, Haiman & Menou 1999, Cavalieri & Vittorini 1998, Kauffmann & Haehnelt 2000, though Choi, Yang & Yi 1999, 2000 also consider a single generation of long lived quasars). They combine theories of structure formation with those for energy generation in quasars, assuming the accretion disk paradigm (*e.g.* Shields 1979, Malkan & Sargent 1982). But these models are not well constrained: Tytler (1999) lists the diverse characteristics of several which can account for the luminosity function evolution. A needed constraint may come from the observed spectral evolution. Accretion disk models make specific predictions for the continuum shape as a function of black hole mass, M , accretion rate, \dot{M} ($\dot{m} = \dot{M}/\dot{M}_{Edd}$) and inclination of the disk axis to the line of sight (θ , $\cos\theta = 1$ is face-on), with the peak frequency determined by the disk temperature, which for optically thick/geometrically thin disks follows the relation: $\log T \propto \frac{1}{4} \log \dot{m}/M \propto \frac{1}{4} [\log(\dot{m}/M)_{\cos\theta=1} + 2.4(\cos\theta - 1)]$; (Sun & Malkan 1989, McDowell et al. 1991). Though the greatest changes in M and \dot{M} are expected for continuous evolution of a single generation, some change would also be consistent with the multiple generation models, since the factor ~ 50 drop in the characteristic luminosity between $z \sim 3$ and $z \sim 0.1$ implies some difference in the central engines of high and low redshift quasars.

We focus here on the optical/UV, where the ‘blue bump’ component, which contains 15-45% of the bolometric luminosity and is commonly interpreted as primary emission from an accretion disk (*e.g.* Shields 1979, Malkan & Sargent 1982, Sun & Malkan 1989, Laor & Netzer 1989), is prominent. To look for evidence of evolution in this region, we construct rest-frame optical/UV continua for a set of bright high redshift ($z > 3$) quasars and compare these with the continua of a set of 27 low redshift ($z \sim 0.1$) ones which were chosen from the ‘Atlas of Quasar Energy Distributions’ (Elvis et al. 1994a) to have *evolved* luminosities within the range spanned by the high redshift sample. The organization of this paper is as follows. The sample selection is discussed in §2, the observations and data reduction in §3 and §4, and the construction of the SEDs in §5. Power law fits to the rest-frame 1285 – 5100Å continua are made in §6, and the distributions of resulting spectral indices for the high and low redshift samples are examined and compared in §7. In §8 and §9, the continuum shape is analyzed in more detail: §8 discusses our searches for previously reported redshift and luminosity trends, and §9 focuses on deviations of the continuum shape from a power law in the UV and optical, particularly the 3000Å region. Finally, §10 lists the conclusions.

2. Sample Selection

We selected two samples of quasars with redshifts $z \sim 3$ and $z \sim 0.1$. Because of the need for IR spectra to determine accurate continua for the $z \sim 3$ quasars, and the relative scarcity of high redshift quasars bright enough to make the collection of such data feasible on 4-m class telescopes, we were forced to select the high redshift sample first. Our high redshift sample spans the range of $M_V = -27.5$ to -29.5 , which corresponds to $L/L^*(z) \sim 1 - 7$, where $L_*(z) = L_{*,o}(1+z)^k$ and the rate, $k = 3.15$ ($H_o = 50 \text{ km s}^{-1} \text{ Mpc}^{-1}$, $q_o = 0.5$) and normalization are what Boyle, Shanks & Peterson (1988) found best described the luminosity function (albeit for $z \lesssim 2.2$) constructed largely from their AAT survey. For comparison, the full range of $L/L^*(z)$ is approximately $\sim 0.05 - 25$ (Boyle et al. 1991).

Following the tracks of $L/L_* = 1$ and 7.4 to $z \sim 0.1$ delimits the absolute magnitude range $M_V = -22.75$ to -24.75 for a low redshift sample which matches the high redshift one in *evolved* luminosity. To minimize the number of new observations required, we selected the low redshift sample from a set of quasars for which Elvis et al. (1994a) had previously constructed radio to X-ray spectral energy distributions.

Several objects had to be discarded from the original samples because we were unable to obtain sufficient observations, or their data were of poor quality; so in the analysis, 15 high and 27 low redshift quasars were considered. Tables 1 and 2 list the properties of the quasars in the initial samples: radio-loudness, redshift, magnitude, α_{ox} , and selection method; and the final column indicates, by a \checkmark or X , those which were used or had to be rejected from the sample. In Figure 1, we plot the redshift-absolute magnitude distribution of the quasars in the final high and low redshift samples. Note that while the sample selection was made assuming $H_o = 50 \text{ km s}^{-1} \text{ Mpc}^{-1}$, $q_o = 0.5$, to be consistent with Boyle, Shanks & Peterson (1988), for the rest of the paper (*e.g.* when converting data to the rest frame) we adopt a different set of cosmological parameters: $H_o = 75 \text{ km s}^{-1} \text{ Mpc}^{-1}$, $q_o = 0.1$, which are intermediate between an open, old and closed, young universe. $\Lambda = 0$ is assumed throughout.

There is evidence that at redshifts greater than 2, evolution slows or stops (Boyle et al. 1991; Hewett, Foltz & Chaffee 1995, Warren, Hewett & Osmer 1994). This would make a smooth extrapolation of the $L \sim (1+z)^k$ evolution out to $z \sim 3$ invalid, and instead the curve would turn over, implying that the $z \sim 3$ sample spans yet higher values of L/L_* . The absolute magnitude range of a matching low redshift sample would then be 0.5 to 1 magnitude brighter. About 5-15 of the quasars in the sample that we chose would be too faint to satisfy this new constraint. However, selecting brighter quasars at low redshift is difficult since their low space density means there are few available.

Both the high and low redshift samples are inhomogeneous. Each is roughly evenly split between radio-loud and radio-quiet quasars and they contain quasars discovered in a variety of surveys: radio; UV excess; objective prism. A clear selection bias exists in the low redshift sample, which was drawn from ‘Atlas’ sample that is comprised of AGN with strong detections with *Einstein*

(Wilkes & Elvis 1987). The high redshift sample contains some of the brightest objects in the universe. One, Q1208 + 101, is a gravitational lens candidate (Maoz et al. 1992). The lens has not been detected, to $H \sim 20$ in NICMOS images (Léhar et al. 2000), but magnification of the luminosity by a factor from 1–22 is estimated from the distribution of Ly α absorption systems near the quasar (proximity effect; Bechtold 1994, Giallongo et al. 1999). None of the other high redshift sample quasars is considered a lens candidate, however Pei (1995b) suggests that from 8–80% (depending on the lens model assumed) of bright ($M_v < -30$) $z \sim 3$ quasars may be lensed and consequently, their apparent brightnesses enhanced. If true and a fraction of the high redshift sample quasars are indeed lensed, this would affect continuum shape-luminosity correlations, but not the primary goal to look for differences in the continuum shapes between $z > 3$ and $z \sim 0.1$. We eliminated quasars known to be highly variable and those classified as BALQSOS (except Q1426 – 015, whose optical spectrum published by Wilkes et al. (1999) does not show strong absorption), and aside from the biases toward strong X-ray emitters in the low redshift sample and extremely luminous quasars in the high redshift one, there is no other obvious bias in either sample.

3. Radio Observations

To ascertain the radio classification of the sample objects which were not obviously radio bright (*e.g.* discovered in a radio survey), we looked in the literature and in the 87GB catalog (Gregory & Condon 1991) which has a flux limit of 25 mJy. We observed the 9 sample quasars whose radio classifications were still not known at the VLA at 5 GHz and 1415 MHz in November 1992, and found all these to be radio quiet (radio loudness, $\mathcal{R} \equiv \log[S(5 \text{ GHz})/S(\lambda 1450)]$ and $\mathcal{R} > 1$ is radio loud, $\mathcal{R} \leq 1$ is radio quiet; Bechtold et al. 1994). Fluxes and upper limits for the 9 high redshift quasars observed at the VLA are listed in Table 3.

4. IR and Optical Observations

At $z \sim 3$, the $1\mu\text{m}$ to $\sim 1000\text{\AA}$ optical/UV ‘blue bump’ is redshifted to optical and infrared wavelengths. To determine its shape accurately, moderate resolution spectroscopy and broadband photometry are needed: the spectroscopic data to distinguish the continuum level in between the numerous broad emission lines, and the photometry to provide an absolute flux calibration. But near-IR observations still do not reach the rest-frame continuum redwards of $\sim 5500\text{\AA}$. To extend coverage of the ‘blue bump’ beyond that, we observed a subset of the sample at L'($3.4\mu\text{m}$) and N($10.6\mu\text{m}$). Because of the difficulty of these observations, we only obtained, at L', fluxes for 5 of the high redshift quasars and upper limits for another 5 and, at N, upper limits for 4.

In this section, we report on the observations and the procedures followed to reduce the data. Because of the number of different observing runs and instruments used, we summarize in Table 4 the information relevant to each: the telescope and instrument, the instrument configuration and

the typical integration times. Logs of the IR and optical spectroscopic observations are given in Tables 5 and 7; and Tables 6 and 8 list the results of the IR and optical photometry, respectively.

4.1. IR spectroscopy

We used three instrument/telescope combinations to obtain the moderate resolution ($R \sim 500 - 700$) near-IR spectra presented here. Table 4 lists the detectors, slit widths, gratings used and resolutions obtained. With two of the instruments, Fspec (Williams et al. 1993) and CRSP (Joyce, Fowler & Heim 1994), a single grating setting covered the entire J, H or K band, and with the third, OSIRIS (DePoy et al. 1993), a cross dispersing grism enabled the simultaneous acquisition of $1.1-2.5\mu\text{m}$ J, H and K spectra. The observing procedures with Fspec, CRSP and OSIRIS were generally similar. In each case, a series of short integrations (background limited in the case of CRSP and OSIRIS) was accumulated, with the object stepped a few arcseconds along the slit between each or every other one, either progressively (Fspec) or in an ABBA pattern (CRSP and OSIRIS). Total on-source integration times ranged from about 0.5-2 hours, with most between ~ 45 and 90 minutes (see Table 4). To enable adequate removal of atmospheric absorption, the observations of each quasar were bracketed by those of a bright star with a nearly featureless near-IR continuum (early A or late F or early G dwarf) and within $\sim 10^\circ$ of it. With CRSP and OSIRIS, the stars were stepped sequentially along the slit rather than being placed in just two positions as were the quasars. For calibration, dome flats were taken with the lamps on and off, to enable the subtraction of thermal radiation and the dark current, except in the case of Fspec, where only on-flats were obtained and then dark frames were taken to subtract from these.

We reduced the IR spectroscopic data using IRAF and following standard procedures. Reduction of the Fspec and OSIRIS data used IRAF scripts specifically written for these instruments. Each of the individual images was corrected for non-linear response on a pixel-by-pixel basis (OSIRIS and CRSP only), and then sky subtracted, using for sky either the average of the two images which bracketed it or the single image taken immediately before or after it but with the object spectrum on a different part of the array. The sky-subtracted images were then divided by the combined set of dark-subtracted flat fields. A residual bias, determined from an unexposed portion of the array was removed from the Fspec images. The values of bad pixels were replaced with those determined by interpolating over (CRSP and OSIRIS) or median combining (Fspec) neighboring pixels. Usually the sky subtraction did not remove all traces of sky emission, so this residual background was fit and subtracted.

The subsequent steps to extract, co-add and wavelength calibrate the one-dimensional spectra were carried out in a different order for the data from CRSP, OSIRIS and Fspec. The Fspec images were rectified to align the spatial axis along the rows and combined in sets of 4. Spectra were then extracted, wavelength calibrated using a sky spectrum extracted from the same set of images, and then all wavelength calibrated spectra of the same object were combined. CRSP spectra were extracted from each reduced image, then wavelength calibrated using the sky spectrum that was

extracted from the corresponding sky image within the aperture determined by the object. Next all the wavelength calibrated spectra for a given object were combined. Finally, with the cross-dispersed OSIRIS data, the images were sky- and residual background- subtracted, then the array regions containing the individual orders were extracted, flat-fielded, and rectified. The reduced subimages were combined, one-dimensional spectra optimally extracted from these, and wavelength calibration done using the OH lines in the spectra that were extracted from the sky images.

The spectroscopic standard stars were reduced in the same way as the quasars, though with CRSP and OSIRIS where the stars were stepped in several positions along the slit, a sky image was produced by median combining all the star integrations. The stellar spectrum extracted from the sky-subtracted, flat-fielded image was wavelength calibrated and then divided into the spectrum of the quasar for which it was taken, to remove telluric absorption lines and correct for spectral response. Before division, intrinsic absorption features in the standards, such as $\text{Pa}\beta$ at $1.28\mu\text{m}$ and $\text{Br}\gamma$ at $2.16\mu\text{m}$ were removed. Another feature, at $2.18\mu\text{m}$, was treated as intrinsic when reducing the Fspec and CRSP data, but for the later OSIRIS reductions, it was properly treated as atmospheric. The strength of this feature was comparable to the noise in the quasar spectra, and so removal of it did not significantly affect the spectra.

The quasar spectra were flux calibrated using the broad band IR magnitude of the standard star as determined from its V magnitude and the optical to IR color (Johnson 1966) corresponding to its spectral type. The stellar continuum shape was determined from its effective temperature (Johnson 1966) and removed from the final quasar spectrum.

4.2. IR photometry

We obtained the J, H, K and L' photometry presented in this paper using the single channel IR photometer at the MMT (Rieke 1984) and OSIRIS in imaging mode at the CTIO 4-meter. The observations at N were also made at the MMT, using the single channel IR bolometer (Keller, Sabol & Rieke 1990).

For all of the MMT photometer and bolometer observations, the secondaries were chopped at a frequency of 7.5 or 20 Hz, respectively, and the telescope was wobbled every 10 seconds to obtain a frequent sky measurements on either side of the source. The chop throw and wobble were both $15''$, except for one run where they were $10''$ (Table 6). The observations were continued until sufficient signal-to-noise was achieved, typically 30-40 minutes for the quasar, and 5 minutes for the standard star. Table 4 lists the aperture sizes, chop rates and throw (in place of grating and resolution) and typical integration times. The bolometer has just one aperture available, though the photometer has two — the choice for any given night depended on seeing conditions. The aperture used for each quasar is given in Table 6. For the observations with OSIRIS, we took series of 5 to 9 short (10 seconds times 3 co-adds) integrations between which the telescope was offset to position the object in a grid which covered the array. Dome flats and dark frames were not taken, but flat fields

were produced by median combining the all the science observations taken through the same filter and with similar integration times during the course of that night. The dark current could not be subtracted from these flats, but was negligible ($1 \text{ e}^- \text{ s}^{-1}$; Cooper, Bui & Bailey 1993).

The IR photometer and bolometer data were reduced in the same way. After each wobble, the instrument output the total background-subtracted counts, where the background was taken to be the average of the two bracketing sky observations. Instrumental magnitudes and errors were computed from the average sky-subtracted counts and the standard deviation in the average.

To reduce the images from OSIRIS, we first produced a blank sky image by median-combining all the images taken within a single grid sequence and rejecting pixel values which deviated significantly from the median. This sky image was then subtracted from each of the images in the sequence and the result was divided by the normalized flat field at the corresponding filter. Bad pixels were replaced with the value determined by interpolating over adjacent ones. Finally, all the reduced images from a single grid sequence were aligned and averaged together. Aperture photometry was done on the individual and combined images using a circular aperture with a 32 pixel ($12''$) diameter; and the mode of values within an annulus that was centered on the object and had a radius and width of 25 pixels was taken as a measure of the residual background and subtracted from the aperture flux.

To flux calibrate the data from the MMT IR photometer and OSIRIS, we observed stars from the lists of bright standards (Elias et al. 1982) and faint UKIRT standards (Casali & Hawarden 1992, Hawarden et al. 2001), respectively. To calibrate the N band bolometer data, we used β And, α Tau, α Cyg and μ Cep as standards (Tokunaga 1984; Rieke, Lebofsky & Low 1985). For all instruments, the instrumental magnitudes were converted to apparent magnitudes assuming extinction coefficients based on previous observing runs at the MMT (M. Rieke 1994, private communication): $k = 0.1 \text{ mag/airmass}$ at J, H and K and $k = 0.2 \text{ mag/airmass}$ at L', though $k = 0.08$ may be more appropriate for the CTIO data. We made no extinction correction to the data at N since we had no detections, only upper limits, at this band. No color transformations between the MMT and CIT systems were assumed except at J where, to account for the difference between the peak wavelengths of the transmission curves for the filter used by Elias and that used in the MMT photometer, the following correction was applied to the Elias magnitudes: $J_{MMT} = 1.006(J - K)_{Elias} + K_{MMT}$ (Willner et al. 1985). No color transformations between the UKIRT (to which the OSIRIS data were referenced) and the CIT systems were assumed. We placed the magnitudes on a flux scale using the following zero magnitude fluxes, also listed in Table 9: at J ($\lambda_o = 1.25\mu\text{m}$), $F_0 = 1603 \text{ Jy}$; H ($\lambda_o = 1.60\mu\text{m}$), $F_0 = 1075 \text{ Jy}$; and K ($\lambda_o = 2.22\mu\text{m}$), $F_0 = 667 \text{ Jy}$ (Campins, Rieke and Lebofsky 1985). At L' ($\lambda_o = 3.4\mu\text{m}$), the zero magnitude flux was taken to be 309.0 Jy, based on a blackbody fit to the spectrum of Vega (R. Cutri 1994, private communication) and at N ($\lambda_o = 10.6\mu\text{m}$), we assumed $F_0 = 36 \text{ Jy}$ (Rieke, Lebofsky & Low 1985).

4.3. Optical spectrophotometry

The optical spectrophotometry was obtained using four different instruments: the red channel spectrograph at the MMT; the Boller and Chivens spectrograph at the Steward Observatory 2.3-m; the FAST spectrograph (Fabricant et al. 1998) at the FLWO 1.5-m telescope; and the RC spectrograph at the CTIO 1.5 m telescope. Details of the various instrument set-ups, including slit widths, gratings, resolution, wavelength coverage, as well as the range of integration times, are given in Tables 4 and 7.

To reduce light losses, we used, for all of the objects, a 4-5" wide slit; for the MMT and Steward Observatory observations, it was oriented parallel to the atmospheric dispersion, though for those made at FLWO and CTIO it was always oriented E-W. With the MMT and Steward 2.3 m, a single 20-30 minute integration gave sufficient signal-to-noise; at the other telescopes, we obtained a set of 3 15-20 minute integrations which we median-combined to increase signal-to-noise and eliminate cosmic rays. An internal HeNeAr or HeAr lamp spectrum was obtained for each position. Spectrophotometric standards from Massey et al. (1988), Massey & Gronwall (1990) (except for the IIDS standard, EG 129; Oke 1974), and Hamuy et al. (1992), for the southern hemisphere observations, were observed frequently throughout the night and at a range of airmasses. Dome flats were taken during the day, and, at CTIO, twilight flats were also taken. Bias frames were obtained for each night. We reduced these data in IRAF following the usual procedures for bias subtraction, flatfielding, spectral extraction with background subtraction, and flux calibration.

4.4. Optical photometry

Optical photometry was obtained at the 1.2 m telescope at FLWO on Mt. Hopkins and the 0.9 m telescope at CTIO. The CTIO data were obtained in photometric conditions. There were cirrus or clouds during some of the observations made at the FLWO, as noted in Table 8, but we repeated the observations obtained in non-photometric conditions. During the course of the night, we observed groups of standard stars from Landolt (1992).

The images were reduced following the standard IRAF procedures. The data were flat-fielded using dome (FLWO and CTIO) and twilight flats (FLWO). Aperture photometry was done where the diameter of the circular aperture, 12 to 17", depending on the seeing, was chosen to include all the light yet not too much background noise. The same aperture size was adopted for all observations taken during the night. The sky counts were measured in an annulus centered on the object. The IRAF task *photcal* was used to convert instrumental to absolute magnitudes. It uses the standard star data to determine the extinction and color correction. For the October 1993 dataset, we did not include a color correction term in the transformation equations, but instead made a correction to the zero-magnitude fluxes at each filter, based on a comparison between an expected quasar spectrum (a power law, $f_\nu \sim \nu^\alpha$) and the convolved CCD response and filter transmission curves (sixth column of Table 9). Finally, we placed the magnitudes on a flux scale,

using the zero-magnitude fluxes in Table 9.

5. The Spectral Energy Distributions

This section describes the procedures followed to piece together the optical and IR data to produce rest-frame optical/UV spectral energy distributions. These consisted of (1) grey-scaling the IR and optical spectroscopy by constant factors to match the fluxes determined from our broad band photometry; (2) correcting the spectra for Galactic extinction and extinction in line-of-sight damped Ly α systems when present; and (3) correcting the continua at wavelengths shorter than redshifted Ly α for the numerous HI absorption lines, the ‘Ly α forest’. Additionally, some reconstruction of the rest-frame continua for the low redshift sample was necessary to make them consistent with those of the high redshift sample.

5.1. Scaling and correction for Galactic extinction

The observations of spectroscopic standards were not sufficient to flux calibrate the IR spectra. The slit was narrow ($1 - 2''$), so centering and maintaining standards and quasars in it was difficult and not uniformly done. Besides, conditions were sometimes not photometric. Therefore, we relied on our IR photometry to greyscale the spectra. The scaling factor was determined by dividing the photometric flux by the spectroscopic flux averaged over the corresponding J, H or K bandpass. Since the IR filter curves closely approximate a ‘tophat’ shape, averaging over the bandpass is not a bad representation of the convolution of the spectrum with the filter curve. Finally, each spectrum was flux calibrated by multiplying by the appropriate scaling factor. In the same way, the flux levels of our optical spectrophotometry were checked against the optical photometry and corrected when needed. The scaling factors are listed in Table 10.

All of the data were corrected for Galactic extinction, using the Galactic extinction curve (optical/UV — Savage & Mathis 1979, IR — Rieke & Lebofsky 1985) and gas to dust ratio of $4.8 \times 10^{21} \text{ cm}^2 \text{ mag}^{-1}$ (Savage & Mathis 1979). When possible, the Galactic column densities were taken from Elvis, Lockman & Wilkes (1989) and Murphy et al. (1996), who directly measured the column densities towards a number of the sample quasars to an accuracy of $< 10^{19} \text{ cm}^{-2}$. For the southern quasars or those otherwise not targeted by Elvis et al. or Murphy et al., we used column densities from the Bell Labs HI survey, which have typical uncertainties of $\lesssim 10^{20} \text{ cm}^{-2}$ (Stark et al. 1992). Table 11 lists the line-of-sight column densities for each of the high redshift sample quasars.

Three of the high redshift quasars: Q0000 – 263, Q0347 – 388 and Q1946 + 7658; have damped Ly α systems in the line-of-sight. There is evidence that these contain dust (Pei, Fall & Bechtold 1991, Carilli et al. 1998), so we corrected for extinction in these systems. Their metallicity and dust to gas ratios are assumed to be lower than Galactic (10%; Pei, Fall & Bechtold 1991), and

so to correct for reddening by these, we used the SMC extinction curve and a dust to gas ratio 10 times smaller than the Galactic value.

5.2. Correction for Ly α forest

Along a given line of sight, the number density of Ly α forest clouds increases with redshift (Peebles 1993). Absorption by these is clearly evident in the $\lambda < \lambda(\text{Ly}\alpha)$ spectra of the high redshift sample quasars. Since the accretion disk spectrum predicted for parameters typical of quasars: *e.g.*, $M_{BH} \sim 10^{8-9} M_\odot$ and $\dot{m} \sim 1$; peaks in the UV at wavelengths $\lambda \lesssim 1000\text{\AA}$, knowledge of the intrinsic continuum shape bluewards of Ly α would be useful in constraining disk models.

To correct the UV continua for flux suppression by superposition of numerous Ly α forest lines, we used high resolution spectra that had been obtained for 7 of the quasars from the $z > 3$ sample (Bechtold 1994; Dobrzycki & Bechtold 1996; Table 12). The resolution of these spectra, FWHM $\sim 50 - 100 \text{ km s}^{-1}$ (19 km s^{-1} for 2 of the objects), is sufficient to distinguish the absorption lines and permit a measurement of the continuum level in between these (Bechtold 1994). However, since these spectra are of necessity taken through a narrow slit, the continuum determined from them is not photometric. We have corrected it using our low resolution spectrophotometry, following the procedures described below and illustrated in Figure 2.

(1) We binned and smoothed the high resolution spectra to match the resolution of the spectrophotometry. (2) This was then divided into the spectrophotometry, which had been shifted by a few pixels to match the more accurate wavelength calibration of the high resolution data, to produce a ‘correction function’. (3) The ‘correction function’ was fit with a low order polynomial. The smoothing lengths, shifts and fit orders varied for each pair of spectra and are listed in Table 12. Because our smoothing procedure included zeroes outside the data range, it produced artificial gradients at the edges. When several high resolution spectra were used to expand the wavelength coverage, these spectra were treated separately until making the polynomial fit to the ratios. We tried both fitting all the sections at once and fitting each individually. As Table 12 shows, for Q0420 – 388 we chose to splice together a number of best fit polynomials while for Q2126 – 158, we used the single polynomial which, as we judged, simultaneously fit all of the ratios well. (4) Finally, we multiplied the continuum that had been fit through the high resolution spectra by this polynomial to produce the final Ly α forest corrected continuum. In some cases, there was ringing in the fitted polynomial near the edges of the spectra. The last column of Table 12 notes the regions where the corrected continuum is valid, not being affected by either smoothing or ringing.

5.3. The SEDs of the high redshift quasars

The flux calibrated, dereddened and blueshifted optical/UV spectral energy distributions of the 15 high redshift sample quasars are plotted in Figure 3. Corrected continua bluewards of Ly α

are plotted using thick lines. The mean SED determined from the radio-loud or radio-quiet quasars from the Elvis et al. (1994a) database of low redshift AGN is superposed for reference.

Four of the high redshift quasars were detected at L' or have upper limits at N which constrain their continua to be close to the mean low redshift continuum. Figure 4 shows their SEDs over the rest-frame spectral region which includes the L' and N datapoints.

5.4. Modifications to the low redshift SEDs

For many of the low redshift quasars there were multi-epoch observations, and some of the quasars showed significant variability. Thus, when possible, we selected the multi-wavelength observations that were obtained closest in time and reconstructed SEDs using only these. Table 13 lists the observation dates for the data we selected. For four quasars, Q0121 – 590, Q0804 + 761, Q1211 + 143 and Q2130 + 099, more than one SED resulted. The one which was judged by eye to look cleanest was used in the final analysis.

The Galactic gas-to-dust ratio and cosmological parameters that Elvis et al. (1994a) had assumed to deredden and blueshift the data on the low redshift ‘Atlas’ quasars ($N_H/E(B-V) = 5 \times 10^{21} \text{ cm}^{-2} \text{ mag}^{-1}$; $H_o = 50 \text{ km s}^{-1} \text{ Mpc}^{-1}$, $q_o = 0.5$) differ from the values we adopt in the paper. Therefore, before comparing the low and high redshift SEDs, it was necessary to convert the low redshift SEDs back to the observed frame using their values and then deredden and blueshift the data using ours.

5.5. Computation of continuum fluxes

We characterize the shapes of the rest-frame optical/UV continua by luminosities measured within a set of twelve narrow band windows which we chose upon examination of the composite QSO spectra constructed by Francis et al. (1991; LBQS) and Boyle (1990; AAT). The central wavelengths and widths of these bands are listed in Table 14 and indicated on the SED of one of the sample quasars (Figure 5).

Initially, eleven of these bands were considered continuum windows. Three are centered at the wavelengths through which Francis et al. (1991) fit a continuum to the composite LBQS spectrum, and five were added at wavelengths where the continuum fit closely approached the LBQS composite. A ninth band was centered at $\lambda_{rest} = 7500\text{\AA}$ to measure the red end of the optical continuum, but the flux there can only be estimated for the low redshift quasars and the $z > 3$ ones detected at L'. Finally, two bands centered at 1160\AA and 1115\AA sample the flux below Ly α . The twelfth band, centered at 2500\AA , where there are several strong FeII multiplets (Joly 1993), was selected to gauge FeII strength.

Around 3000\AA there is a small bump in the continua of many low redshift quasars (Oke, Shields

& Korycansky 1984). It is modelled as blended FeII and Balmer continuum emission (Wills, Netzer & Wills 1985). Though its strength varies from object to object, between 2000Å and 4000Å it may contribute as much as the continuum itself to the total flux (see Figure 2 of Neugebauer et al. 1987). The LBQS composite, however, does not show significant excess over the continuum fit within this region, and four of the ‘line-free’ bands lie between 2000Å and 4000Å. In our analysis, we treat the fluxes within these bands with caution, looking for indications of non-continuum emission (see Table 18, *e.g.*, which lists spectral indices computed with and without these points). Only the spectral indices determined without the 2000 – 4000Å data are used in the analysis, and the 2000 – 4000Å residuals are discussed in §9.2.

The luminosities within the narrow bands (Tables 15, 16 and 17) were determined as follows. The monochromatic luminosity emitted at the central wavelength of each band, νF_ν , was taken to be the average of the data points (scaled, dereddened, and blueshifted) within that band. The narrow widths of the bands ($\Delta\lambda = 20 - 40\text{\AA}$) and the smoothness of the energy distribution within them make this a good approximation to the integral of flux over frequency. Within the shortest wavelength bands (the bluest 2 for the high redshift quasars and the bluest 5 for the low redshift ones), where the datapoints are from moderate resolution ($R \sim 100 - 500$) optical spectrophotometry, there were abundant points over which to average. But at longer wavelengths the data are sparser and there are gaps between the datasets, which are mostly unavoidable because they are where atmospheric transmission is poor. Furthermore, the dispersion of the near-IR spectra is lower than the optical — about $11 - 17\text{\AA}/\text{pxl}$ rather than ~ 7 . Thus, the average fluxes within the redder bands were often computed either from relatively few data points or if none, by interpolation between the average fluxes computed within 50\AA wide bands on either side of the empty window. The width of 50\AA was chosen since it usually included sufficient data points to provide good statistics, yet did not extend to emission line features.

There were various sources of error in these narrow-band average luminosities: among them (1) errors in normalization, either from grey-scaling or flux calibration; (2) rms errors in the individual spectra; (3) errors in individual photometric points; and (4) scatter caused by having more than one epoch of data within a band. For the high redshift quasars, the normalization error was taken to be the error propagated from the errors in the photometry used to grey scale the IR spectra and optical spectrophotometry. For those quasars with Ly α forest corrected spectra, the normalization error of these was taken to be 10%, which was the typical scatter about the polynomial fit to the ratio of the binned, smoothed high resolution data to the spectrophotometric data. For the low redshift quasars, the normalization error in the IUE spectra was taken to be 10% (Bohlin et al. 1980). The errors that are given alongside the luminosities in Tables 15 – 17 both include the normalization and photometry errors, but incorporate the rms scatter in different ways. The first, σ_{avg} , uses a quadrature sum of the scatter in the individual spectra, which is an accurate reflection of the quality of the data and valid when variability is not an issue. In contrast, the second, σ_{var} , accounts for the rms scatter, *i.e.* σ_{N-1} , for all datapoints, spectroscopic and photometric, within the band.

Tables 15 and 16 list the monochromatic luminosities at each of the ten bands redwards of Ly α , for the high and low redshift sample objects, respectively. They also give the number of points used in the average, either within the band itself or within the two 50Å regions used in interpolating the flux, and the confidence in the computed luminosity: 3 signifies that it was directly computed from points within the band and well represents the flux level; 2, that it was interpolated; 1, that it does not represent the flux level well; and 0, that it could not be determined even by interpolation because of insufficient data coverage to the red.

The continuum luminosities in the two windows at $\lambda < \lambda_{\text{Ly}\alpha}$ can be computed only for a subset of objects from the low and high redshift samples: of the low redshift sample, only those objects with redshifts large enough to shift the 1115Å and 1160Å bands beyond the geo-coronal Ly α ; and of the high redshift one, only those 7 for which high resolution spectra enabled the correction of the $\lambda < \lambda_{\text{Ly}\alpha}$ continuum for flux suppression by Ly α forest. Consequently, luminosities at 1160Å were computed for 26 of the 27 low redshift quasars (all but Q0121 – 590) and 7 of the 15 high redshift ones, and luminosities at 1115Å, for 20 low and 7 high redshift objects. Table 17 lists these luminosities. For comparison, for the high redshift quasars, luminosities determined from uncorrected data are also given.

6. The optical/UV continuum shapes

6.1. Power law fits

Our first approach towards characterizing the optical/UV continuum shape was to fit a single power law through the set of average narrow band continuum fluxes. Since our coverage of the red and blue ends of the ‘blue bump’ was poor — only 4 of the 15 quasars in the high redshift sample were detected at L' and only 7 of the 15 had high resolution spectroscopy bluewards of Ly α — we focused on fitting the continuum from $\lambda_{\text{rest}} = 1285 - 5100\text{\AA}$ only. This region included 9 narrow band windows, four of which lie between 2000Å and 4000Å, in the ‘3000Å bump’ region. To insure that the power law fits are not influenced by the blended line emission, we tried both fitting through all 9 bands from 1285Å–5100Å and through the 5 bands which remained after excluding those between 2000Å and 4000Å. The spectral indices determined from both sets of fits are listed in Table 18. As the last column in the table shows, the differences between the the spectral indices computed with and without the 2000 – 4000Å data are small, especially for the high redshift quasars. K-S tests on the sets of spectral indices determined with and without the 2000–4000Å data give probabilities of 7% for the low and 0% for the high redshift sample that they differ. The residuals from the fits to just the 5 bands around the ‘3000Å bump’ are shown in Figure 6. For the low redshift quasars, the 2000 – 4000Å residuals are systematically positive, suggesting either the presence of an extra component or that the continuum has an intrinsic curvature at low but not at high redshift. This will be discussed further in §9.2, and for the analysis of continuum shapes we use the optical/UV spectral indices obtained without the data between 2000 and 4000Å.

7. The distributions of optical/UV spectral indices

The histograms in Figure 7 show the distributions of the $1285 - 5100\text{\AA}$ spectral indices, α_{ouv} for the high and low redshift samples. The mean (median) spectral indices for the 15 high and 27 low redshift quasars and for the 42 objects in the combined high and low redshift samples are -0.32 ± 0.07 (-0.29), -0.38 ± 0.07 (-0.40) and -0.36 ± 0.05 (-0.40), respectively. The latter is similar to the median determined for the set of 688 LBQS quasars (Francis et al. 1991), -0.33 , and also to the average optical/UV spectral index of -0.33 that Natali et al. (1998) find for a sample of 62 quasars, though they point out that the continuum is better described by a double power law, with a turnover at 3000\AA . We examine the shape of the continuum around 3000\AA further in §9.2. The mean values, medians and standard deviations of the distributions of optical/UV spectral indices are summarized in Table 19.

7.1. Diversity of continuum shapes

Even a cursory glance at the optical/UV continua and the distributions of spectral indices reveals a broad diversity. For both samples, the values of α_{ouv} range from ~ -1 to 0.5 . The standard deviations about the means, σ_{N-1} , are 0.28 and 0.35, for the high and low redshift samples, respectively. The interquartile ranges are from -0.57 to -0.26 for the low and -0.51 to -0.22 for the high redshift samples, so one-half of the objects in each sample lie within a strip of width 0.3 about the median. This width is about 10 times larger than the measurement errors (0.04 and 0.03 for the low and high redshift samples, respectively — see Table 18), and thus indicates that the spread in optical/UV continuum shapes is real and not due solely to measurement errors.

The broad range of optical/UV spectral indices in our samples is not unusual. Such diversity has been previously noted for many different samples (*e.g.* Richstone & Schmidt 1980, Neugebauer et al. 1987, Cheng, Gaskell & Koratkar 1991, Elvis 1992). Elvis et al. (1994a) computed the mean and dispersion of the SEDs of the 47 low redshift ‘Atlas’ AGN and concluded that, while the mean well-represented the sample, with the continua of two-thirds of the quasars within a factor of 2-3 of it, the spread in continuum shapes was significant. And, Francis et al. (1991) plot a histogram (their Figure 1) of optical/UV spectral indices for 688 LBQS quasars which shows that they span a range from about -1.5 to 1 .

Various explanations for the wide range of optical/UV continuum shapes have been proposed, among these: that it may arise from measurement errors (Cheng et al. 1991 — though they discuss only the UV continuum slope); variability; different amounts of unknown, and thus not corrected for, intrinsic reddening (Cheng et al. 1991); a range of shapes in the emitted continuum itself; or from combination of orientation and intrinsic reddening (Rowan-Robinson 1995).

As mentioned at the beginning of this section, the measurement errors are too small to account for the full range in our samples. To reduce the contribution of variability to the uncertainties, we

have tried to obtain the data for the high z quasars close in time and, as far as possible, to use quasi-simultaneous and simultaneous datasets for the low z quasars (see §5.4 and Table 13). The observed range in spectral index cannot be explained by errors in the Galactic column densities, which are known to better than $\sim 10^{20} \text{ cm}^{-2}$ (Stark et al. 1992), and most to $\sim 1 - 3 \times 10^{19} \text{ cm}^{-2}$ (Elvis, Lockman & Wilkes 1989, Murphy et al. 1996).

We have considered whether differing amounts of intrinsic extinction, applied to similarly shaped emitted continua, might produce the observed distribution of optical/UV continuum shapes. To account for the spread of $\Delta\alpha_{ouv} \approx 1$ in $1285 - 5100\text{\AA}$ spectral index requires intrinsic reddening up to $E_{B-V} = 0.11$ or 0.25 , depending on which extinction law: Small Magellanic Cloud (SMC; Bouchet et al. 1985, Prévot et al. 1984) or Galactic (MW; Savage and Mathis 1979, Rieke & Lebofsky 1985); is assumed (see the right hand panels, b and d, of Figure 7). The absence of the $10\mu\text{m}$ silicate feature and the non-universality of absorption at 2175\AA in quasar spectra argue for a dust composition in AGN unlike that in the Milky Way and more similar to that in the SMC. Hence the SMC, rather than Milky Way, extinction curve may better represent the AGN one (Czerny et al. 1995). Assuming both the SMC and Milky Way extinction laws and gas-to-dust ratios ($4.45 \times 10^{22} \text{ cm}^{-2}$ for the SMC, Bouchet et al. 1985, Prévot et al. 1984 and $4.8 \times 10^{21} \text{ cm}^{-2}$ for the MW, Savage & Mathis 1979), we find that the color excesses needed to produce the observed range in spectral index correspond to intrinsic column densities of $4.9 \times 10^{21} \text{ cm}^{-2}$ (SMC) and $1.2 \times 10^{21} \text{ cm}^{-2}$ (MW).

These are about 100 times larger than the column densities of less than $5 \times 10^{19} \text{ cm}^{-2}$ which Laor et al. (1997) infer from fits to high S/N ROSAT PSPC spectra of 23 quasars from the BQS sample with $z < 0.4$ and low Galactic column densities. But, they are consistent with those for the RIXOS X-ray AGN ($0 - 4 \times 10^{21} \text{ cm}^{-2}$; Puchnarewicz et al. 1996). Finally, they are about 10 times smaller than the intrinsic columns implied by fits to X-ray spectra of several high redshift, radio-loud quasars, three of which are in the high z sample: Q0014+813 ($N_{H,int} = 57.8^{+22.2}_{-20.4} \times 10^{21} \text{ cm}^{-2}$ from ASCA; Reeves et al. 1997); Q0636+680 ($N_{H,int} = 20^{+10}_{-8} \times 10^{21} \text{ cm}^{-2}$, ROSAT PSPC; Fiore et al. 1998; and Q2126-158 ($N_{H,int} = 12.9^{+7.2}_{-3.8} \times 10^{21} \text{ cm}^{-2}$, ROSAT PSPC; Elvis et al. 1994b or $12.6^{+6.6}_{-5.9} \times 10^{21} \text{ cm}^{-2}$, ASCA; Reeves et al. 1997). However, while there is evidence that optical reddening and X-ray absorption are paired at low redshift (Puchnarewicz et al. 1996, Elvis et al. 1998), Elvis et al. (1998) find that at high redshift there is no such correlation. In line with their result, we find no correlation between intrinsic column density and optical/UV spectral index for the three high redshift radio-loud quasars with strong X-ray absorption ($\alpha_{ouv} = -0.14, -0.57$ and -0.41 for Q0014+813, Q0636+680 and Q2126-158). So the gas-to-dust ratios in the intrinsic hydrogen columns at high redshift may differ substantially from those at low redshift or in the SMC or Milky Way. A better understanding of intrinsic absorption at high redshift is anticipated from XMM and Chandra.

The emitted optical/UV continuum might itself span a range of shapes. Thin disk spectra predicted for typical quasar masses and accretion rates are expected to show some curvature between 1285\AA and 5100\AA region, in which case the best-fitting power law slope within this spectral region

would be flatter than the canonical $\nu^{1/3}$ dependence (Frank, King & Raine 1995). The predicted disk spectrum is also anisotropic, so the turnover depends on viewing angle. A range of orientations within the sample may cause some scatter even if the black hole masses and accretion rates are identical. In addition to changes caused by shifts in turnover frequency, more complex accretion disk models which include scattering in the disk atmosphere (Czerny & Elvis 1987), Compton scattering by a corona (Czerny & Elvis 1987, Kurpiewski, Kuraszkiewicz & Czerny 1997), and external X-ray irradiation (Matt, Fabian & Ross 1993, Sincell & Krolik 1997), predict a range of spectral indices down to ~ -1 (Malkan 1991), near the lower end of the distribution, so accretion models can account for nearly the entire range of continuum slopes.

The slope of the continuum generated by free-free emission depends on the temperature of the emitting clouds and can range from ~ -0.6 to -0.2 , for $T=10^5$ to 10^6 K, the range of expected temperatures in quasars (Barvainis 1993). This is not enough to account for the full distribution of optical/UV continuum shapes.

7.2. Continuum evolution?

The distributions of spectral indices within the high and low redshift samples, though broad, are also similar, at a 96% significance as given by a K-S test. The mean spectral index is bluer for the high than for the low redshift sample, as would be expected for continuous evolution of a single generation, but a *t*-test to compare the means indicates the difference is not significant — the probability of randomly obtaining a larger *t* is 60%. Hence, our data do not give any strong evidence for evolution of the optical/UV continua between $z > 3$ and $z \sim 0.1$.

The similarity between the distributions of continuum shapes at high and low redshift is inconsistent with the evolution of only a single generation of quasars, whether the activity is continuous or recurrent, though the latter, since it allows for high accretion rates at low redshift and less mass growth, may be reconcilable with the data. The lack of significant evolution clearly favors models which involve the formation and evolution of multiple generations of quasars. Haiman & Menou (1999) fit the observed luminosity function evolution with multiple generations of quasars in which the characteristic accretion rate increases with redshift, while Haehnelt, Natarajan & Rees (1998) focus instead on evolution of the mass in their model. Referring back to the dependence of the disk temperature on mass and accretion rate, evolution of both \dot{M}/\dot{M}_{Edd} and M , at roughly the same rate, is implied by the lack of significant evolution in the continuum shape.

In this simple interpretation, we have assumed first, that the high and low redshift quasars lie at ends of a single continuum and, second, that the structures of the accretion disks (thin, slim, thick) are the same at high and low redshift (luminosity). The former assumption appears valid. The 27 low redshift objects have absolute magnitudes large enough to be classified as quasars, and even quasars and the lower luminosity Seyfert 1 galaxies are linked, as implied by the smooth continuity between their luminosity functions (Köhler et al. 1997). The greater concern is probably at high

redshift, where several of our sample quasars are among the most luminous objects in the universe. To move away from these extremes, we are beginning to survey the optical/UV continuum shapes of a larger, fainter sample of $z > 3$ quasars. Fits to some of these high redshift/luminosity quasars imply that they may be undergoing near- or super-Eddington accretion (Kuhn et al. 1995, Bechtold et al. 1994), which is inconsistent with thin disks. A comparison between the SEDs presented here and the predictions of various accretion models is planned.

8. Comparison with previous results

Though we find no significant difference between the optical/UV continuum shapes at low and high redshift (or low and high luminosity, given the strong $z - L$ correlation in the combined samples), prior studies have indicated that the shape of the UV continuum does evolve (O’Brien, Gondhalekar & Wilson 1988, Cheng et al. 1991) and that the optical/UV continuum is luminosity dependent (Wandel 1987, Mushotzky & Wandel 1989, Zheng & Malkan 1993). Our samples were not selected for a comprehensive correlation analysis: there are too few objects, and these are not evenly distributed in redshift and luminosity. We have looked for evidence of these previously reported correlations in our dataset, however, and this section discusses the outcome of these searches.

8.1. α_{uv} vs. redshift, luminosity

A trend toward harder (flatter) UV spectral indices at higher redshifts was reported both by Cheng, Gaskell & Koratkar (1991) and O’Brien, Gondhalekar & Wilson (1988). Multivariate linear regression fits to the UV spectral index as a function of both redshift, $\log(1+z)$, and UV luminosity, $L(1450\text{\AA})$, showed the primary correlation to be between UV spectral index and redshift.

We looked in our samples for similar correlations between the UV continuum shape, $\log(1+z)$ and $\log L(1460\text{\AA})$, using spectral indices measured between two pairs of the narrow-band monochromatic luminosities listed in Tables 15 and 16: (1285\AA, 2200\AA) and (1285\AA, 1460\AA); to characterize the UV continuum shapes. These and other point-to-point spectral indices are given in Table 20. The 1285\AA– 2200\AA spectral index matches the definition used by Cheng et al., while the 1285–1460\AA one is deliberately cut off at a wavelength short enough that there is no possibility of continuum contamination from the 3000\AA bump, the rationale of O’Brien et al. in measuring the UV spectral index from $\lambda\text{Ly}\alpha$ to 1900\AA. (We had not defined a narrow-band window between 1460\AA and 2200\AA, so cannot readily approximate their measure any better). Although the 1285 – 1460\AA spectral index represents the true continuum better than the 1285 – 2200\AA one, its smaller baseline yields larger errors and increased scatter, especially for the low redshift sample where the UV data are from the IUE and, for some objects, are relatively noisy.

We found positive correlations between the 1285 – 2200\AA spectral index and both redshift and

luminosity. The linear regression fits and two-tailed significances of the correlations, *i.e.*, one minus the probability of a chance correlation as given by the Kendall-tau test, are summarized in Table 21. When the UV continuum shape is represented by the $1285 - 1460\text{\AA}$ spectral index instead, the trends persist (the results of the linear regression fits are similar, albeit with larger errors), but the correlations disappear (significance levels $< 82\%$). From this analysis, it is difficult to determine whether the correlations are stronger for the $1285 - 2200\text{\AA}$ spectral indices because of their smaller errors and scatter, or instead reflect a luminosity or redshift dependence of the 3000\AA bump, which may be contaminating the continuum luminosity at 2200\AA (see section 9.2); but the similarity of the trends and linear fits for both measures of UV spectral index favors the former explanation.

To compare our results directly with O’Brien et al. and Cheng et al. requires re-computing the luminosities under the same cosmological assumptions as they made. Table 21 lists the parameters of the best-fitting lines alongside those that they determined. Our results from fitting spectral index against luminosity are in good agreement with theirs, though the slope of the spectral index vs. redshift relation that we derive is shallower, but still consistent within 1σ , than their result based on simultaneous fits of spectral index against luminosity and redshift. We tried a multivariate fit, but the strong luminosity-redshift correlation in our combined samples yields results very different from those of either group.

When our samples are broken down by redshift, the trend of increasing spectral index with luminosity or redshift remains, though is weaker. Only for the low redshift sample is the correlation between $1285 - 2200\text{\AA}$ spectral index and luminosity marginally significant, 95% by the Kendall-tau test. Neither the trend of UV spectral index against UV luminosity within the high redshift sample nor of UV spectral index against redshift within each sample is significant: the Kendall-tau significance level is $< 84\%$ in each case. We investigated whether the correlation between $\alpha(1285\text{\AA}, 2200\text{\AA})$ and luminosity holds for both UV and optical luminosities, and find it is stronger for the UV than for optical ones. A similar result is found for the optical/UV continuum shape (discussed in the next section): it is correlated with UV but not with the optical luminosity.

In sum, we find a positive correlation between the UV spectral index and UV luminosity (or redshift) in our combined high and low redshift samples, in good agreement with what Cheng et al. and O’Brien et al. had previously found for objects covering a similar range of redshifts. The strong luminosity-redshift correlation in our combined samples does not allow us to test their conclusion that the primary correlation is with redshift. The trend towards harder UV continua for higher luminosity or redshift exists for both measures of UV slope, but its increased significance for the $1285 - 2200\text{\AA}$ slope raises some doubt as to whether the trend is intrinsic or instead due to a luminosity or redshift dependent contribution of the 3000\AA bump at 2200\AA . Better fits to the UV continua would be needed to make stronger conclusions.

8.2. α_{ouv} vs. luminosity

As discussed in §7.2, we find no evidence for significant evolution of the optical/UV continuum shape. Given the strong redshift-luminosity correlation present in our combined samples, this would imply no significant correlation between the optical/UV continuum shape and luminosity, consistent with the results that Neugebauer et al. (1987) obtain from near-IR and optical observations of 105 PG quasars. Other groups, however, have reported trends between the rest-frame optical/UV continuum shapes and luminosities. Wandel (1987) and Mushotzky & Wandel (1989) found a correlation between the optical spectral index, measured between 4200 and 7500Å, and the rest-frame luminosity at 4200Å. And Zheng & Malkan (1993) found a reasonably significant anti-correlation (correlation coefficient, $r = -0.59$) between the 1250 – 6500Å continuum slope and $M_{4800\text{\AA}}$ for 145 QSOs and Seyfert 1 galaxies. We checked for correlations between optical luminosity, taken at $\lambda_{rest} = 4200\text{\AA}$ and 4750Å, and the α_{ouv} listed in column 7 of Table 18 but found none for the combined samples or the high or low redshift one individually. The results are given in Table 21.

Although the spectrum of starlight from the host galaxy peaks in the near-IR, its contribution to the optical continuum, especially for the low luminosity AGN, may be non-negligible (Elvis et al. 1994a). An increasing fraction of the starlight to AGN continuum with decreasing luminosity could account for the reported correlations. Wandel (1987) and Mushotzky & Wandel (1989) considered the role of host-galaxy starlight in the correlation and acknowledged that it may explain the correlation for luminosities, $L < 10^{45}$ erg s $^{-1}$, though to contribute significantly to the continua of higher luminosity quasars would require an implausibly high starlight flux (Mushotzky & Wandel 1989). Zheng & Malkan (1993) also questioned whether the contribution of host-galaxy starlight at 6500Å could account for the observed correlation; but, pointing to the persistence of the correlation when only the optical or UV spectral index or the brightest AGN (with $M < -23$) are used, concluded that, while important, the host galaxy contribution does not fully account for the correlation. To gauge the importance of host galaxy starlight to the optical slope–luminosity correlations, we measured the spectral indices from 1250Å–6500Å and absolute magnitudes at 4800Å of 46 AGN in the Atlas, with and without the host galaxy contribution subtracted⁶. As Figure 10 illustrates, the host galaxy starlight is most important at low luminosity and does effect a slope-luminosity correlation. When the starlight is not subtracted the spectral index and magnitude are weakly anti-correlated (Spearman correlation coefficient, $r_s = -0.37$, and the probability of a chance correlation, $p_s = 3\%$). With the host galaxy starlight spectrum subtracted, however, there is no evidence for a correlation between spectral index and absolute magnitude ($r_s = 0.13$ and $p_s = 37\%$).

⁶To improve statistics, the full ‘Atlas’ sample, and not just the subset of 27 studied here, was used to examine the host galaxy contribution. But since we have not computed narrow band luminosities for all these, we used the TIGER software package written by J. McDowell (Wilkes & McDowell 1995) to determine the 1250 – 6500Å spectral indices and $M_{4800\text{\AA}}$.

We checked whether the optical/UV continuum slope was also uncorrelated with UV luminosity, but found instead a positive correlation (99.5% significance) between α_{ouv} and the UV luminosity measured at 1285Å (see figure 9; there is also a correlation when UV luminosity is measured at 1460Å, but it is weaker). Though present for the combined samples (97% significance), it is strongest within the low redshift one (99.5%) and absent in the high redshift one, echoing the α_{uv} – UV luminosity correlation reported in the previous section. Therefore, while our analysis shows that host galaxy starlight can effect a correlation between α_{ouv} and optical luminosity, and this explains the absence of a correlation between optical/UV slope and optical luminosity in our host-galaxy corrected data, it does not explain why we should find a correlation between α_{ouv} and UV luminosity. A similar trend for variable quasars to have bluer continua in their higher luminosity states (Giveon et al. 1999) suggests an intrinsic origin, but further investigation is clearly needed.

9. Comparison continued — Continuum deviations from a single power law

Whereas the single power law fits to the optical/UV continuum energy distributions are adequate in most cases, a closer look at several continua (*e.g.* Q0055 – 269) shows that they steepen between the optical and UV, consistent with prior consensus that the overall optical/UV shape is more complex than a single power law (Neugebauer et al. 1987). This section examines the UV continuum shape shortwards of Ly α and around 3000Å.

9.1. UV turnover

In the extreme ultraviolet (EUV), the continuum must turnover to match up with the X-ray flux. Quasar accretion disk models predict a turnover in the EUV, so an accurate determination of the continuum shape in that region is important for testing these. Unfortunately, the EUV data are sparse and, for high redshift quasars, complicated by Ly α forest absorption. However, HST observations of over 100 quasars with $z > 0.33$ have provided valuable information on the rest-frame EUV continuum (Zheng et al. 1997). The composite spectrum formed by these data, after they were statistically corrected for Ly α forest absorption, shows a turndown at 1050Å, believed to be intrinsic (Zheng et al. 1997).

Although we do not have data at $\lambda_{rest} \sim 1050$ Å, we can use the 1115Å and 1160Å fluxes (Table 17) to investigate the continuum behavior at $\lambda < \lambda$ Ly α . Spectral indices were computed from 1115Å–1285Å and 1160Å–1285Å, 1285Å being the closest narrow band window to Ly α and well representative of the continuum level around the line. These are given in Table 20. Average spectral indices on either side of Ly α and statistics on the inflection at 1285Å are listed in Table 22. The first column indicates which sample is considered, the second lists which spectral indices are used in computing the inflection at 1285Å, and the third through sixth columns give the number of

objects in the sample, the average slope change, the scatter (σ_{N-1}) and the error in the mean. In the final three columns, the numbers of objects showing, at a level greater than 1σ , a turn over, no change or a turn up, are tabulated. The average slope change is, in general, positive (a turnover), except for the average change in slope from 1160Å to 1285Å to 2200Å for the low redshift and combined samples. The turn up for these might be explained if the 3000Å bump influences the luminosity measured at 2200Å for the low redshift AGN. Since there are over 3 times as many low redshift AGN as high redshift ones in the combined sample of objects for which 1160 – 1285Å and 1285 – 2200Å spectral indices can both be measured, the overall average is heavily weighted by the low redshift sample. Among the average values that are positive, several are within 1σ of the mean and hence consistent with no slope change. The numbers in the last three columns indicate that for most of the sample objects, there is no compelling evidence for a turnover out to 1160Å or 1115Å, and thereby suggest that it must occur at shorter wavelengths, consistent with the HST results of Zheng et al. (1997).

9.2. The 3000 Å region — excess or continuum turnover?

9.2.1. 3000Å excess

There is one clear difference between the high and low z samples. The residuals from a single power law fit (Figure 6) show a systematic excess between 2000 and 4000Å ($\log \nu = 14.88 - 15.18$) for the low redshift sample, which is weak or absent in the high redshift one. This region is that of the ‘small bump’ made up of blended FeII emission ($\lambda \sim 2000 - 3000\text{\AA}$) and Balmer continuum ($\lambda \sim 2500 - 3800\text{\AA}$; Wills, Netzer & Wills 1985). This result is robust; although the data coverage is somewhat sparse, we have tried multiple ways of quantifying the difference and they all agree.

We use four parameters to gauge the strength of the 3000 Å excess. Two are the residuals at 2500Å and 2660Å. Recall that the 2500Å window is centered on a strong FeII multiplet (Joly 1993), and the 2660Å one is the only other window of the four between 2000 and 4000Å within which luminosities could be directly measured for a significant part of the sample. Another measure is the luminosity of the excess relative to the continuum between 2200Å and 3023Å,

$$\frac{L(\text{excess})}{L(\text{cont})} = \frac{\int_{2200\text{\AA}}^{3023\text{\AA}} (F_{\nu,\text{total}} - F_{\nu,\text{fit}}) d\nu}{\int_{2200\text{\AA}}^{3023\text{\AA}} F_{\nu,\text{fit}} d\nu}. \quad (1)$$

where the continuum level, $F_{\nu,\text{fit}}$, is given by the power law fit through all bands between 1285Å and 5100Å excluding those four between 2000Å and 4000Å. Luminosity excesses were computed by trapezoidal integration over both directly measured and the interpolated narrow band fluxes, $F_{\nu,\text{total}}$, at 2200Å, 2500Å, 2660Å and 3023Å. Finally, the fourth parameter is the 2200 – 3023Å

equivalent width, which was computed as follows:

$$EW(2200 - 3023\text{\AA}) = \int_{2200\text{\AA}}^{3023\text{\AA}} (F_{\nu, total} - F_{\nu, fit})/F_{\nu, fit} d\nu. \quad (2)$$

Errors on the residuals are simply taken to be the errors on the measured narrow band fluxes (Table 15 and 16), and errors on the fractional luminosity excesses and equivalent widths are computed by propagating the sources of error in equations 1 and 2. The 2500\AA and 2660\AA residuals, ratios of excess to total luminosity and the EW(2200 – 3023\AA) are listed in Table 23. The last column indicates the quality of the four narrow band average luminosities from 2500\AA to 3023\AA — whether they are computed directly (3), interpolated (2) or if they do not represent what is believed to be the true flux level, regardless of how they are determined (1). The values that are listed in parentheses in the table were determined solely from interpolated fluxes or from one or more discrepant points, and were not used to compute the statistics, however the results would not be significantly different if they were.

The distributions of the residuals, luminosity ratios and equivalent widths are plotted in Figure 11. The K-S probabilities that the 2500\AA residuals, 2660\AA residuals, 2200 – 3023\AA excesses and equivalent widths of the high and low redshift samples differ are 99.95%, 99.97%, 99.75% and 99.75%, respectively. Equivalent widths for the high redshift sample range from –10\AA to 300\AA, while for the low redshift one, they are 100\AA–700\AA. The average equivalent width for the high redshift sample is 100\AA, but the median is 35\AA. These average and median values are 3 and 8 times lower than those for the low redshift sample.

Though the 3000\AA excesses for most of the high redshift quasars are consistent with zero, five show some evidence for excess emission. Q0055 – 269 has the clearest indication of a 3000\AA bump. Both its 2500\AA and 2660\AA residuals were directly measured, and they and the fractional luminosity excess and equivalent width are significant to greater than 3σ . Q0347 – 383, Q2204 – 408 and Q1935 – 692 also show evidence for a 3000\AA bump, as does Q1208 + 101, though its residuals and equivalent width had to be determined from interpolated fluxes. The 2200 – 3023\AA equivalent widths of these five ‘3000\AA excess’ quasars are consistent with or greater than the 2000 – 3000\AA equivalent width of 130\AA–157\AA (depending on the assumed line profile) that Thompson, Hill & Elston (1999) measured from a composite spectrum of six quasars with $< z > = 3.35$. They also lie within the range covered by our $z \sim 0.1$ sample, though are all less than the average for it ($\sim 300\text{\AA}$). It is interesting that two of our $z > 3$ sample quasars which are considered to be strong iron emitters based on their FeII(opt)/H\beta ratios: Q0014 + 813 and Q0636 + 680 (Elston, Thompson & Hill 1994, but see Murayama et al. 1996); show little or no evidence for a 3000\AA excess. Direct measurements of the UV FeII multiplets in the J-band spectra, and comparison of these to the 3000\AA bump and optical FeII strengths would shed some light on this apparent discrepancy.

These five $z > 3$ quasars notwithstanding, we find that the 3000\AA excess is on the whole much weaker (or absent) in the SEDs of the $z > 3$ sample quasars than in those of the $z \sim 0.1$ ones. If it is primarily blended FeII emission, and the iron abundance does not evolve significantly as

Thompson, Hill & Elston (1999) concluded, then the explanation must lie with other parameters which affect the strength of the FeII emission, such as its energy source.

There is abundant evidence for a link between the strength of FeII emission and the X-ray properties, though the origin of this is uncertain. In general, the AGN with flat X-ray spectra or strong X-ray emission tend not to have strong optical FeII (Wang, Brinkmann & Bergeron 1996, Laor et al. 1997, Lawrence et al. 1997, Wilkes et al. 1999). Green et al. (1995), however, found a positive correlation between the UV FeII and X-ray strengths: the LBQS quasars with the strongest UV FeII emission have soft X-ray (ROSAT) fluxes 2 times greater than the sample average. The discrepant results and inconsistency of most with the expectations of standard photoionization models (*e.g.* Krolik & Kallman 1988) are confusing, and other mechanisms such as collisional excitation may play a large role in FeII production (Kwan et al. 1995, Collin & Joly 2001). Kwan et al. (1995) suggest that FeII may be collisionally excited within a well defined region of the accretion disk, and this dependence of FeII on the accretion flow has been invoked to explain the strong FeII emission seen in the spectra of narrow line Seyfert 1s and $z > 4$ quasars, both of which are assumed to be young and accreting at high rates (Mathur 2000). The strong evolution that we find in the 3000Å excess does not support this analogy between NLSy1 and high redshift quasars, though a more rigorous test, using measures of UV and optical FeII features, would be interesting, especially given that our low redshift sample contains several objects classified as NLSy1s, including the prototype, IZw1.

We looked in our data for any trends between the strength of the 3000Å excess and the quasars' X-ray properties. All the quasars in our low redshift sample have X-ray data from the Einstein IPC, and 8 of the 15 in the high redshift one were detected with the ROSAT PSPC (but these include only 1 of the 5 high redshift quasars with a relatively strong 3000Å excess). We found no significant correlations between the 3000Å bump strength (any of the 4 measures) and the rest-frame 2500Å to 2keV flux ratio, α_{ox} (see Tables 1 and 2) or X-ray spectral index, α_x (case A in Table 1 of Bechtold et al. 1994 and Table 2 of the ‘Atlas’), neither in the combined high and low redshift samples nor in each individually. Though the number of objects considered is small for such statistical tests, the lack of any trend between the strength of the 3000Å excess and X-ray emission is puzzling, especially given that the samples are well separated in α_{ox} .

In sum, while the difference in strength of the 3000Å excess between the high and low redshift samples is clear, its origin remains uncertain. First, we have assumed, based on models at low redshift, that it is primarily due to FeII, though other factors could contribute. A comparison of its strength with direct measurements of UV and optical FeII multiplets, which are apparent in the J and K spectra of some of the high redshift objects and in the UV and optical for the low redshift ones (Wilkes et al. 1999), would help resolve this issue. Second, the models to explain FeII production in quasars are themselves uncertain. However, the evidence for an X-ray-FeII link argues for the collection of X-ray spectra for all the high redshift sample quasars; a comparison of these with the 3000Å excess and UV and optical FeII strengths could yield some clues to the evolution.

9.2.2. Optical continuum turnover

Recently, several groups have reported evidence for an intrinsic turnover in the continuum at 3000Å (Zheng & Malkan 1993, Natali et al. 1998, Carballo et al. 1999). The average spectral indices measured on either side of $\sim 3000\text{\AA}$ differ by $\sim 0.8 - 0.9$. The immediate suspicion is that the 3000Å FeII and BaC emission bump is responsible for this turnover. However, Zheng & Malkan, using Malkan's (1988) estimate that emission from the small bump contributes about 20% of the total flux at 3100Å, determine that, while consideration of it could reduce the intrinsic slope change to 0.45, it would not eliminate it. Similarly, Carballo et al. have examined the role of FeII and BaC emission, but conclude that it alone cannot explain the turnover.

To test these results and assay the role of the small bump in producing the turnover, we have computed point-to-point spectral indices from the SEDs of the high and low redshift quasars. Spectral indices computed from 1285 – 3023Å and 3023 – 5100Å have been used to measure the continuum slopes below (UV) and above (optical) 3000Å, respectively. These closely match Zheng & Malkan's (1993) definitions of α_{uv} and α_{opt} . To move away from the influence of the 3000Å bump we also measured the UV spectral index from 1285Å to 1460Å and 1285Å to 2200Å, and the optical one starting from 4200Å rather than 3023Å. Table 20 lists the spectral indices, and Table 24 lists the average spectral index, scatter and standard deviation in the mean for the high and low redshift and the combined samples in addition to the results of statistical tests (*t*-tests and K-S tests) to compare the various optical and UV slopes. As the table shows, there is a clear slope change when the spectral indices are measured to 3023Å: the average UV and optical spectral indices are -0.68 ± 0.07 and 0.18 ± 0.07 , respectively. Both the *t*-test and K-S tests strongly indicate a difference in optical and UV slopes when measured to 3023Å.

When the spectral indices are computed without using data within the 2000-4000Å small bump region, a difference between those computed shortwards and longwards of 3000Å still exists, though is less significant. The average UV spectral indices are -0.61 ± 0.07 (1285-2200Å) and -0.33 ± 0.18 (1285-1460Å); both redder than the average optical (4200-5100Å) spectral index of -0.09 ± 0.13 . But these averages are dominated by the low redshift sample, for which the slope change appears to be stronger. The statistics suggest that the 3000Å excess is responsible for the observed optical/UV inflection, but they do not rule out an intrinsic continuum turnover. To discern the relative contributions of blended line and continuum emission to the 3000Å bump would require a thorough treatment of the FeII+BaC emission and better measures of the spectral indices, especially over short baselines.

10. Conclusions

To look for signatures of physical evolution in quasars, which are expected given their strong statistical evolution, we have constructed the rest-frame optical/UV spectral energy distributions of 15 $z > 3$ quasars, using near-IR spectroscopy, optical spectrophotometry, and near-IR and optical

photometry. We compare these with the SEDs of the set of 27 low redshift ($z \sim 0.1$) quasars from the ‘Atlas’ (Elvis et al. 1994a) whose luminosities with respect to L_* lie within the same range spanned by the high redshift sample quasars. The SEDs of the $z > 3$ quasars are presented, and their shapes are characterized by single power law fits to the average continuum fluxes measured within line-free narrow windows between 1285Å and 5100Å. We list the conclusions drawn from an examination and comparison of the distributions of the optical/UV spectral indices of the high and low redshift samples.

1. *The optical/UV continuum shapes at high and low redshift span a broad range.* The distributions of spectral indices for both the high and low redshift samples are broad, spanning a full range of ~ 1 in spectral index. In both cases the interquartile spread is ~ 0.30 , too large to be explained by measurement errors. It is also unlikely that variability or uncertainties in Galactic extinction can account for it. Intrinsic reddening and the diversity in the shapes of the emitted spectra produced by accretion disk models may both contribute to this spread, as Rowan-Robinson (1995) concluded in an earlier study.

2. *The shapes of the optical/UV continua at high and low redshift do not differ significantly.* Half of the high redshift sample objects have α_{ouv} between -0.51 to -0.22 , and half of the low redshift ones have α_{ouv} between -0.57 to -0.26 . The mean (median) spectral indices for the high and low redshift samples are -0.32 (-0.29) and -0.38 (-0.40), respectively. Though these are bluer for the high redshift sample, the difference in the means is significant to only 60%, as measured by the t -test. A K-S test indicates that the spectral index distributions are similar to a high confidence level, 96%. This similarity disfavors the hypothesis that the observed luminosity evolution derives from the continuous long-timescale evolution of a single generation of quasars, and instead is easier to reconcile with models which invoke multiple generations.

3. *The 3000Å excess is stronger in the low redshift sample than in the high redshift one, where it is generally weak or absent.* While there is little evidence for evolution in the optical/UV continuum slopes, the SEDs of the high and low redshift samples do differ significantly in the 3000Å small bump region. Residuals from the single power law fits, measured at 2500Å, 2660Å, and between 2200Å and 3023Å, are all generally stronger at low redshift than at high. The K-S significance of this result is $> 99\%$ for all four measures. Assuming the 3000Å excess is primarily blended FeII emission, the relative weakness or absence of the 3000Å bump at high redshift indicates either a smaller abundance of iron or differences in other parameters affecting FeII strength. Recent results of Thompson et al. show no change in the UV FeII strength from $z \sim 4$ to $z \sim 0.88$, though they did not compare with a set of lower redshift AGN. The $z \sim 0.1$ ‘Atlas’ AGN could have greater iron abundances. A better explanation, though, might focus on the shape of the photoionizing soft X-ray continuum, which is relatively strong in the ‘Atlas’ AGN, since these were selected based on counts measured with the *Einstein* Observatory, or on other parameters which affect the FeII strength. Further work is needed to determine the origin of the differences between the $\sim 3000\text{\AA}$ continua of the high and low redshift quasars. The planned emission line study, which will involve fitting the individual FeII complexes, should enable a more thorough analysis of the 3000Å excess.

To look for links with the X-ray properties, X-ray spectra are needed for all the high z sample quasars.

We looked in our dataset for previously reported correlations between UV spectral index and redshift or luminosity and between optical/UV spectral index and luminosity.

4. *The UV spectral indices in our dataset become flatter (hotter) with increasing luminosity or redshift, consistent with previous results.* The correlations are significant for $\alpha(1285\text{\AA}, 2200\text{\AA})$ but much weaker for $\alpha(1285\text{\AA}, 1460\text{\AA})$; either the large errors and scatter in the spectral indices measured over such a short baseline dissolve any correlation which may be present, or FeII and BaC emission affect the 2200\AA flux in which case the the correlation is not intrinsic to the continuum but reflects the stronger 3000\AA excess at low than at high redshifts (or luminosities, given the strong redshift-luminosity correlation in the combined samples).

5. *The optical/UV spectral index, as measured by a power law fit, is correlated with UV, but not optical, luminosity for the low redshift sample.* Starlight from the the host galaxy does contribute to the red optical flux (Elvis et al. 1994a) and must be considered. However, the correlation with UV luminosity exists even in our data where the host galaxy has been carefully removed from the SEDs of the low redshift quasars. It may be related to the energy generation mechanism, and we plan to investigate its origin more carefully.

The primary goal of this paper is to present the spectral energy distributions of the 15 quasars in the high redshift sample and contrast them with the SEDs of a comparison sample at low redshift. Future work will concentrate on fitting these with accretion disk and other models and analyzing the emission line properties. The samples discussed here suffered from (1) the strong redshift-luminosity correlation which resulted from the luminosity matching selection criteria, and (2) a bias to the bright end of the luminosity function (several of the high redshift quasars were at one time considered the most luminous objects in the universe) which arose from the need for IR spectroscopy of these. We are beginning a survey of the continuum shapes of a set of $z > 3$ radio loud quasars which should extend the present sample by 2-3 magnitudes. This will have the advantage of including less extreme quasars and enabling us to begin to disentangle luminosity from redshift trends.

Since this project involved many observing runs, using a range of different telescopes and instruments, it relied on the help of many people. We thank M. and G. Rieke for setting up and helping us obtain the observations with Fspec. G. Rieke and R. Cutri helped O.P.K. obtain the IR bolometer and photometer observations, and R. Cutri and S. Kenyon obtained the IR photometry that is presented here for 6 of the quasars. We are grateful also to D. Joyce for his help with the CRSP observations at KPNO. P. Berlind obtained the optical spectrophotometry of Q0956 + 122 with FAST at the FLWO 1.5-m. We gratefully acknowledge the assistance of the staffs at the FLWO, MMTO, KPNO and CTIO. The Ohio State Infrared Imager/Spectrometer, OSIRIS, was built using funds from NSF awards AST 90-161112 and AST 92-18449 by the OSU

Astronomical Instrumentation Facility. We also thank those who helped with the data reduction. The VLA data were reduced by C. Fassnacht. K. Kearns and M. Davisson reduced some of the optical spectrophotometry presented here. The Fspec data were reduced up to the stage of flux calibration using IRAF tasks and scripts written at University of Arizona, Steward Observatory, by M. Rieke, C. Engelbracht, L. Shier and D. Williams. B. Wilkes and J. McDowell were consulted throughout the course of the project and we thank them for many helpful discussions key to its progress. Finally, we thank the anonymous referee for suggestions which helped to improve the presentation. O.P.K. acknowledges support from a NASA Graduate Student Researchers Program grant during a part of this work. M.E. acknowledges NASA grants NAGW-2201 and NAG5-6078, and J.B. acknowledges support from NASA ADP NAG5-3691 and NSF AST-9617060.

REFERENCES

Barthel, P. D., Tytler, D. R. & Thomson, B. A&AS, 82, 339.

Barvainis, R. 1993, ApJ, 412, 513.

Bechtold, J. 1994, ApJS, 91, 1.

Bechtold, J., et al. 1994, AJ, 108, 374.

Bohlin, R. C., Holm, A. V., Savage, B. D., Snijders, M. A. J. & Sparks, W. M. 1980 A&A, 85, 1.

Bouchet, P., Lequeux, J., Maurice, E., Prévot, L. & Prévot-Burnichon, M. L. 1985, A&A, 149, 330.

Boyle, B. J., Shanks, T. & Peterson, B. A. 1988, MNRAS, 235, 935.

Boyle, B. J. 1990, MNRAS, 243, 231.

Boyle B. J., Jones L.R., Shanks T., Marano B., Zitelli V., & Zamorani G., 1991, in ASP Conf. Ser. 21, The Space Distribution of Quasars, ed. D. Crampton, (San Francisco: ASP), 191.

Boyle, B. J., Shanks, T., Croom, S. M., Smith, R. J., Miller, L., Loaring, N. & Heymans, C. 2000, MNRAS, 317, 1014.

Campins, H., Rieke, G. H. & Lebofsky, M. J. 1985, AJ, 90, 896.

Carballo, R., González-Serrano J. I., Benn, C. R., Sánchez, S. F. & Vigotti, M. 1999, MNRAS, 306, 137.

Carilli, C. L., Menten, K. M., Reid, M. J., Rupen, M. P. & Yun, M. S. 1998, ApJ, 494, 175.

Casali, M. M. & Hawarden, T. G. 1992, UKIRT Newsletter, 4, 33.

Cavaliere, A., Giallongo, E., Padovani, P. & Vagnetti, F. 1988, in ASP Conf. Ser. 2, Proceedings of a Workshop on Optical Surveys for Quasars, ed. P. Osmer, A. Porter, R. Green & C. Foltz (San Francisco: ASP), 335.

Cavaliere, A. & Vittorini, V. 1998, in ASP Conf. Ser. 146, The Young Universe: Galaxy Formation and Evolution at Intermediate and High Redshift, eds. S. D'Odorico, A. Fontana & E. Giallongo, (San Francisco: ASP), 26.

Cheng, F. H., Gaskell, C. M. & Koratkar, A. P. 1991, ApJ, 370, 487.

Choi, Y., Yang, J. & Yi, I. 1999, ApJ, 518, L77

Choi, Y., Yang, J. & Yi, I. 2000, astro-ph/0005590.

Collin, S. and Joly, M. 2001, New Astronomy Reviews, 44, 531.

Cooper, D. E., Bui, D. & Bailey, R. B. 1993, Proc. SPIE, 1946, 170.

Czerny, B. & Elvis, M. 1987, ApJ, 321, 305.

Czerny, B., Loska, Z., Szczerba, R., Cukierska, J. & Madejski, G. 1995, Acta Astron., 45, 623.

DePoy, D. L., Atwood, B., Byard, P., Frogel, J. & O'Brien, T. 1993, Proc. SPIE, 1946, 667.

Dobrzycki, A. & Bechtold, J. 1996 ApJ, 457, 102.

Elias, J. H., Frogel, J. A., Matthews, K. & Neugebauer, G. 1982, AJ, 87, 1029.

Elston, R., Thompson, K. L. & Hill, G. J. 1994, Nature, 367, 250.

Elvis, M., Lockman, F. J. & Wilkes, B. J. 1989, AJ, 97, 777.

Elvis, M. 1992, in “Frontiers of X-ray Astronomy”, eds. Y. Tanaka & K. Koyama, Universal Academic Press, p.567.

Elvis, M., Wilkes, B. J., McDowell, J. C., Green, R. F., Bechtold, J., Willner, S. P., Cutri, R., Oey, M. S. & Polomski, E., 1994a, ApJS, 95, 1.

Elvis, M., Fiore, F., Wilkes, B. J., McDowell, J. C. 1994b, ApJ, 422, 60.

Elvis, M., Fiore, F., Giommi, P. & Padovani, P. 1998, ApJ, 492, 91.

Fabricant, D., Cheimets, P., Caldwell, N. & Geary, J. 1998, PASP, 110, 79.

Fan, X., et al. 2000, AJ, 120, 1167.

Fiore, F., Elvis, M., Giommi, P. & Padovani, P. 1998, ApJ, 492, 79.

Francis, P. J., Hewett, P. C., Foltz, C. B., Chaffee, F. H., Weymann, R. J. & Morris, S. L. 1991, ApJ, 373, 465.

Frank, J., King, A. R. & Raine, D. J. 1992, Accretion Power in Astrophysics, 2nd Edition, (Cambridge: Cambridge University Press).

Giallongo, E., Fontana, A., Cristiani, S. & D'Odorico, S. 1999, ApJ, 510, 605.

Giveon, U., Maoz, D., Kaspi, S., Netzer, H. & Smith, P. S. 1999, MNRAS, 306, 637.

Goldschmidt, P., Miller, L., LaFranca, F. & Cristiani, S. 1992, MNRAS, 256, 65P.

Goldschmidt, P. & Miller, L. 1998, MNRAS, 293, 107.

Green, P. J., et al. 1995, ApJ, 450, 51.

Gregory, P. C. & Condon, J. J. 1991, ApJS, 75, 1011.

Haehnelt, M. G. & Rees, M. J. 1993, MNRAS, 263, 168.

Haehnelt, M. G. , Natarajan, P. & Rees, M. J. 1998, MNRAS, 300, 817.

Hagen, H.-J., Cordis, L., Engels, D., Groote, D., Haug, U., Heber, U., Köhler, Th., Wisotzki, L. & Reimers, D. 1992, A&A, 253, L5.

Haiman, Z. & Menou, K. 2000, ApJ, 531, 42.

Hamuy, M., Walker, A. R., Suntzeff, N. B., Gigoux, P., Heathcote, S. R. & Phillips, M. M. 1992, PASP, 104, 533.

Hawarden, T. G., Leggett, S. K., Letawsky, M. B., Ballantyne, D. R. & Casali, M. M. 2001, MNRAS, in press.

Hawkins, M. R. S. & Véron, P. 1993, MNRAS, 260, 202.

Hawkins, M. R. S. & Véron, P. 1995, MNRAS, 275, 1102.

Hayes, D. S. 1985, in “Calibration of Fundamental Stellar Quantities: proceedings of the 111th Symposium of the IAU”, eds. D. S. Hayes, L. E. Pasinetti & A. G. Davis Phillip, [Boston: D. Reidel Publishing Co.], pg 225.

Hewett, P. C., Foltz, C. B. & Chaffee, F. H. 1993, ApJ, 406, L43.

Hewett, P. C., Foltz, C. B. & Chaffee, F. H. 1995, AJ, 109, 1498.

Hewitt, A. & Burbidge, G. 1991, ApJS, 63, 1.

Hewitt, A. & Burbidge, G. 1993, ApJS, 87, 451.

Jauncey, D. L, Savage, A., Morabito, D. D., Preston, R. A., Nicolson, G. D. & Tzioumis, A. K. 1989, AJ, 98, 54.

Johnson, H. L. 1966, ARA&A, 4, 193.

Joly, M. 1993, Annales de Physique, 18(3), p. 241.

Joyce, R. R., Fowler, A. M. & Heim, G. B. 1994, in Proc. SPIE, 2198, 725.

Kauffmann, G. & Haehnelt, M. 2000, MNRAS, 311, 576.

Keller, L. D., Sabol B. A. & Rieke, G. H. 1990, Proc. SPIE, 1235, 160.

Kennefick, J. D., Djorgovski, S. G. & de Carvalho, R. R. 1995, ApJ, 110, 2553.

Köhler, T., Groote, D., Reimers, D. & Wisotzki, L. 1997, A&A, 325, 502.

Koo, D. C. & Kron, R. G. 1988, ApJ, 325, 92.

Krolik, J. H. & Kallman, T. R. 1988, *ApJ*, 324, 714.

Kuhn, O., Bechtold, J., Cutri, R., Elvis, M. & Rieke, M. 1995, *ApJ*, 438, 643.

Kurpiewski, A., Kuraszkiewicz, J. & Czerny, B. 1997, *MNRAS*, 285, 725.

Kwan, J. Cheng, F.-Z., Fang, L.-Z., Zheng, W. and Ge, J. 1995, *ApJ*, 440, 628.

LaFranca, F. & Cristiani, S. 1997, *AJ*, 113, 1517.

Landolt, A. 1992, *AJ*, 104, 340.

Lanzetta, K. M., Wolfe, A. M., Turnshek, D. A., Lu, L., McMahon, R. G. & Hazard, C. 1991, *ApJS*, 77, 1.

Laor, A. & Netzer, H. 1989, *MNRAS*, 238, 897.

Laor, A., Fiore, F., Elvis, M., Wilkes, B. J. & McDowell, J. C. 1997, *ApJ*, 477, 93.

Lawrence, A., Elvis, M., Wilkes, B. J., McHardy, I. & Brandt, N. 1997, *MNRAS*, 285, 879.

Léhar, J., Falco, E. E., Kochanek, C. S., McLeod, B. A., Muñoz, J. A., Impey, C. D., Rix, H.-W., Keeton, C. R. & Peng, C. Y. 2000, *ApJ*, 536, 584.

Londish, D., Boyle, B. J. & Schade, D. J. 2000, *MNRAS*, 318, 411.

Magorrian, J., et al. 1998, *ApJ*, 115, 2285.

Malkan, M. A. & Sargent, W. L. W. 1982, *ApJ*, 254, 22.

Malkan, M. A. 1988, *Adv. Space Res.*, 8, 49.

Malkan, M. A. 1991, in “Structure and Emission Properties of Accretion Disks”, Proc. of the Sixth IAP Astrophysics Meeting/IAU Colloquium No. 129, eds. C. Bertout, S. Collin-Souffrin, J. P. Lasota & J. Tran Thanh Van, (Gif sur Yvette Cedex, France: Editions Frontières), 165.

Maoz, D., Bahcall, J. N., Schneider, D. P., Doxsey, R., Bahcall, N. A., Filippenko, A. V., Goss, W. M., Lahav, O. & Yanny, B. 1992, *ApJ*, 386, L1.

Marshall, H. L. 1985, *ApJ*, 299, 109.

Massey, P., Strobel, K., Barnes, J. V. & Anderson, E. 1988, *ApJ*, 328, 315.

Massey, P., & Gronwall, C. 1990, *ApJ*, 358, 344.

Mathur, S. 2000, *MNRAS*, 314, L17.

Matt, G., Fabian, A. C. & Ross, R. R. 1993, *MNRAS*, 264, 839.

McDowell, J., Kuhn, O., Elvis, M. & Wilkes, B. 1991, in “Structure and Emission Properties of Accretion Disks”, Proc. of the Sixth IAP Astrophysics Meeting/IAU Colloquium No. 129, eds. C. Bertout, S. Collin-Souffrin, J. P. Lasota & J. Tran Thanh Van, (Gif sur Yvette Cedex, France: Editions Frontières), 473.

Murayama, T., Taniguchi, Y., Evans, A. S., Sanders, D. B., Ohyama, Y., Kawara, K. & Arimoto, N. 1998, AJ, 115, 2237.

Murphy, E. M., Lockman, F. J., Laor, A. & Elvis, M. 1996, ApJS, 105, 369.

Mushotzky, R. F. & Wandel, A. 1989, ApJ, 339, 674.

Natali, F., Giallongo, E., Cristiani, S. & LaFranca, F. 1998, AJ, 115, 397.

Neugebauer, G., Green, R. F., Matthews, K., Schmidt, M., Soifer, B. T. & Bennett, J. 1987, ApJS, 63, 615.

O’Brien, P. T., Gondhalekar, P. M. & Wilson, R. 1988 MNRAS, 233, 801.

Oke, J. B. 1974, ApJS, 27, 210.

Oke, J. B., Shields, G. A. & Korycansky, D. G. 1984, ApJ, 277, 64.

Peebles, P. J. E. 1993, Principles of Physical Cosmology, (Princeton: Princeton University Press).

Pei, Y. C., Fall, S. M. & Bechtold, J. B. 1991, ApJ, 378, 6.

Pei, Y. C. 1995a, ApJ, 438, 623.

Pei, Y. C. 1995b, ApJ, 440, 485.

Prévot, M. L., Lequeux, J., Maurice, E., Prévot, L. & Rocca-Volmerange, B. 1984, A&A, 132, 389.

Puchnarewicz, E. M., et al. 1996, MNRAS, 315, 1.

Reeves, J. N., Turner, M. J. L., Ohashi, T. & Kii, T. 1997, MNRAS, 292, 468.

Richstone, D., et al. 1998, Nature, 395, A14.

Richstone, D. O. & Schmidt, M. 1980, ApJ, 235, 361.

Rieke, G. H. 1984, in MMTO Visiting Astronomer Information, Multiple Mirror Telescope Observatory Technical Report No. 13.

Rieke, G. H. & Lebofsky, M. J. 1985, ApJ, 288, 618.

Rieke, G. H., Lebofsky, M. J. & Low, F. J. 1985, , AJ, 90, 900.

Rowan-Robinson, M. 1995, MNRAS, 272, 737.

Salucci, P., Szuszkiewicz, E., Monaco, P. & Danese, L. 1999, MNRAS, 307, 637.

Savage, B. D. & Mathis, J. S. 1979, ARA&A, 17, 73.

Schmidt, M. 1968, ApJ, 151, 393.

Schmidt, M. & Green, R. F. 1983, ApJ, 269, 352.

Schmidt, M., Schneider, D. P. & Gunn, J. E. 1995, AJ, 110, 68.

Schneider, D. P., et al. 1992, PASP, 104, 678.

Shields, G. A. 1979, Nature, 272, 706.

Siemiginowska, A. & Elvis, M. 1997, ApJ, 482, L9.

Sincell, M. W. & Krolik, J. H. 1997, ApJ, 476, 605.

Stark, A. A., Gammie, C. F., Wilson, R. W., Bally, J., Linke, R. A., Heiles, C. & Hurwitz, M. 1992, ApJS, 79, 77.

Steidel, C. C. 1990, ApJS, 72, 1.

Sun, W.-H. & Malkan, M. A. 1989, ApJ, 346, 68.

Thompson, K. L., Hill, G. J. & Elston, R. 1999, ApJ, 515, 487.

Tokunaga, A. T. 1984, AJ, 89, 172.

Tytler, D. & Fan, X.-M. 1992, ApJS, 79, 1.

Tytler, D. 1999, in ASP Conf. Ser. 162, Quasars and Cosmology, ed. G. Ferland and J. Baldwin (San Francisco: ASP), 449.

Véron-Cetty, M.-P. & Véron, P. 1993, “A Catalogue of Quasars and Active Nuclei (6th edition)”, ESO Scientific Report, No. 13.

Wandel, A. 1987, ApJ, 316, L55.

Wang, T., Brinkmann, W. & Bergeron, J. 1996, A&A, 309, 81.

Warren, S. J., Hewett, P. C. & Osmer, P. J., 1994, ApJ, 421, 412.

Webb, J. K., Parnell, H. C., Carswell, R. F., McMahon, R. G., Irwin, M. J., Hazard, C., Ferlet, R. & Vidae-Madjar, A. 1988, The Messenger, 51, 15.

Wilkes, B. J. & Elvis, M. 1987, ApJ, 323, 243.

Wilkes, B. J. & McDowell, J. C. 1995, in ASP Conf. Ser. 61, Astronomical Data Analysis and Software Systems III, ed. D. Crabtree, R. Hanisch and J. Barnes (San Francisco: ASP), 423.

Wilkes, B. J., Kuraszkiewicz, J., Green, P. J., Mathur, S. and McDowell, J. C. 1999, *ApJ*, 513, 76.

Williams, D. M., Thompson, C. L., Rieke, G. H. & Montgomery, E. F. 1993, *Proc. SPIE*, 1308, 482.

Williger, G. M., Carswell, R. M., Webb, J. K., Boksenberg, A. & Smith, M. G. 1989, *MNRAS*, 237, 635.

Willner, S. P., Elvis, M., Fabbiano, G., Lawrence, A. & Ward, M. J. 1985, *ApJ*, 299, 443.

Wills, B. J., Netzer, H. & Wills, D. 1985, *ApJ*, 288, 94.

Wisotzki, L., Christlieb, N., Bade, N., Beckmann, V., Köhler, T., Vanelle, C. & Reimers, D. 2000, *A&A*, 358, 77.

Wisotzki, L. 2000, *A&A*, 288, 94.

Zheng, W. & Malkan, M. A. 1993, *ApJ*, 415, 517.

Zheng, W., Kriss, G. A., Telfer, R. C., Grimes, J. P. & Davidsen, A. F. 1997, *ApJ*, 475, 469.

Fig. 1.— Absolute magnitudes, M_V , and redshifts, z , of the quasars in the high and low redshift samples (solid squares). The M_V are computed for $H_o = 50 \text{ km s}^{-1} \text{ Mpc}^{-1}$ and $q_o = 0.5$ to match the parameters assumed by Boyle et al. (1988), whose model for luminosity evolution was referred to in the sample selection, although, as stated in the text, we subsequently adopt $H_o = 75 \text{ km s}^{-1} \text{ Mpc}^{-1}$ and $q_o = 0.1$. The thick solid lines indicate tracks of pure luminosity evolution for $L/L^* = 1.2$ and 7.4, where these values span the range for all but one of the quasars in the high redshift sample and correspond to $M_V = -29.5$ and -27.5 , respectively. $L^* \sim (1+z)^k$ ($k = 3.15$; Boyle et al. 1988), so at $z \sim 0.1$, these tracks delimit a range for the ‘matching’ low redshift sample of $M_V = -22.75$ to -24.75 . The thin dashed lines mark curves of constant apparent magnitude, m_V , where, following Véron-Cetty and Véron (1993), the k -correction was made assuming an optical/UV spectral index, $\alpha = -0.7$ ($F_\nu \sim \nu^\alpha$) and the wiggles near redshifts 2 and 3 arise from strong emission lines of Ly α and CIV entering and leaving the V band.

Fig. 2.— The three panels, from top to bottom, illustrate, for Q2126 – 158, the steps taken to correct for suppression of the UV continuum by ‘Ly α forest’ absorption. In the top panel, the high resolution spectrum is binned and smoothed (thick curve) to approximate the resolution of the spectrophotometry (thin curve), and the spectrophotometry shifted to match the wavelength calibration of the high resolution data. The middle panel shows the ratio of the binned and smoothed high resolution spectrum to the shifted spectrophotometry and the best-fitting polynomial, termed the ‘correction function’. In the bottom panel, the corrected continuum (thick curve), *i.e.* the product of the continuum fit to the high resolution spectrum and the ‘correction function’, is plotted with the shifted spectrophotometry (thin curve) for comparison. Note that the levels match well to the red of Ly α , but on the blue side, the corrected continuum flux is larger (by a factor of ~ 1.5 for this quasar) than the level of the spectrophotometry.

Fig. 3.— Optical/UV spectral energy distributions of the 15 high redshift sample quasars. The optical spectrophotometry and IR spectra, scaled by the photometric data as described in §5.1, are plotted, together with the average luminosities computed within each of the 9 narrow bands between 1285Å and 5100Å. The symbols indicate how well the computed luminosity is believed to represent the continuum: solid squares mark the luminosities computed directly from the data and well representative of the continuum level (Q=3 in Tables 15 and 16); empty squares mark those which, though interpolated, seem to represent the continuum well (Q=2); and x's mark those that are not well representative of the continuum (Q=1) and those determined at 2500Å, which was not defined as a ‘continuum’ window. At wavelengths shorter than Ly α , the corrected continuum is plotted over the spectrophotometric data with a thicker line, and average fluxes at 1115Å and 1160Å, computed for the corrected and uncorrected data, are plotted (open circles for corrected continua, x's for uncorrected). The power law fits made through the 5 narrow band fluxes on either side of the 2000 – 4000Å small bump region, are plotted as dashed lines. Note that the corrected spectra nearly reach the extrapolated power law for some objects (Q0000 – 263, Q0420 – 388, Q0636 + 680) but fall short for others (Q0014 + 813, Q1208 + 101, Q1946 + 7658 and Q2126 – 158), as discussed in §9.1. For comparison, the average radio-quiet or radio-loud low redshift spectral energy distribution (Elvis et al. 1994), normalized to match the quasar’s 1460Å luminosity, is overplotted (dotted line).

Fig. 4.— Spectral energy distributions for 4 high redshift sample quasars detected at L', 2 of which, Q0014 + 813 and Q1946 + 7658, also have interesting upper limits at N. Optical spectrophotometry, IR spectra and corrected $\lambda < \lambda(\text{Ly}\alpha)$ continua are plotted as in Figure 3, with the addition here of optical and IR photometry and upper limits (solid squares). As in Figure 3, the appropriate (radio-loud or radio-quiet) mean, low redshift, SED is overplotted for comparison (dotted line) as well as the power law fit (dashed line).

Fig. 5.— The locations of the 12 narrow bands chosen for this study (defined in Table 14) are marked with reference to the SED of one of the high redshift sample quasars, Q0636 + 680 at $z = 3.18$.

Fig. 6.— Residuals of single power law fits to the narrow band average continuum luminosities between 1285-5100Å, excluding the four between 2000Å and 4000Å where FeII+BaC emission (the 3000Å small bump) contributes. Symbols are as in Figure 3 except that all 4 bands between 2000 and 4000Å are indicated by an ‘x’ in addition to the symbol used to signify how the luminosity was determined (solid square — directly or open squares — by interpolation) and its quality (x — poorly determined). For most of the low redshift AGN, the 2000-4000Å residuals indicate excess emission within this region, but this feature is weak or absent among the high redshift quasars, as discussed in §9.2.

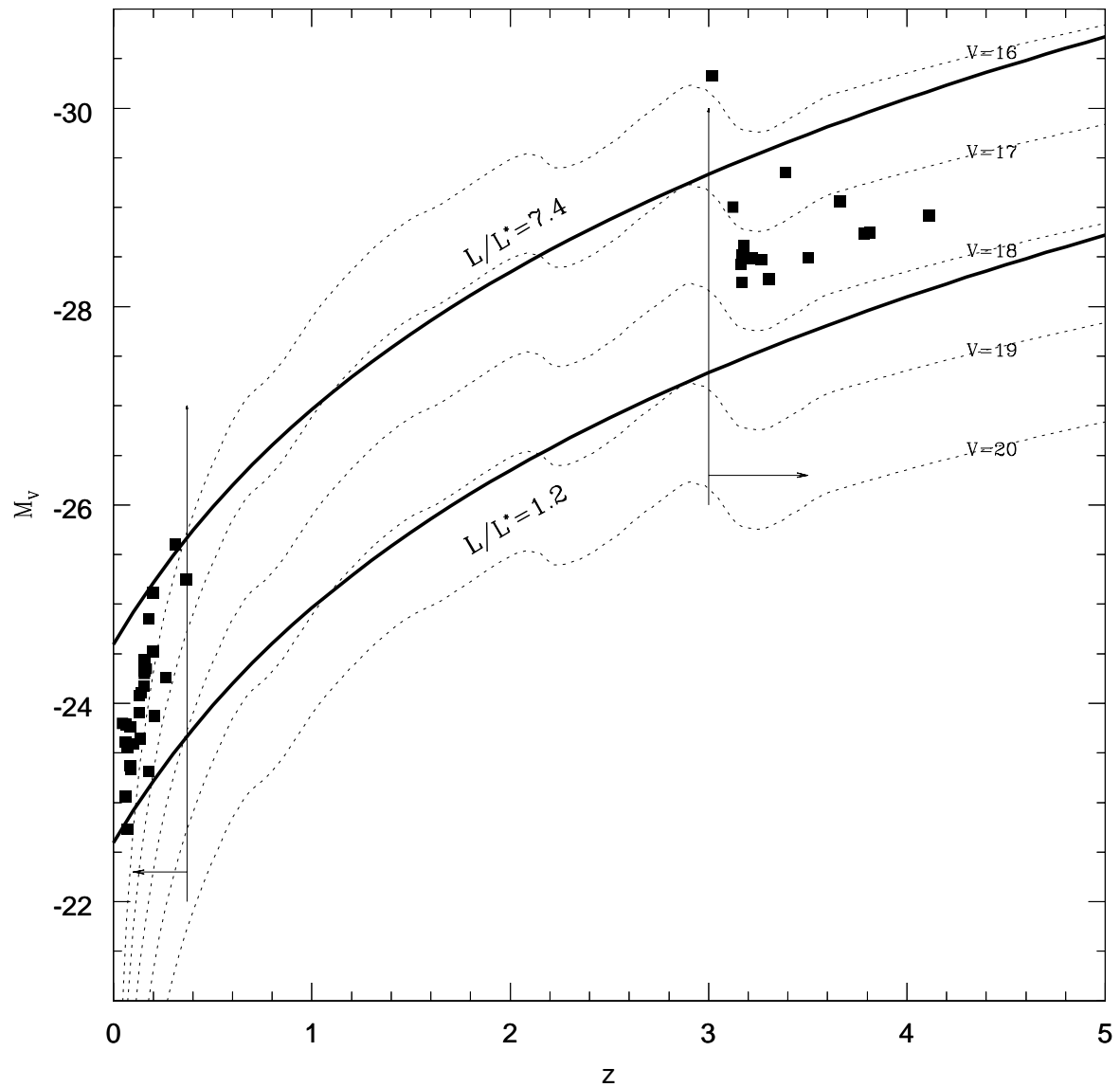
Fig. 7.— The histograms show the distributions of optical/UV spectral indices for the high and low redshift samples, computed using the narrow band luminosities between 1285Å and 5100Å but excluding those 4 within the ‘small bump’ region. In (a) and (c), error histograms are inset. In (b) and (d), the scale indicates the E(B-V) needed, assuming both Milky Way and SMC extinction laws, to redden a $\nu^{1/3}$ power law by a given amount. To cover the range of spectral indices ($\Delta\alpha_{ouv} \approx 1$) would require E(B-V) ≈ 0.11 (SMC) or 0.25 (MW).

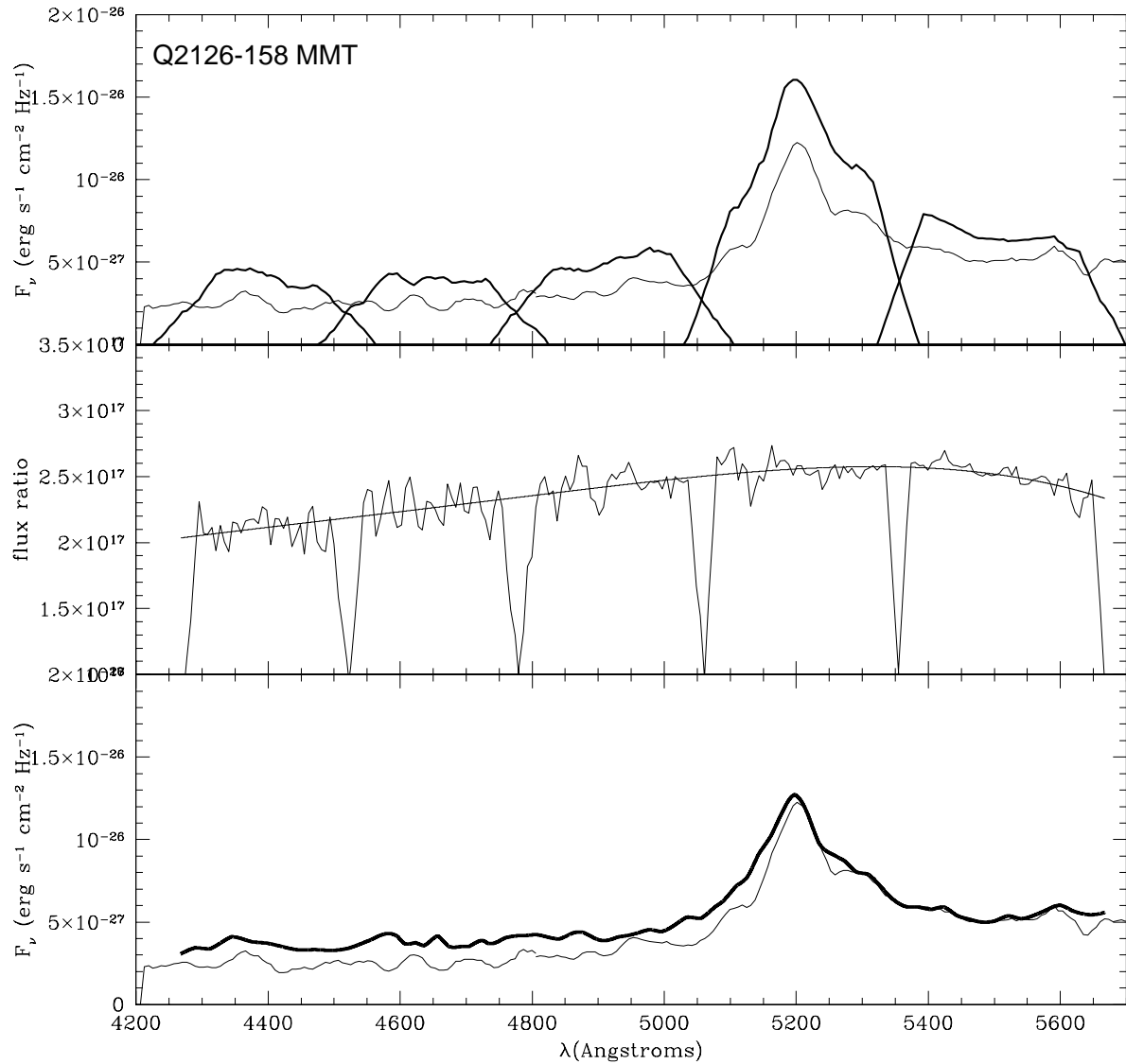
Fig. 8.— UV spectral indices, α_{uv} , plotted against luminosity at 1460Å, $\log\nu L_\nu(1460\text{\AA})$ (a) and redshift, $\log(1+z)$ (b). In both figures the filled symbols and solid thick error bars are used for the $\alpha_{uv}(1285\text{-}2200\text{\AA})$, and the open symbols and dotted error bars, for the $\alpha_{uv}(1285\text{-}1460\text{\AA})$. The solid lines show the best linear fit between the 1285-2200Å spectral indices and $\log L$ or $\log(1+z)$ while the dotted lines mark the best fits determined using the 1285-1460Å spectral indices instead.

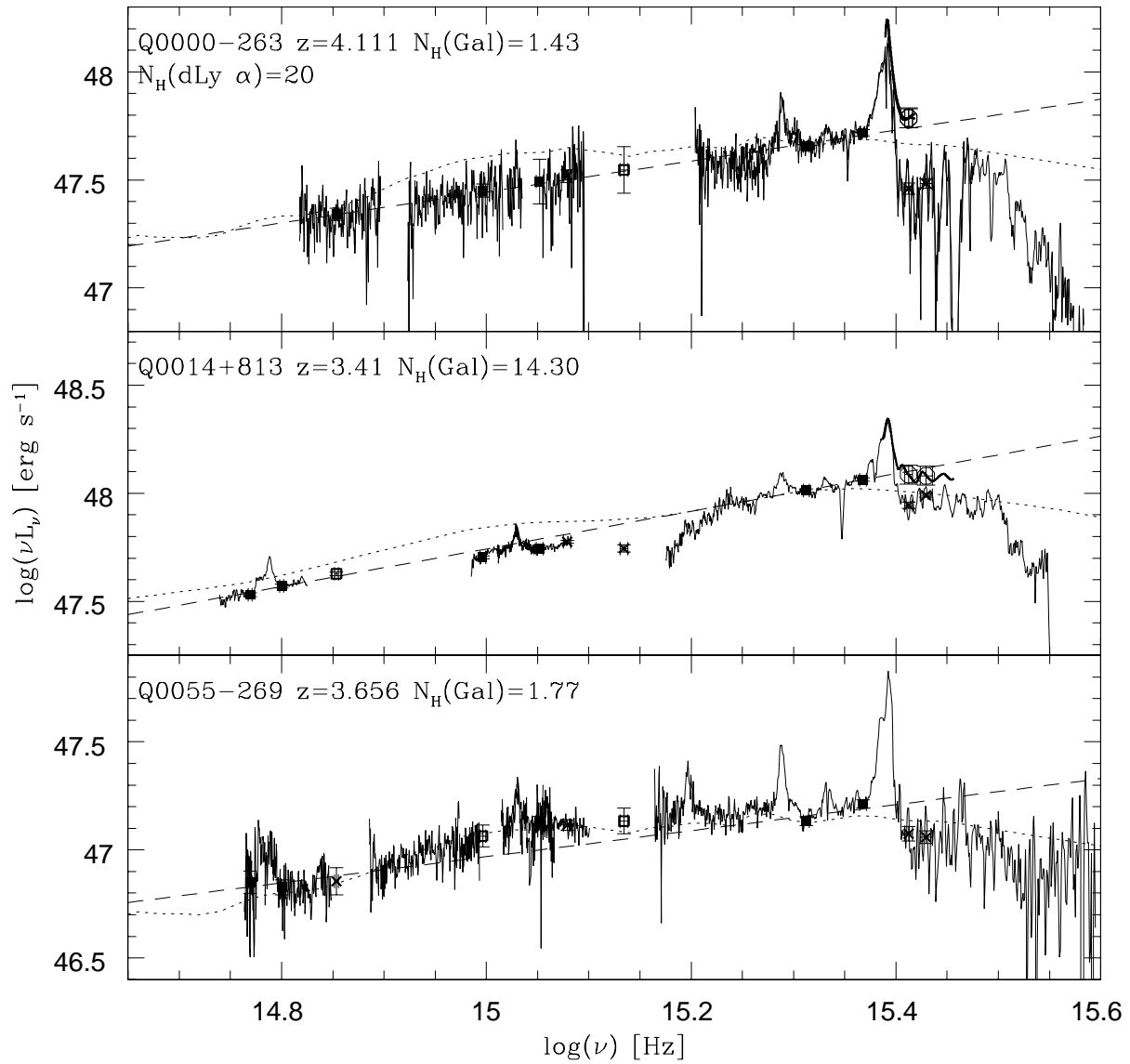
Fig. 9.— Optical/UV 1285-5100Å spectral indices, α_{ouv} , plotted against UV ($\log\nu L_\nu(1285\text{\AA})$; solid circles) and optical ($\log\nu L_\nu(4200\text{\AA})$; open circles) luminosities for the low redshift sample. The solid line indicates the best fit between α_{ouv} and $\log\nu L_\nu(1285\text{\AA})$ and the long-dashed line, the best fit between α_{ouv} and $\log\nu L_\nu(4200\text{\AA})$. The short-dashed lines connect optical and UV luminosities for the same object, and illustrate the movement away from a slope-luminosity correlation when the luminosity is measured in the optical rather than the UV. There is good evidence for a correlation between the optical/UV continuum shape and UV, but not optical, luminosity for the low redshift sample and marginal evidence that it is present also in the combined low and high redshift samples, though not within the high redshift sample alone.

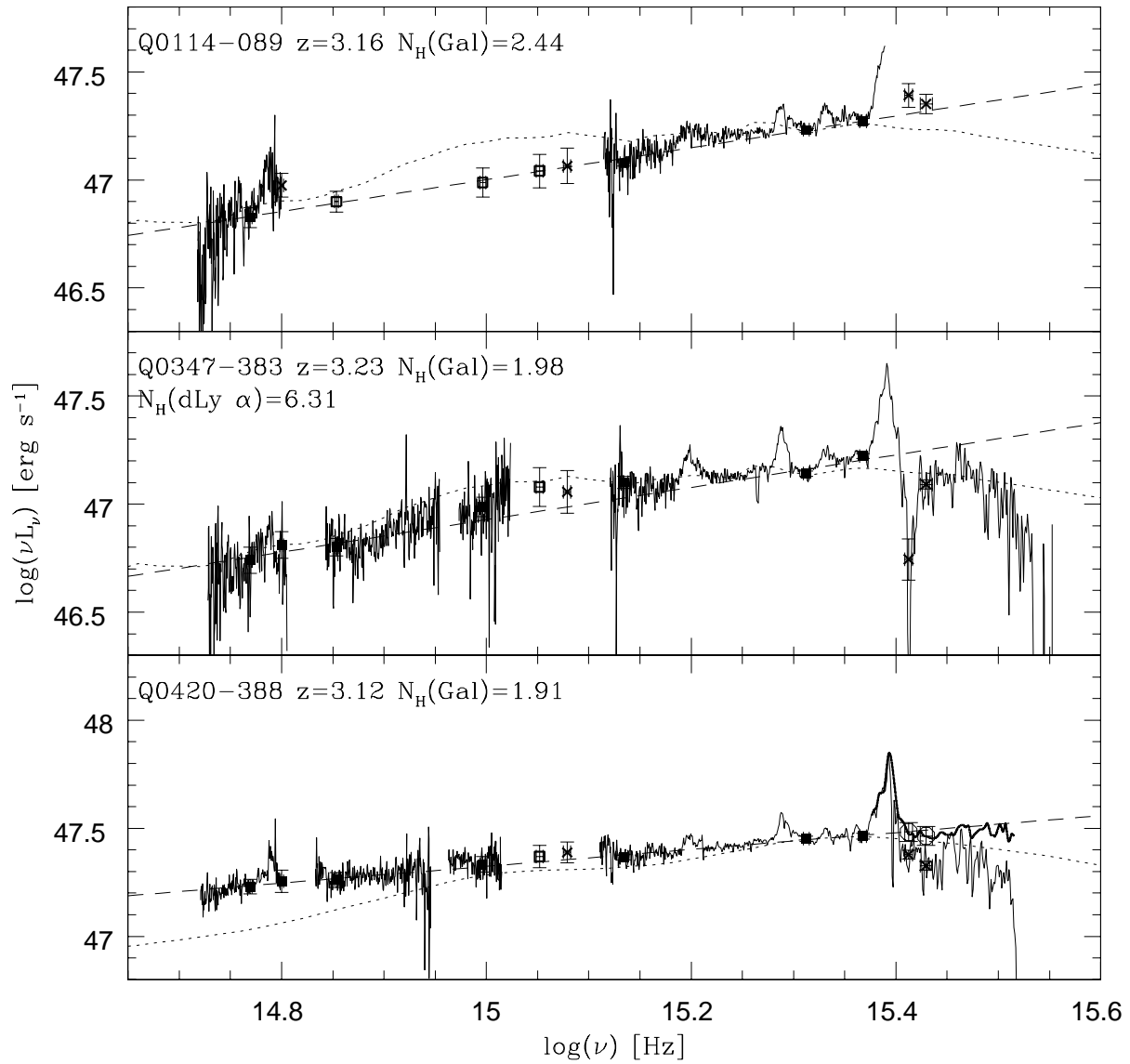
Fig. 10.— The influence of host galaxy starlight in the correlation between optical/UV slope and optical luminosity is illustrated in this figure where the spectral indices from 1285-6500Å and absolute magnitudes at 4800Å are plotted for 46 low redshift AGN from the ‘Atlas’ (Elvis et al. 1994a), before (open squares) and after (solid squares) subtracting the host galaxy starlight contribution. There is a weak correlation between spectral index and luminosity when the host galaxy contribution is not removed (Spearman correlation coefficient, $r_s = -0.32$ with a 3% probability, p_s , of a chance correlation). Subtracting it effects the lowest luminosity AGN most, and there is no evidence for slope-luminosity correlation in the resulting distribution ($r_s = 0.13$, $p_s = 37\%$). Linear least squares fits to the data before (dotted) and after (solid) host galaxy subtraction are shown.

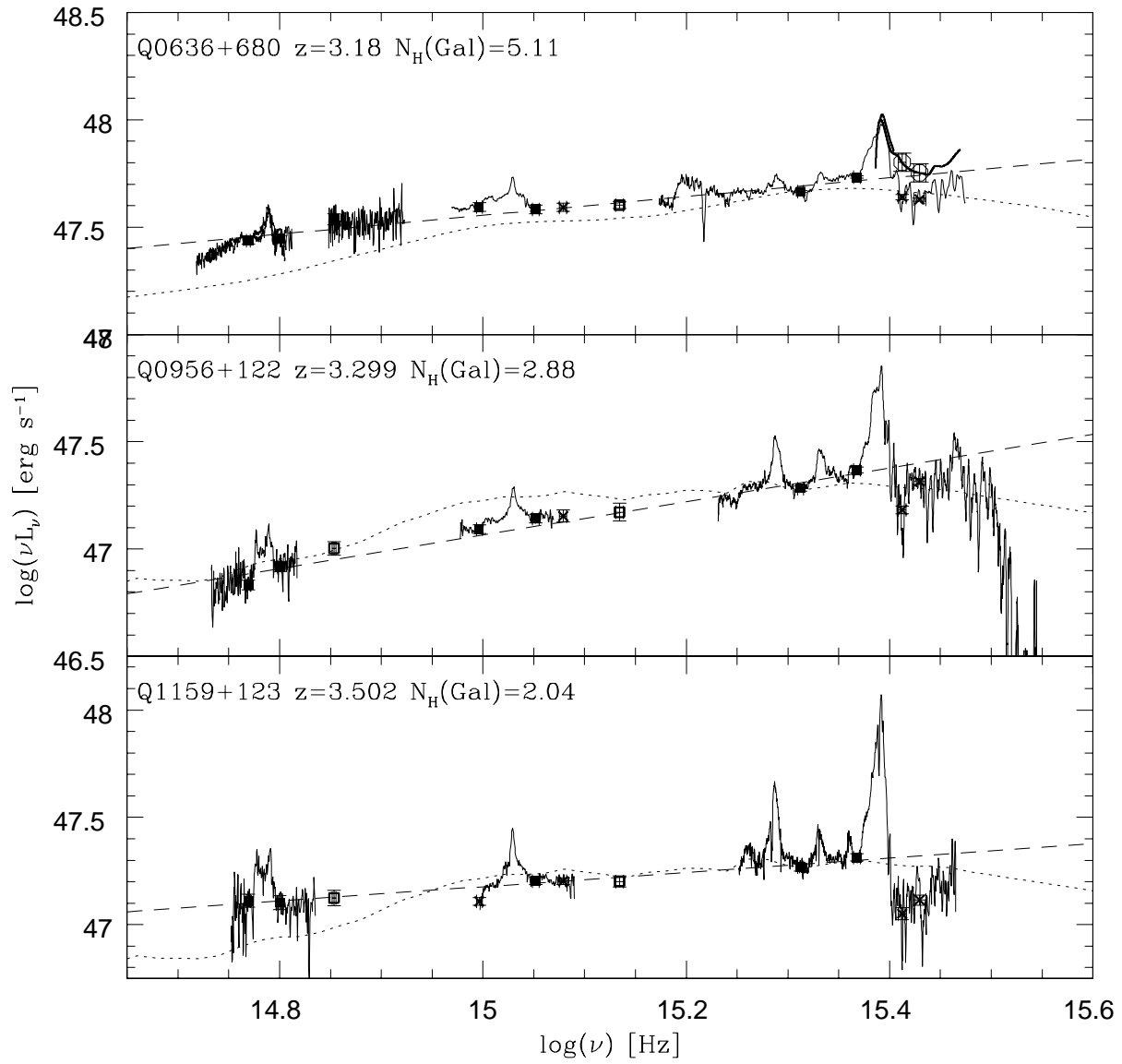
Fig. 11.— Evolution of the 3000Å bump with redshift. The histograms show the distributions of the residuals at 2500Å and 2660Å, the ratios of the excess to continuum luminosity between 2200Å and 3023Å, and the 2200–3023Å equivalent widths (as defined in the text) for the objects from the high and low redshift samples. Only those measures which do not rely solely on interpolated fluxes or include discrepant flux points (*i.e.* all values not in parentheses in Table 23) are plotted and used in the sample comparisons, but the distributions which include the measures for all objects do not differ significantly from these. The high redshift quasars have significantly weaker 3000Å bumps than the low redshift ones, as evidenced by all four measures.

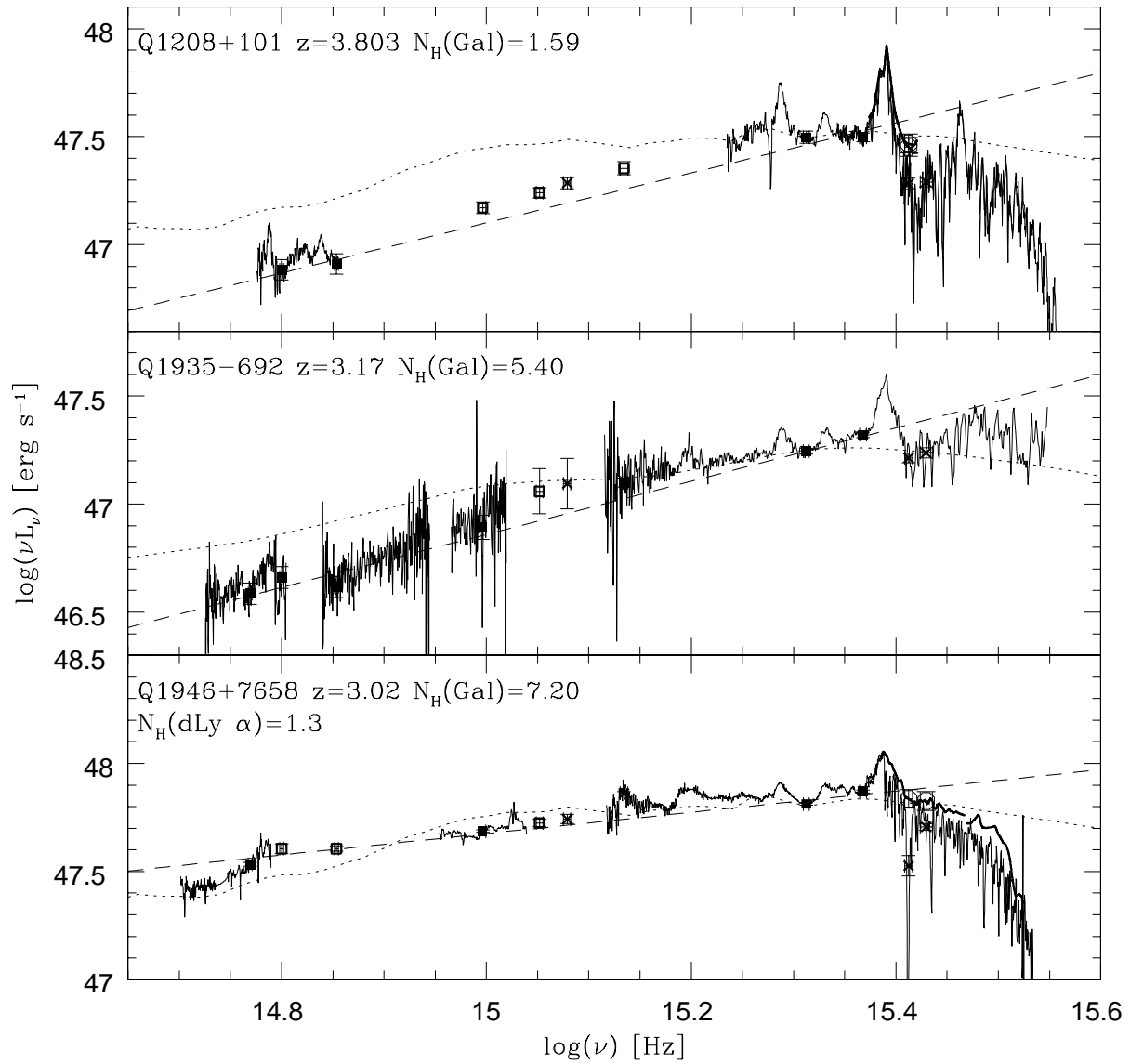


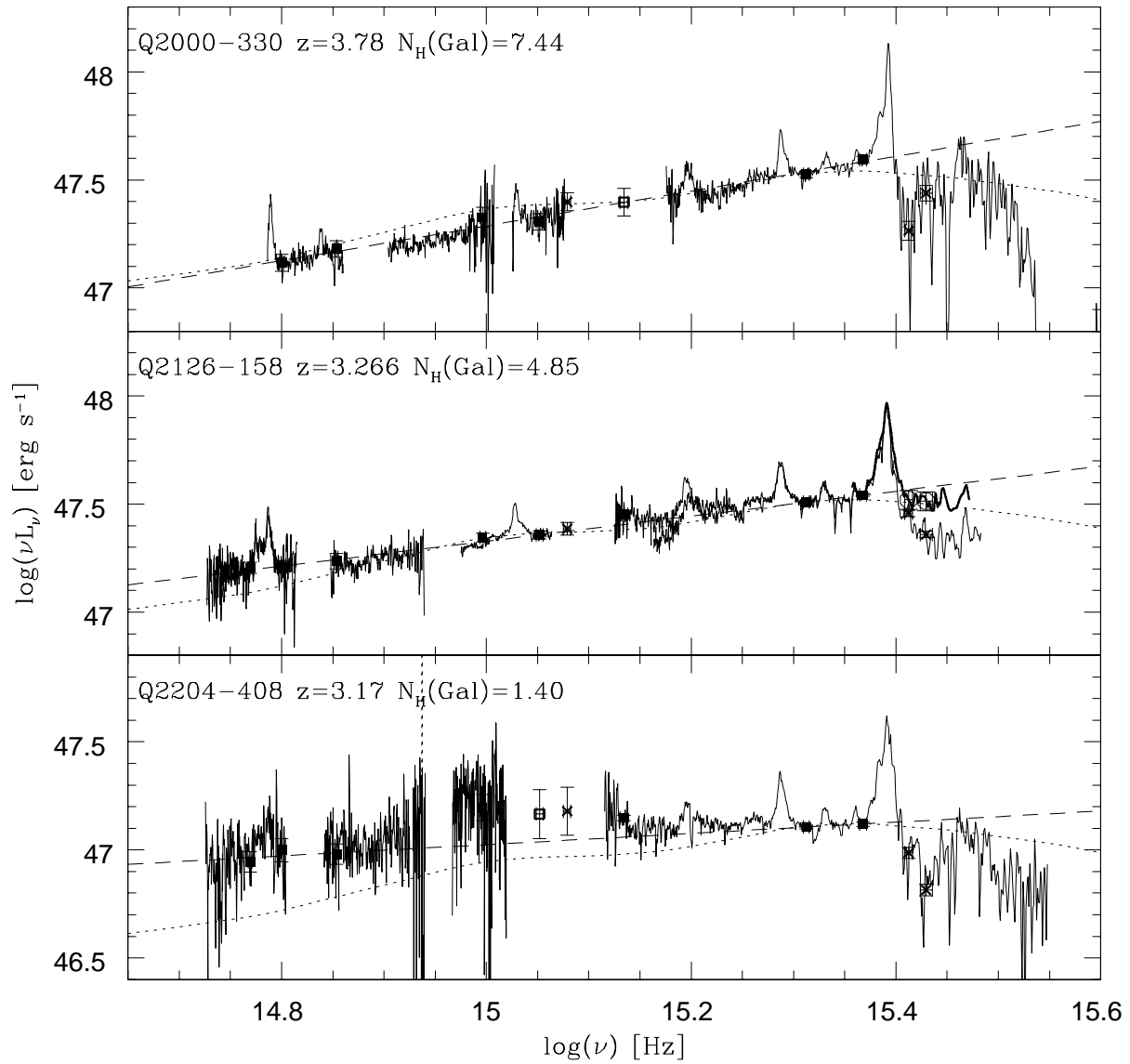


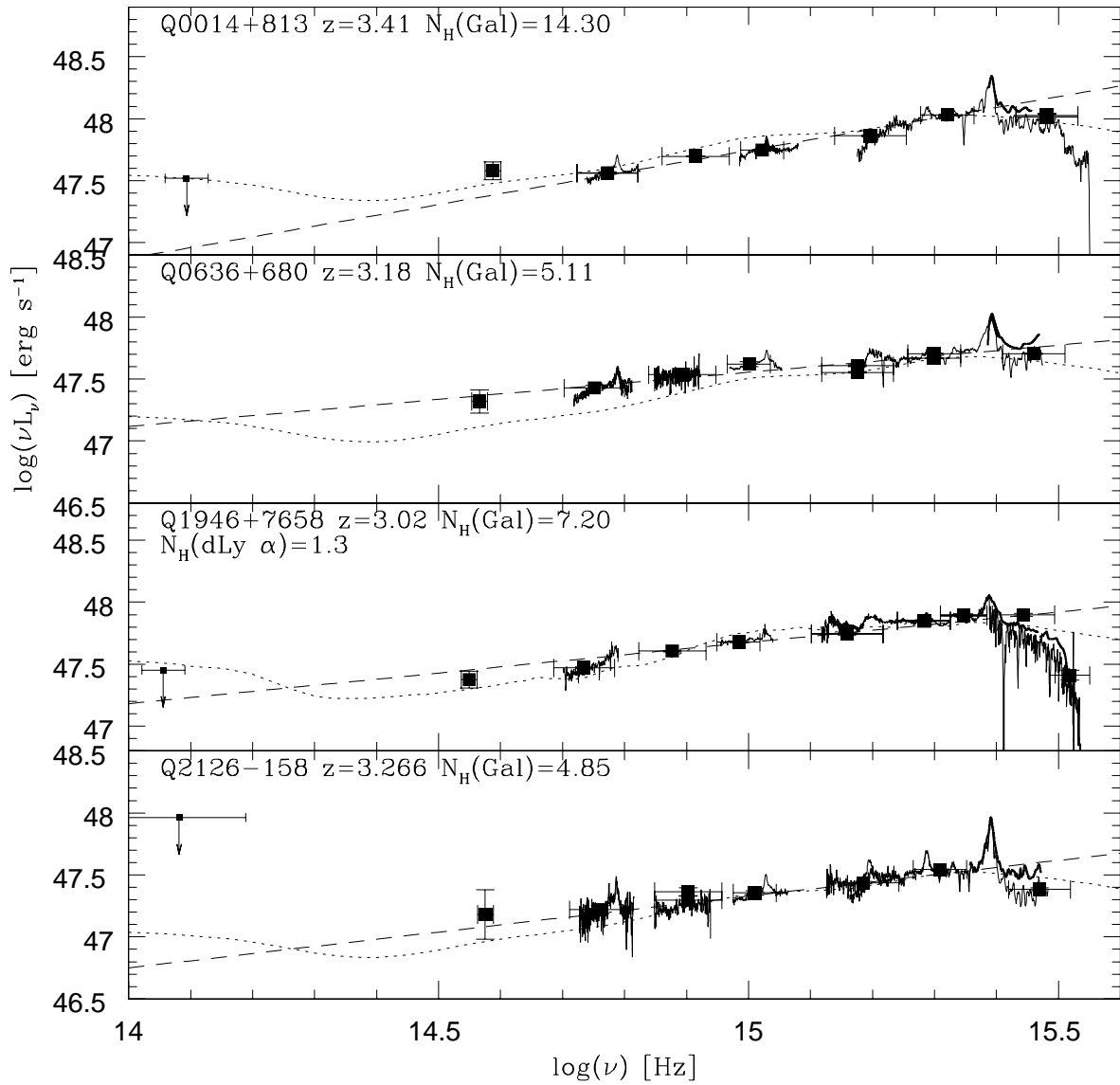


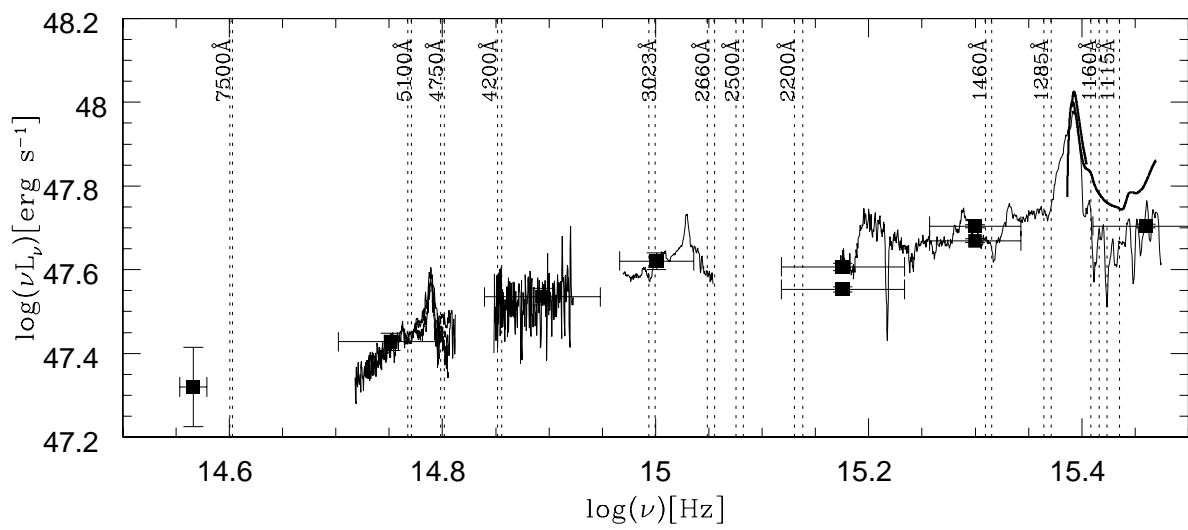


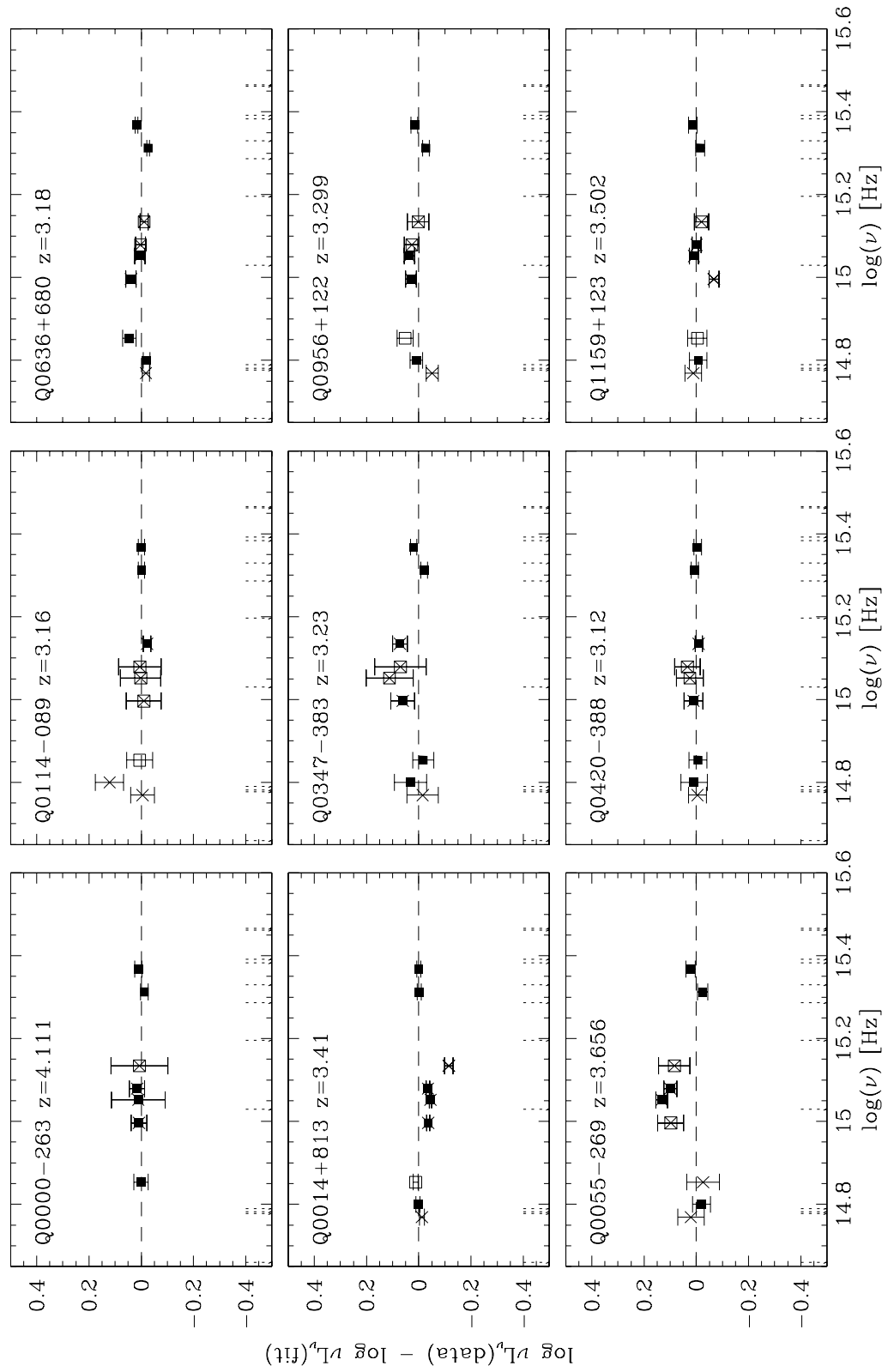


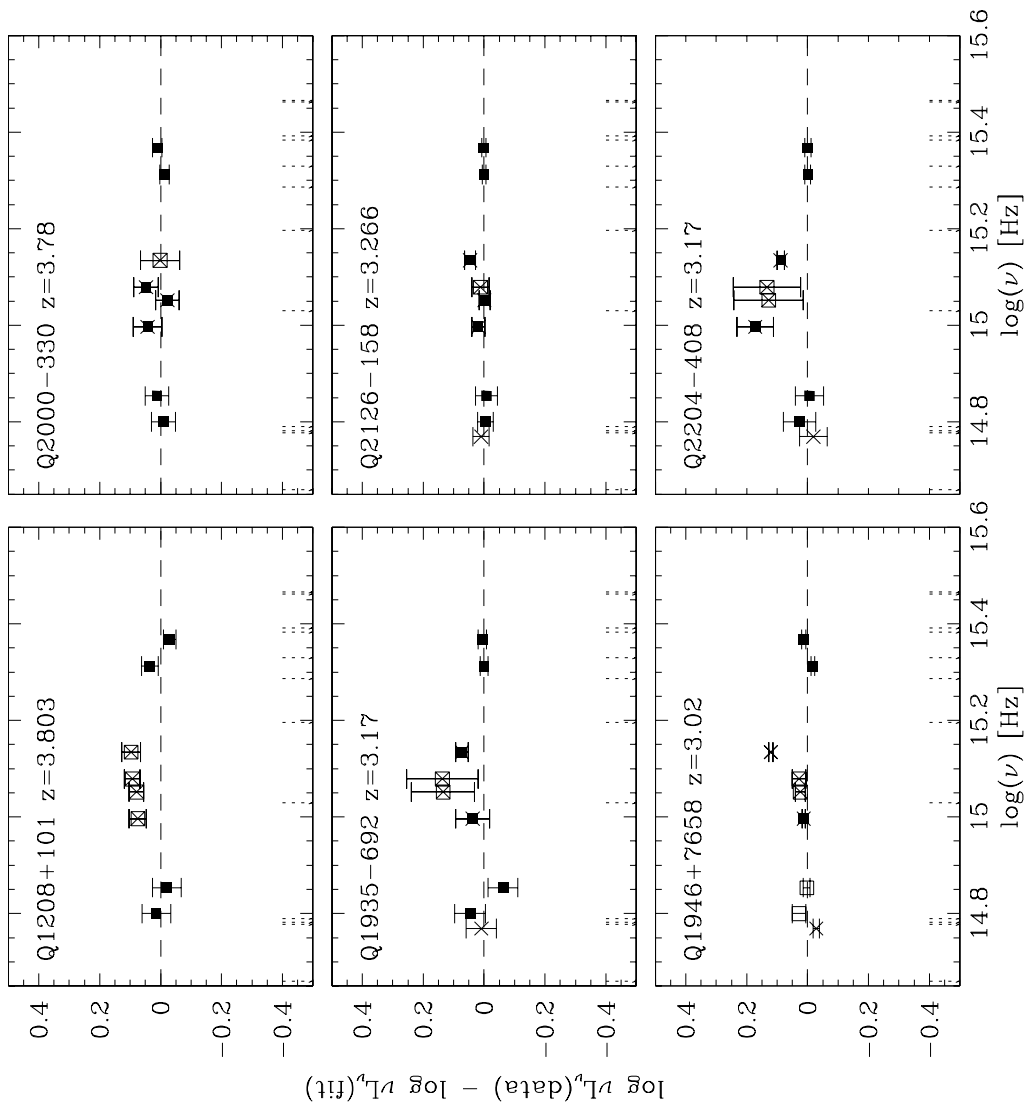


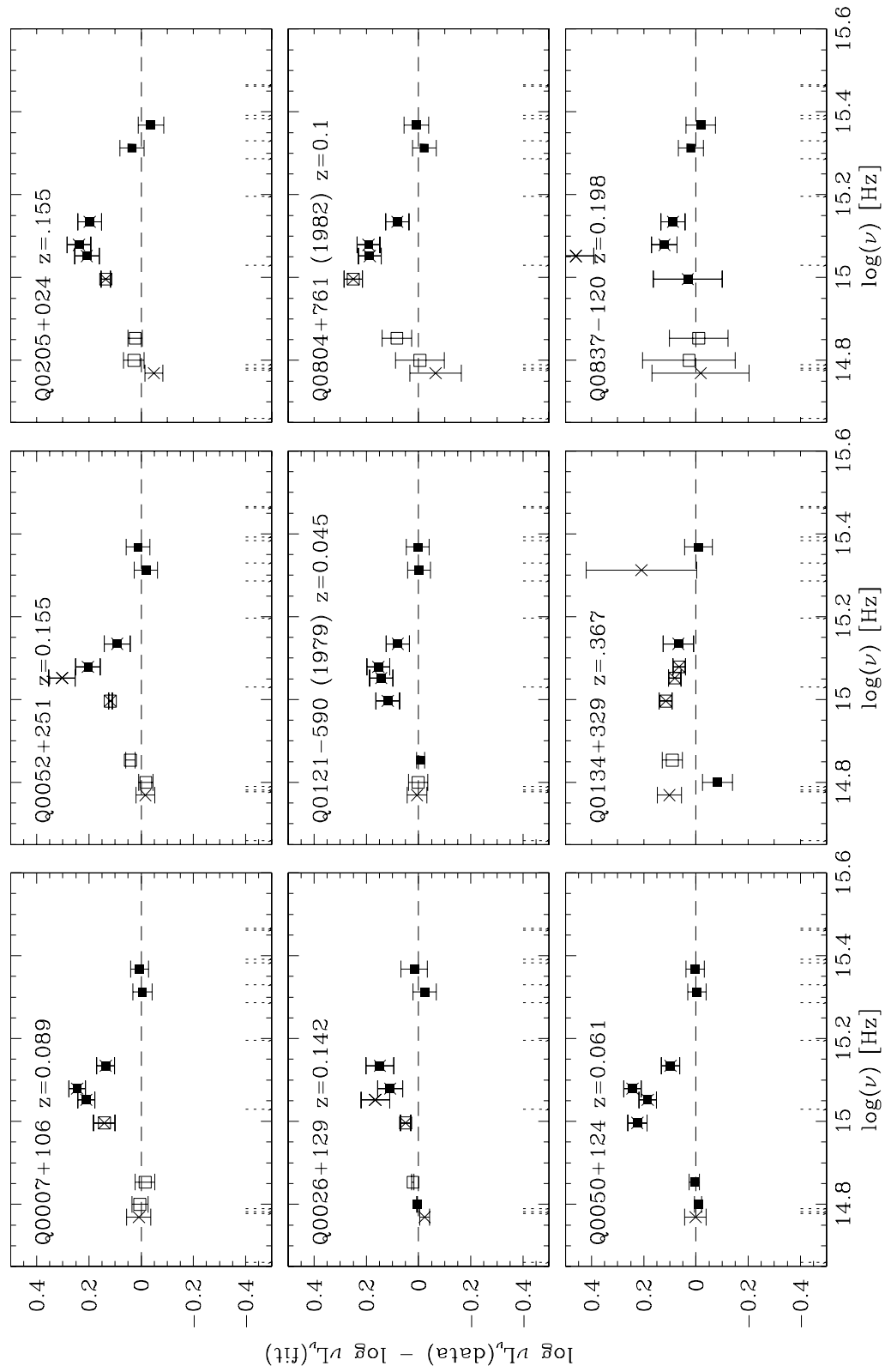


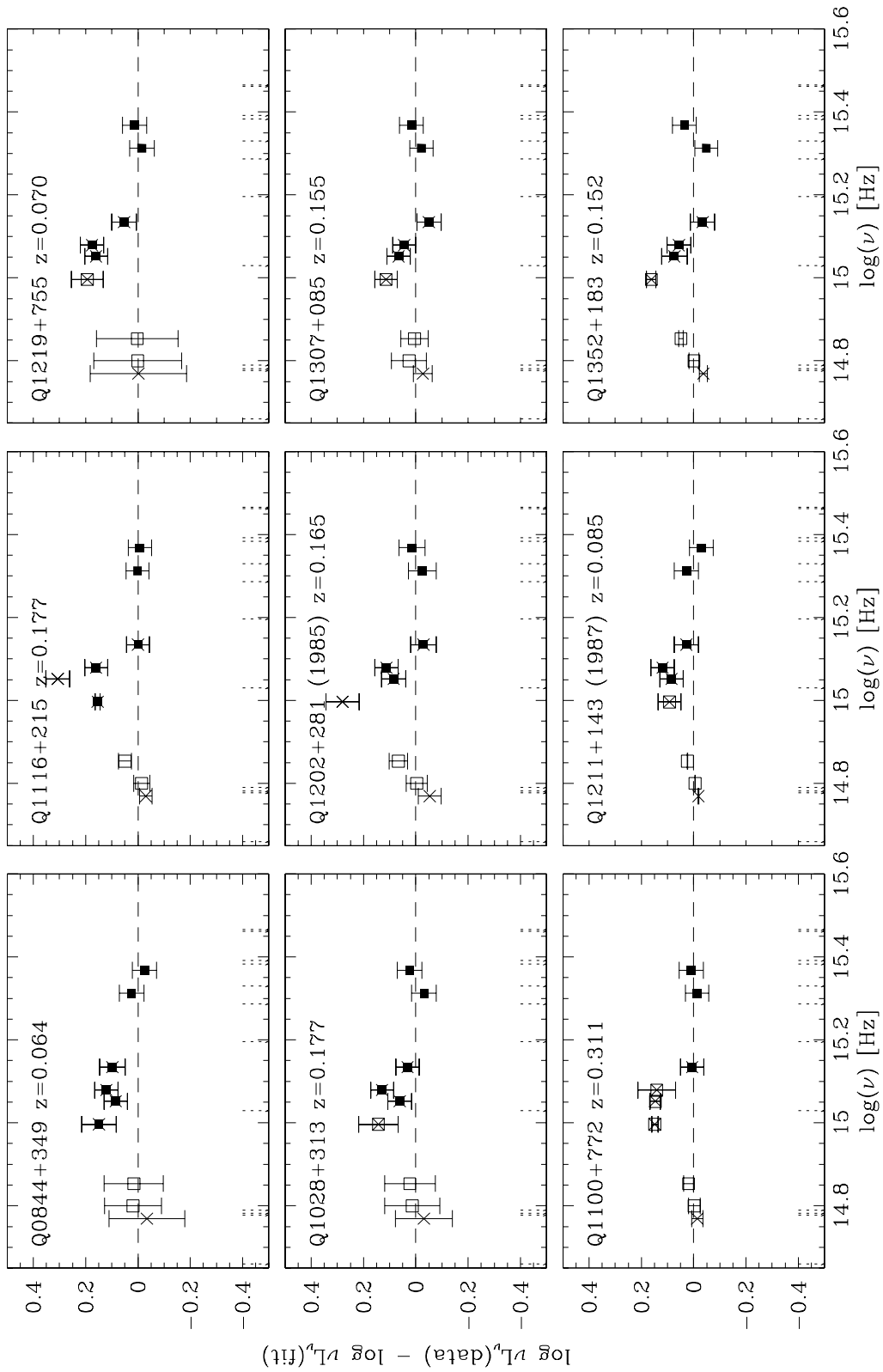


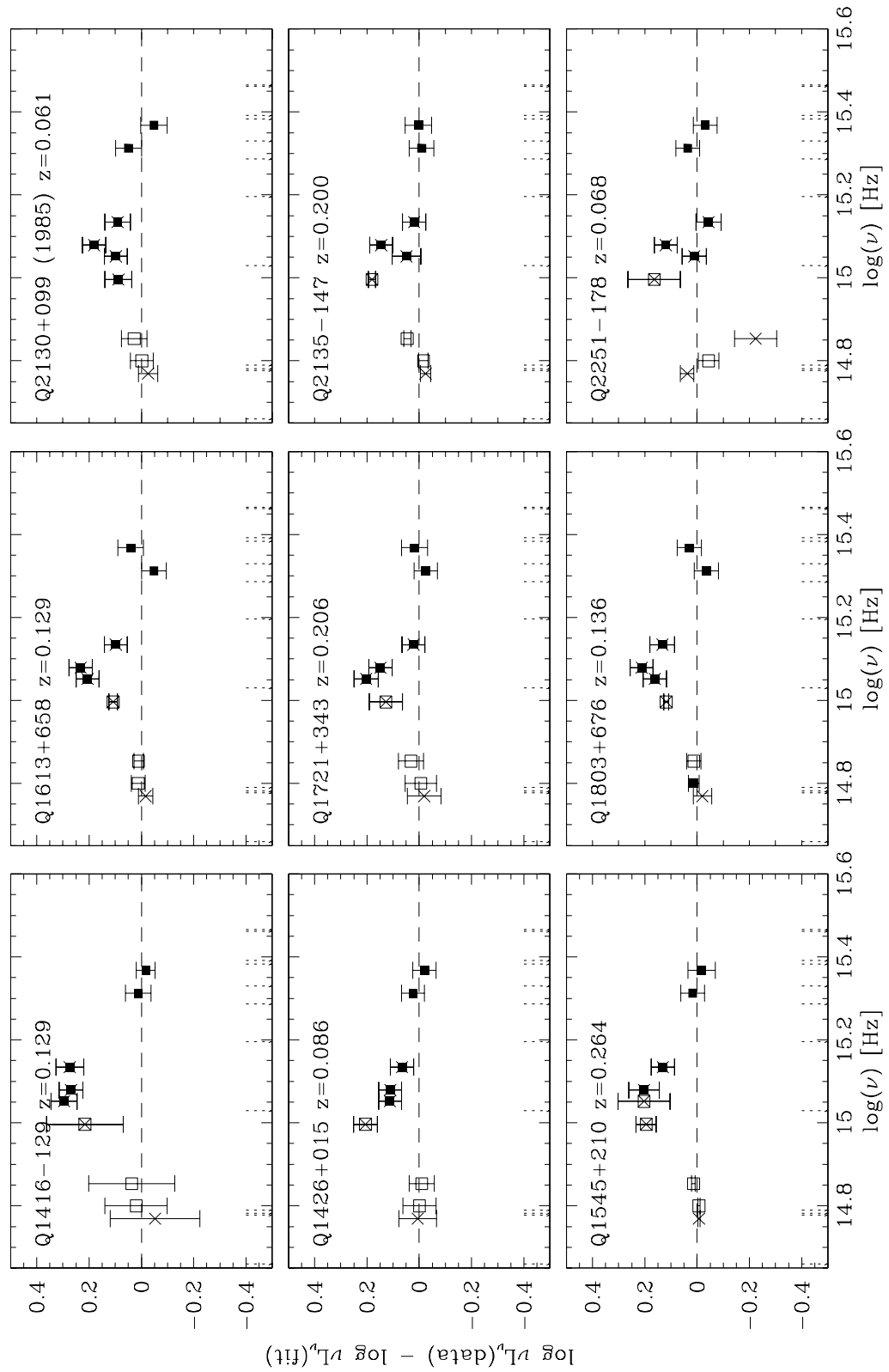


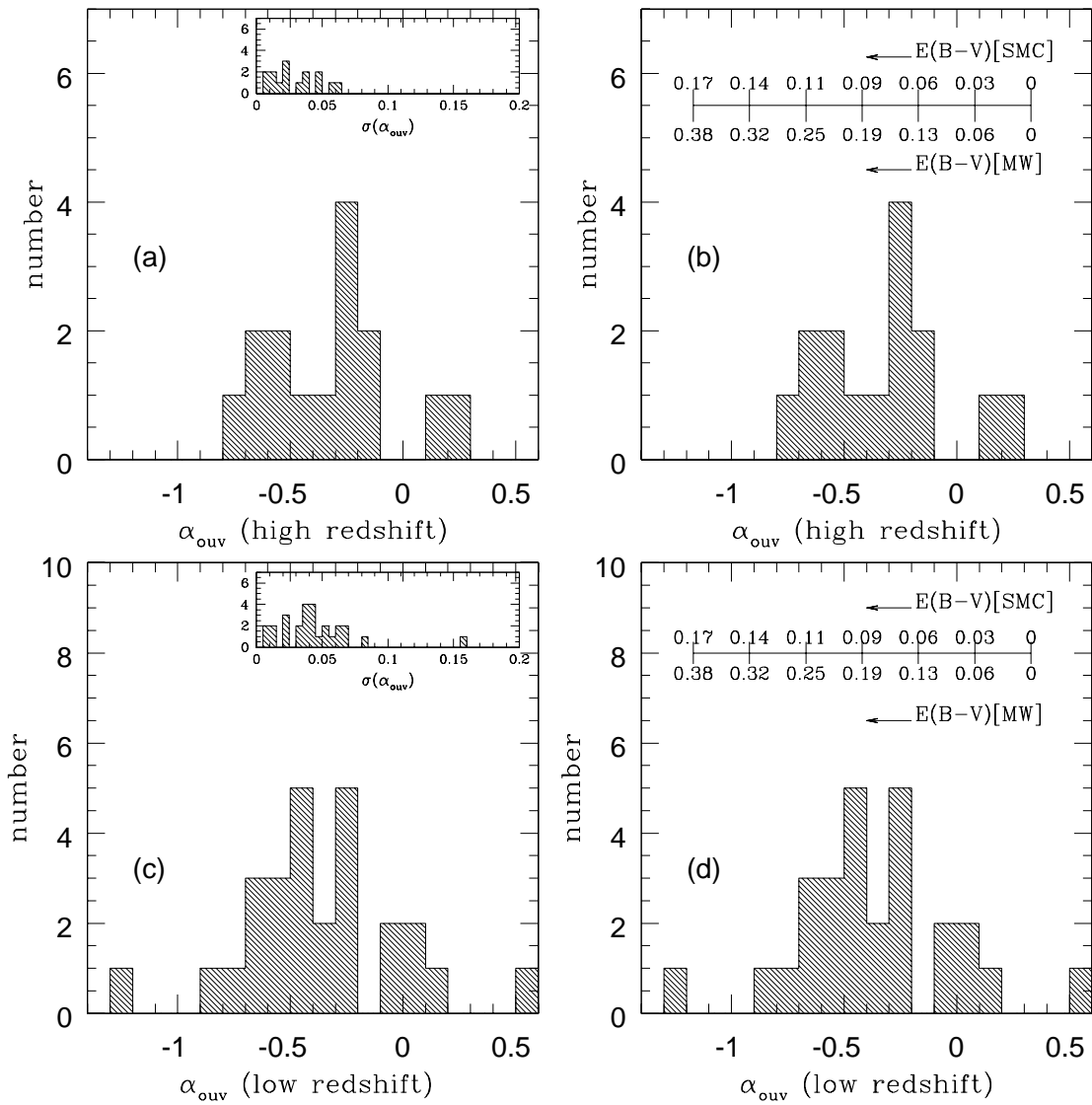


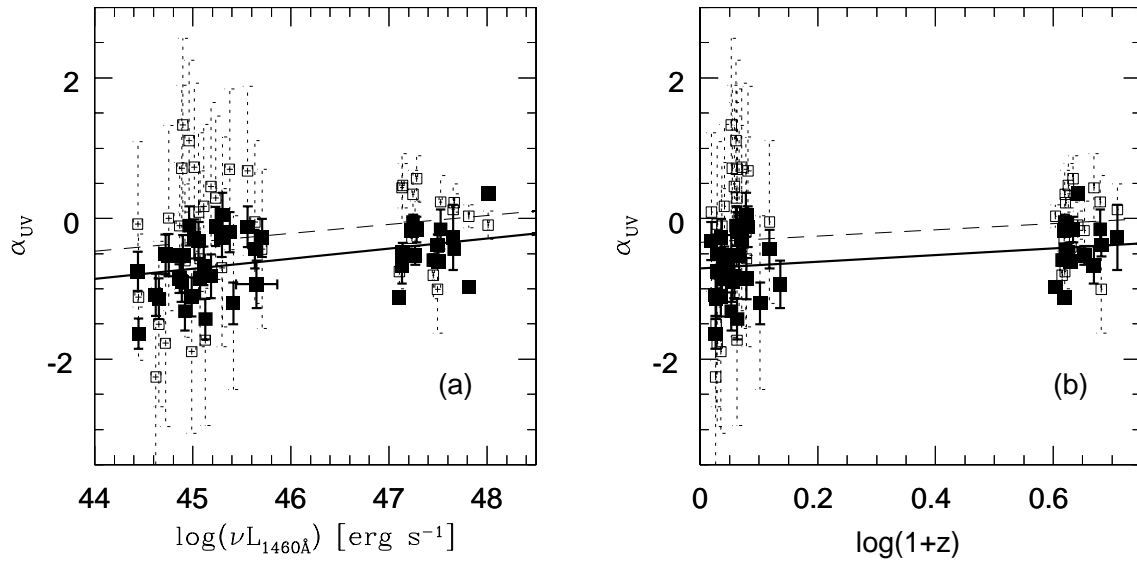


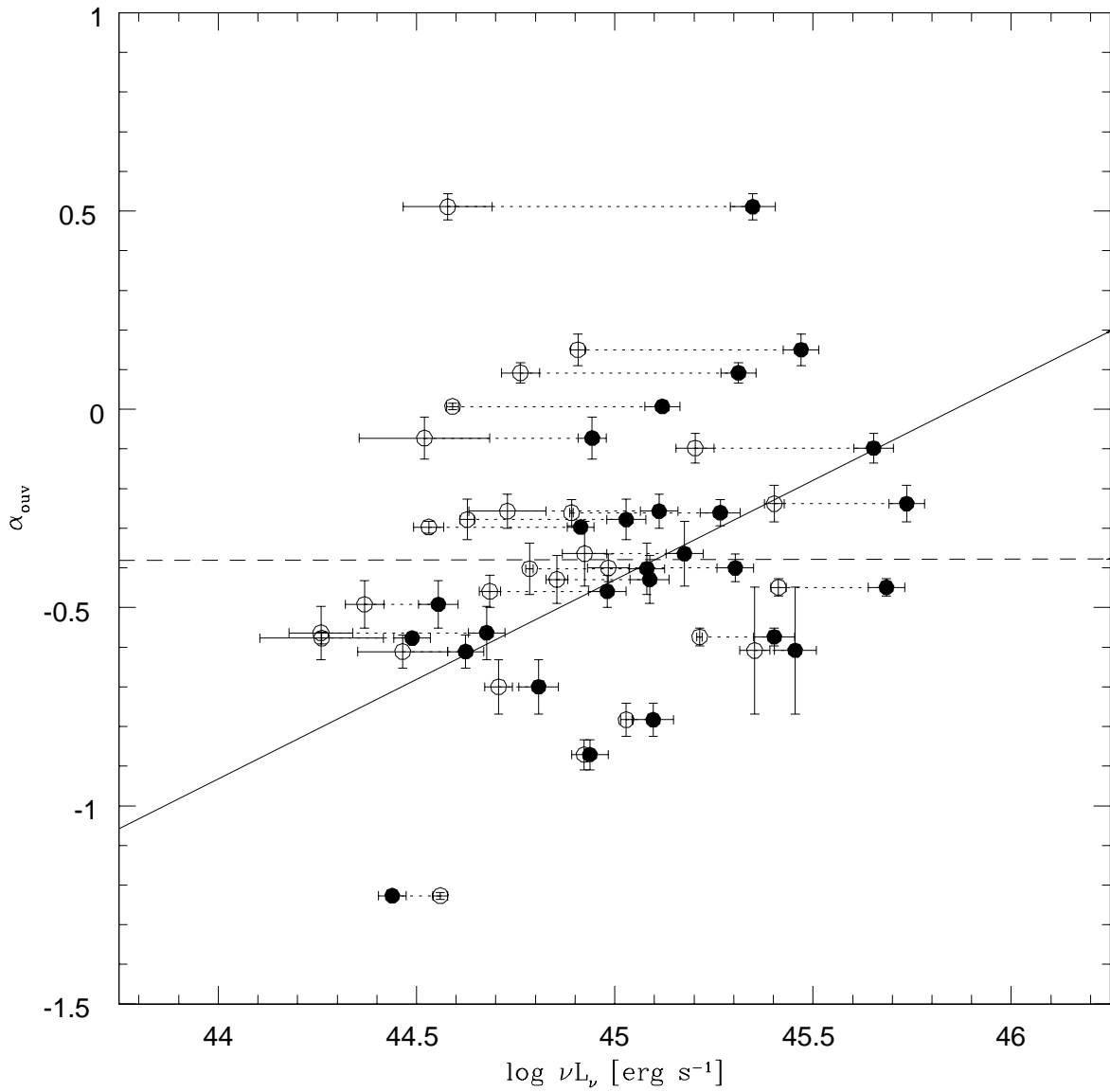


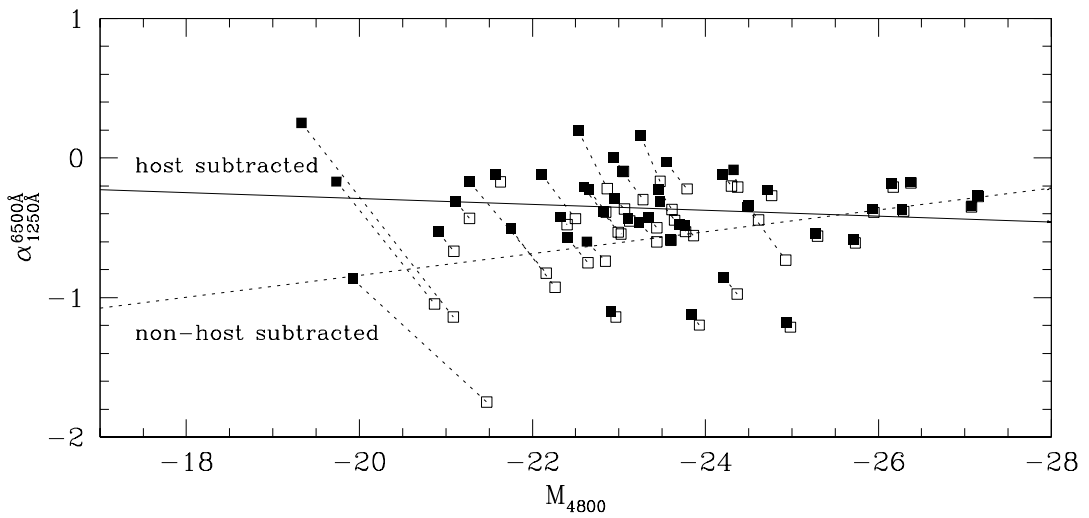












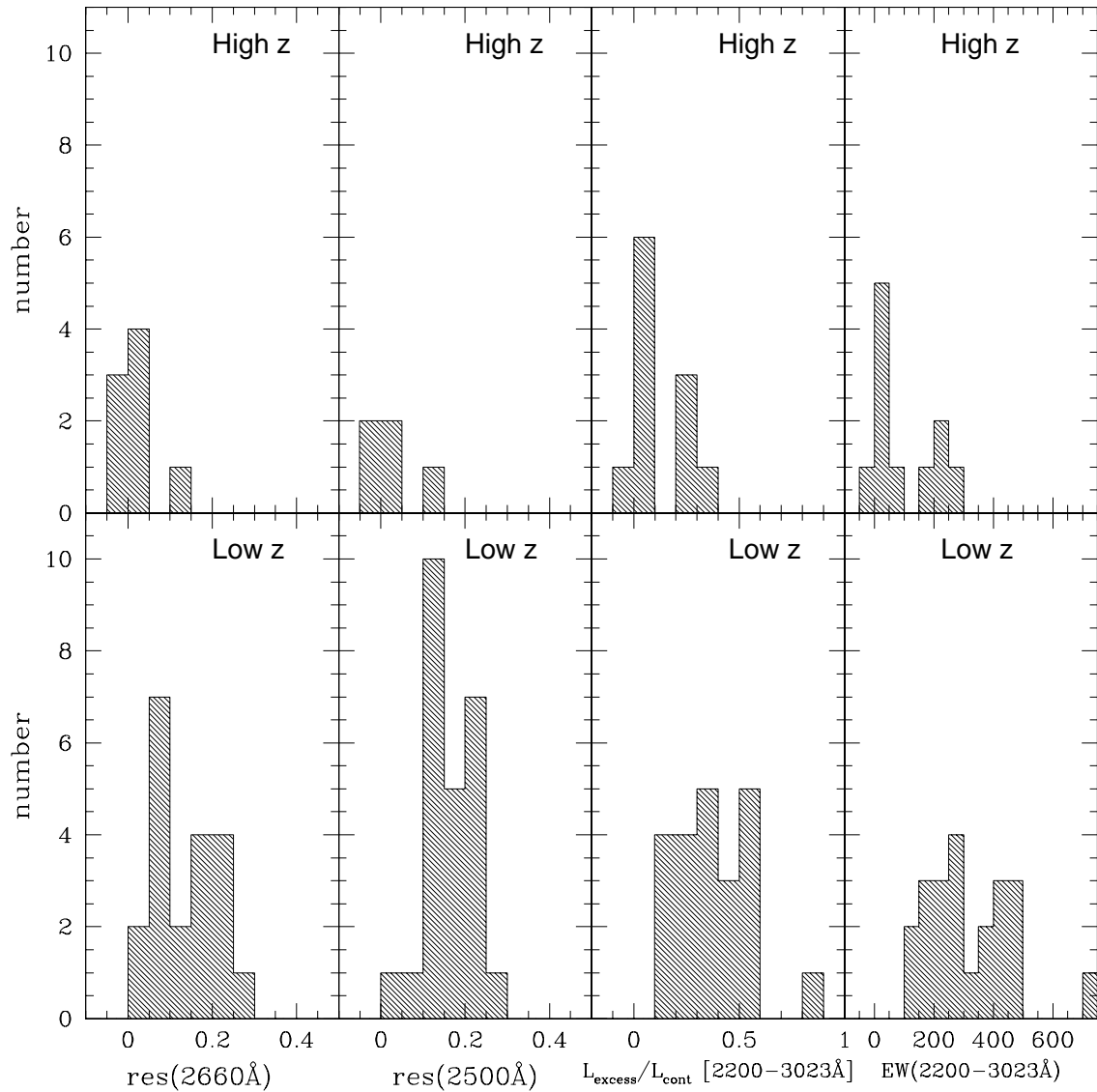


Table 1. High redshift sample

Object	Other Names	class ^a	z ^b	V ^b	α_{ox} ^c	selection ^d	used? ^e
Q0000 – 263		RQ	4.111	17.5 ^f	1.866	OBJ	✓
Q0014 + 813	S5	RL	3.3866 ^g	16.5	1.344	RAD	✓
Q0055 – 269		RQ	3.6625 ^g	17.1	...	OBJ	✓
Q0114 – 089	UM670	RQ	3.1626 ^g	17.4	...	OBJ	✓
Q0130 – 403		RQ	3.03	17.02	1.713	OBJ	X
Q0347 – 383		RQ	3.222 ⁱ	17.3	...	OBJ	✓
Q0351 – 390		RQ	3.01	17.9	...	OBJ	X
Q0420 – 388A		RL	3.123 ^j	16.92	1.506	OBJ	✓
Q0636 + 680	S4	RL	3.1775 ^g	17.2 ^m	1.679	RAD	✓
Q0956 + 122		RQ	3.306	17.5	...	OBJ	✓
Q1107 + 487	SP	RQ	3.01 ^h	16.9 ^h	1.809	OBJ	X
Q1159 + 123		RQ	3.502	17.5	> 1.688	OBJ	✓
Q1206 + 119		RQ	3.106	17.90	...	OBJ	X
Q1208 + 101		RQ	3.811 ⁱ	17.5	1.818	OBJ	✓
Q1358 + 391	SP 1	RQ	3.3	17.0	...	OBJ	X
Q1442 + 101	OQ172	RL	3.535	17.78 ^k	...	RAD	X
Q1935 – 692	PKS	RL	3.170 ^l	17.3 ^l	...	RAD	✓
Q1946 + 769	HS1946+7658	RQ	3.02	15.85	1.933	OBJ	✓
Q2000 – 330	PKS	RL	3.783 ^g	17.5 ^m	1.349	RAD	✓
Q2126 – 158	PKS	RL	3.2663 ^g	17.3	1.142	RAD	✓
Q2204 – 408		RL	3.169 ⁱ	17.57	...	OBJ	✓

^aClassification: RL = Radio Loud quasar; RQ = Radio quiet quasar.

^bRedshifts, z , and V magnitudes are taken from the catalog of Hewitt & Burbidge (1993), unless otherwise noted.

^c $\alpha_{ox} \equiv -\log(l_{opt}/l_x)/\log(\nu_{opt}/\nu_x)$ where l_{opt} and l_x are the 2500Å and 2 keV fluxes measured in the rest-frame; from Bechtold et al. (1994).

^dType of survey: radio (RAD) or objective prism (OBJ); in which the quasar was first discovered; from Hewitt & Burbidge (1993).

^e‘✓’s indicate the quasars used in the final analysis and ‘X’s indicate those omitted.

^fThe magnitude is an estimate at 6000Å from Webb et al. (1988).

^gredshift from Tytler & Fan (1992)

^hfrom our observations

ⁱredshift from Steidel (1990)

^jredshift from Lanzetta et al. (1991)

^kmagnitude from Barthel, Tytler & Thompson (1990)

^lredshift and magnitude from Jauncey et al. (1989)

^mmagnitude from spectrophotometry of Bechtold et al. (1994)

Table 2. Low redshift sample

Object	Other Names	class ^a	z ^b	V ^b	α_{ox} ^c	selection ^d	used? ^e
Q0007 + 106	PG	RL	0.089	15.16	1.33	XRAY	✓
Q0026 + 129	PG	RQ	0.142 ^f	15.41 ^f	1.35	UVX	✓
Q0050 + 124	I Zw 1	RQ	0.061	14.07	1.44	UVX	✓
Q0052 + 251	PG, HEAO	RQ	0.155	15.42	1.39	UVX	✓
Q0054 + 144	PHL909	RQ	0.171	16.70	1.34	UVX	X
Q0121 – 590	<i>in</i> Fairall 9	RQ	0.045	13.23	1.37	UVX	✓
Q0134 + 329	3CR 48, 4C 32.08	RL	0.367 ^f	16.46 ^f	1.28	RAD	✓
Q0205 + 024	NAB, Mkn 586	RQ	0.155 ^f	15.39 ^f	1.53	UVX	✓
Q0312 – 770	PKS	RL	0.223 ^f	16.10 ^f	1.16	RAD	X
Q0804 + 761	PG	RQ	0.1 ^f	15.15 ^f	1.44	UVX	✓
Q0837 – 120	3C 206, PKS	RL	0.198	15.76	1.15	RAD	✓
Q0844 + 349	PG	RQ	0.064	14.00	1.60	UVX	✓
Q1028 + 313	B2	RL	0.177	16.71	1.30	RAD	✓
Q1100 + 772	3CR 249.1, 4C 77.09 PG, S5	RL	0.311	15.72	1.40	RAD	✓
Q1116 + 215	PG, TON 1388	RQ	0.177	15.17	1.62	UVX	✓
Q1146 – 037	PKS	RL	0.341	16.90	1.22	RAD	X
Q1202 + 281	PG, GQ Com	RQ	0.165	15.51	1.26	VAR	✓
Q1211 + 143	PG	RQ	0.085	14.63	1.39	UVX	✓
Q1219 + 755	Mkn 205	RQ	0.070	15.24	1.21	UVX	✓
Q1307 + 085	PG	RQ	0.155	15.28	1.42	UVX	✓
Q1352 + 183	1E, PG	RQ	0.152	15.5	1.46	UVX	✓
Q1416 – 129	PG	RQ	0.129	15.40	1.26	UVX	✓
Q1426 + 015	Mkn 1383	RQ	0.086	15.05	1.41	UVX	✓
Q1545 + 210	3CR 323.1, 4C 21.45 PKS, PG	RL	0.264 ^f	16.69 ^f	1.37	RAD	✓
Q1613 + 658	Mkn 876, PG	RQ	0.129	15.37	1.36	UVX	✓
Q1635 + 119		RL	0.146	16.50	1.31	RAD	X
Q1721 + 343	4C 34.47	RL	0.206	16.50	1.28	RAD	✓
Q1803 + 676	<i>in</i> Kazaryan 102	RQ	0.136 ^f	15.78 ^f	1.45	UVX	✓
Q2130 + 099	PG <i>in</i> II Zw 136	RQ	0.061	14.62	1.52	UVX	✓
Q2135 – 147	PHL 1657, PKS	RL	0.200 ^f	15.19 ^f	1.25	UVX	✓
Q2251 – 178	MR	RQ	0.068	14.36	1.28	XRAY	✓

^aClassification: RL = Radio Loud; RQ = Radio quiet; from Table 1 of Elvis et al. (1994a).

^b Redshifts, and V magnitudes, from Table 1 of Elvis et al. (1994a), unless otherwise noted.

^c $\alpha_{ox} \equiv -\log(l_{opt}/l_x)/\log(\nu_{opt}/\nu_x)$ where l_{opt} and l_x are the 2500Å and 2 keV fluxes measured in the rest-frame; from Table 2 of Elvis et al. (1994a).

^d Primary selection technique based on: radio (RAD), color excess (UVX), X-ray (XRAY) or variability (VAR) measurements. For the $z \geq 0.1$ quasars these designations are from Table 1 of Hewitt & Burbidge (1993) and for the $z < 0.1$ ones not included in that version, from Table 1 of Hewitt & Burbidge (1991). Three quasars not in either version: Q0844+349, Q1211+143 and Q1426+015; appear in the Markarian or PG surveys so we list these as UVX selected.

^e ‘✓’s indicate the quasars used in the final analysis and ‘X’’s indicate those omitted.

^f redshift and magnitude from Hewitt & Burbidge (1993).

Table 3. VLA Fluxes: $z > 3$ Quasars

Quasar	$\nu = 4.95$ GHz			$\nu = 1415$ MHz		
	F_{max} [mJy] ^a	RMS flux [mJy] ^b	SNR	F_{max} [mJy] ^a	RMS flux [mJy] ^b	SNR
Q0000 – 263	0.27	0.13	2.1	0.32	0.16	2.0
Q0055 – 269	0.45	0.14	3.2	0.44	0.20	2.2
Q0114 – 089	0.23	0.13	1.8	0.12	0.16	0.8
Q1107 + 48	0.48	0.14	3.4	0.33	0.37	0.9
Q1159 + 123	0.31	0.14	2.2	0.44	0.17	2.6
Q1206 + 119	0.26	0.13	2.0	0.42	0.17	2.5
Q1208 + 101	0.20	0.12	1.7	0.31	0.15	2.1
Q1358 + 391	0.24	0.12	2.0	0.13	0.17	0.8
Q1946 + 7658	0.89	0.13	6.8	0.43	0.17	2.5

^a F_{max} is the flux measured at position of beam peak if no obvious source was visible.

^bRMS flux measured far from center of image

Table 4. Instrument/Observation Summary

Telescope/Run Dates	Instrument ^a	Detector	$\lambda\lambda$	W/D ^b	gpm ^c	R ^d	t_{total}^e
IR SPECTROSCOPY							
MMT Nov 93	Fspec	NICMOS HgCdTe 256 × 256	H K	1.2''	75 75	730 670	50 40-90
KPNO 4-m Dec 93	CRSP	SBRC 41 InSb 256 × 256	J J K K	1.4''	150 300 150 300	550 1430 700 1800	30-140 20 50-80 25-50
CTIO 4-m Sep 94, Dec 93	OSIRIS	NICMOS3 HgCdTe 256 × 256	IJHK ^f	1.2''	120	550	50-200
IR PHOTOMETRY							
MMT Jun, Sep, Oct 93, Mar 94	IR-phot	InSb single-channel	J, H, K & L'	5''3 or 8''7	30-40
MMT Nov 92	IR-bolom	Ge diode	N	5''4	13-27
CTIO 4-m Sep 94, Dec 93	OSIRIS	NICMOS3 HgCdTe	H K	32 pxls (12''.7) 0''.398/pxl	4.5 2.5
OPTICAL SPECTROPHOTOMETRY							
MMT May 91 & Sep 91	Red channel	TI 5 CCD 800 × 800	4200-8400 4200-8400 4000-6550	5'' 1''.5 1''.5	150 150 300	60 250 450	5-20
FLWO 1.5-m Feb 94	FAST	Loral CCD unthinned 512 × 2688	3700 – 7500	5''	300	500	45
Steward Obs. 2.3-m Sep 92	B&C spec	Loral CCD 1200 × 800	5500-9100 3200-6500	4''.5 4''.5	400 300	160 180	60
May 90 CTIO 1.5-m Sep 93	RC spec	thick GEC CCD 576 × 420	4500-7500 3500-8300 5000-9500	4''.5 4'' 4''	300 150 (#13) 158 (#11)	400 300 480	60
OPTICAL PHOTOMETRY							
FLWO 1.2-m Oct 93 & Apr 94	Ford CCD 2048 × 2048	UBVRI	24,28 pxls (14''.4, 16''.8) 0''.6/pxl ^g	2-10
CTIO 0.9-m Sep 93	Tek CCD 1024 × 1024	BRI	24 pxls (11''.9) 0''.496/pxl	2-4

^aInstrument references: Fspec — Williams et al. (1993); CRSP — Joyce, Fowler and Heim (1994); OSIRIS — DePoy et al. (1993); IR-photometer — Rieke (1984); IR-bolometer — Keller, Sabol and Rieke (1990); FAST spectrograph — Fabricant et al. (1998)

^bAperture: In the case of spectroscopic observations, the projected slit width on the sky in arcseconds. All spectroscopy was done using long slits which included object and sky. In the case of photometric observations, the diameter of the aperture through which the object was observed (MMT IR photometer and bolometer) or that chosen in the data reduction (OSIRIS).

^cgratings per mm of the grating used.

^dR = $\lambda/\Delta\lambda$, where $\Delta\lambda$ is the FWHM which corresponds to the 2-pixel dispersion for the IR spectra.

^eThe range of total on-source integration times (min) per object per filter or setting.

^fCross-dispersed, spectral range $\sim 1.1\mu\text{m}$ to $2.4\mu\text{m}$ (IJHK)

^gThe pixels were binned 2×2 , and the plate scale given here is for the 2×2 binning.

Table 5. Log of IR spectroscopic observations

Quasar	Instrument	bands	slit \times grating ^a	R ^b	t ^c	date (UT)	comments
Q0000 - 263	OSIRIS	JHK	1.2x120	550	80	1994 Jul 27	
Q0014 + 813	CRSP	J	1.4x150	550	27	1993 Dec 6	
	CRSP	J	1.4x300	1430	20	1993 Dec 7	
	Fspec	K	1.2x75	670	88	1993 Nov 26	
Q0055 - 269	CRSP	K	1.4x150	1450	50	1993 Dec 6	0.8 seeing
	CRSP	J	1.4x150	550	93	1993 Dec 7	variable seeing, cirrus
	OSIRIS	JHK	1.2x120	550	102	1993 Dec 5	
Q0114 - 089	CRSP	J	1.4x150	550	53	1993 Dec 4	1.4 seeing
	Fspec	K	1.2x75	670	56	1993 Nov 28	thin cirrus
Q0347 - 383	OSIRIS	JHK	1.2x120	550	198	1993 Dec 8	
Q0420 - 388A	OSIRIS	JHK	1.2x120	550	48	1994 Sep 26	
Q0636 + 680	CRSP	J	1.4x150	550	80	1993 Dec 4	$\gtrsim 1''$ seeing
	CRSP	K	1.4x150	670	47	1993 Dec 5	cirrus
	CRSP	K	1.4x300	1720	53	1993 Dec 6	
	Fspec	K	1.2x75	670	88	1993 Nov 27	
	Fspec	H	1.2x75	730	48	1993 Nov 29	1.8 seeing; clouds
Q0956 + 122	CRSP	J	1.4x150	550	137	1993 Dec 4	1.1 seeing
	CRSP	K	1.4x300	1930	26	1993 Dec 6	
	Fspec	K	1.2x75	670	88	1993 Nov 27	thin clouds
Q1159 + 123	CRSP	J	1.4x150	550	53	1993 Dec 5	1'' seeing; some cirrus
	Fspec	K	1.2x75	670	72	1993 Nov 29	
Q1208 + 101	CRSP	K	1.4x150	700	80	1993 Dec 6	
Q1935 - 692	OSIRIS	JHK	1.2x120	550	80	1994 Sep 25	
Q1946 + 7658	CRSP	J	1.4x150	550	57	1993 Dec 6	0.8 seeing
	Fspec	K	1.2x75	670	64	1993 Nov 26	$\sim 2''$ seeing
Q2000 - 330	OSIRIS	JHK	1.2x120	550	104	1994 Sep 22	
Q2126 - 158	CRSP	J	1.4x150	550	53	1993 Dec 5	1.4 seeing
	Fspec	K	1.2x75	670	40	1993 Nov 26	$\sim 2''$ seeing
	OSIRIS	JHK	1.2x120	550	128	1994 Sep 24	
Q2204 - 408	OSIRIS	JHK	1.2x120	550	64	1994 Sep 22	

^aThe slit width (in arcsec on the sky) \times grating (gpm).^b $R = \lambda/\Delta\lambda$, where $\Delta\lambda$ is the FWHM and corresponds to the 2-pixel dispersion.^cTotal exposure time in minutes.

Table 6. IR Photometry

Quasar	Instrument	date (UT)	J	H	K	L ^a	N ^a	comments ^b
Q0000-263	OSIRIS	1993 Dec 5	15.07 ± 0.05	
	MMT-IRphot	1993 Oct 30	16.09 ± 0.05	15.48 ± 0.05	14.85 ± 0.05	c
Q0014+813	MMT-IRphot	1993 Jun 4	13.60 ± 0.02	> 13.18	...	5''3
	MMT-IRphot	1993 Jun 8	14.88 ± 0.01	14.21 ± 0.17	13.61 ± 0.02	12.28 ± 0.52	...	5''3
	MMT-IRbol	1992 Nov 8	> 8.81	5''4
Q0055-269	OSIRIS	1993 Dec 5	15.48 ± 0.06	
	OSIRIS	1994 Sep 26	...	15.92 ± 0.09	
	MMT-IRphot	1993 Sep 27	...	16.06 ± 0.06	15.12 ± 0.07	> 12.89	...	8''7, d
Q0114-089	MMT-IRphot	1993 Sep 27	15.11 ± 0.10	> 13.40	...	8''7, d
	OSIRIS	1994 Sep 26	...	15.95 ± 0.09	
	MMT-IRbol	1992 Nov 8	> 8.39	5''4
Q0347-383	OSIRIS	1994 Sep 26	...	16.04 ± 0.09	
Q0420-388	OSIRIS	1994 Sep 26	...	14.86 ± 0.08	
Q0636+680	MMT-IRphot	1993 Oct 30	14.83 ± 0.05	14.31 ± 0.05	13.68 ± 0.05	c
	MMT-IRphot	1994 March 24	12.64 ± 0.24	...	5''3, e
Q0956+122	MMT-IRphot	1993 Oct 30	16.10 ± 0.05	15.59 ± 0.05	15.11 ± 0.05	c
Q1107+48	MMT-IRphot	1993 Jun 8	14.33 ± 0.07	12.91 ± 0.59	...	5''3
Q1159+123	MMT-IRphot	1993 Jun 8	16.03 ± 0.04	15.50 ± 0.17	14.71 ± 0.07	> 12.61	...	5''3
Q1208+101	MMT-IRphot	1993 Jun 7	16.24 ± 0.06	...	15.42 ± 0.12	5''3
Q1358+391	MMT-IRphot	1993 Jun 7	16.48 ± 0.08	15.98 ± 0.08	15.32 ± 0.10	> 12.63	...	5''3
Q1442+101	MMT-IRphot	1993 Jun 8	16.83 ± 0.06	16.42 ± 0.17	15.94 ± 0.11	> 10.99	...	5''3
Q1935-692	OSIRIS	1994 Sep 26	...	16.27 ± 0.11	
Q1946+7658	MMT-IRphot	1993 Jun 4	14.58 ± 0.01	14.01 ± 0.02	13.44 ± 0.02	12.50 ± 0.16	...	5''3
	MMT-IRbol	1992 Nov 8	> 8.59	5''4
Q2000-330	OSIRIS	1994 Sep 26	...	15.64 ± 0.09	
Q2126-158	OSIRIS	1994 Sep 26	...	14.82 ± 0.08	
	MMT-IRphot	1993 Jun 7	15.57 ± 0.04	14.99 ± 0.08	14.28 ± 0.09	13.11 ± 0.50	...	5''3
	MMT-IRbol	1992 Nov 8	> 7.54	5''4
Q2204-408	OSIRIS	1994 Sep 26	...	15.47 ± 0.09	

^aLower limits to the magnitudes were determined from the 3σ flux upper limits following: $M_{3\sigma} = -2.5\log_{10}[3\sigma(F)/F_0]$ where $F_0 = 309$ Jy at L' (Cutri 1994, private communication) and $F_0 = 36$ Jy at N (Rieke, Lebofsky and Low 1985)

^bComments include aperture used (") for MMT IR photometer or bolometer observations and the additional notes: c. Photometry obtained and reduced by R. Cutri; d. Photometry obtained and reduced by S. Kenyon; e. A 10", rather than 15", throw used.

Table 7. Log of Optical Spectrophotometric Observations

Quasar	Telescope	λ (Å)	slit/grating ^a	R ^b	t ^c	date (UT)
Q0000 – 263	CTIO 1.5-m	5090-9580	4/158	500	60	1993 Sep 16
	MMT	3685-8780	5/150	60	15	1991 Sep 16
	MMT	3685-8780	1.5/150	250	20	1991 Sep 16
Q0014 + 813	MMT	3685-8780	5/150	60	5	1991 Sep 16
	MMT	3685-8780	1.5/150	250	10	1991 Sep 16
Q0055 – 269	CTIO 1.5-m	3500-8300	4/150	400	60	1993 Sep 15
	CTIO 1.5-m	5000-9500	4/158	500	60	1993 Sep 16
Q0114 – 089	CTIO 1.5-m	5000-9500	4/158	500	60	1993 Sep 17
Q0347 – 383	CTIO 1.5-m	3500-8300	4/150	400	60	1993 Sep 15
	CTIO 1.5-m	5000-9500	4/158	500	60	1993 Sep 17
Q0420 – 388A	CTIO 1.5-m	3500-8300	4/150	400	60	1993 Sep 15
	CTIO 1.5-m	5000-9500	4/158	500	56.7	1993 Sep 16
	MMT	4200-8400	5/150	60	10	1991 May 17
Q0636 + 680	MMT	4200-8400	1.5/150	250	5	1991 May 17
	MMT	4060-6550	1.5/300	400	15	1991 May 19
Q0956 + 122	FLWO 1.5-m	3680-7575	5/300	500	45	1994 Feb 6
Q1159 + 123 ^d	Steward 2.3-m	4500-7500	4.5/300	400	50	1990 May 21
Q1208 + 101	MMT	4200-8400	5/150	60	10	1991 May 17
	MMT	4200-8400	1.5/150	250	15	1991 May 17
	MMT	4000-6550	1.5/300	400	10	1991 May 18
Q1935 – 692	CTIO 1.5-m	3500-8300	4/150	400	80	1993 Sep 15
	CTIO 1.5-m	5000-9500	4/158	500	60	1993 Sep 17
Q1946 + 7658	Steward 2.3-m	3200-6500	4/400	160	30	1992 Sep 23
	Steward 2.3-m	5500-9100	4/300	180	30	1992 Sep 23
Q2000 – 330	CTIO 1.5-m	3500-8300	4/150	400	60	1993 Sep 15
	CTIO 1.5-m	5000-9500	4/158	500	60	1993 Sep 16
Q2126 – 158	CTIO 1.5-m	5000-9500	4/158	500	60	1993 Sep 16
	MMT	4200-8400	1.5/150	250	15	1991 Sep 16
	MMT	4200-8400	5/150	60	10	1991 Sep 16
Q2204 – 408	CTIO 1.5-m	3500-8300	4/150	400	60	1993 Sep 14
		5000-9500	4/158	500	60	1993 Sep 17

^aThe slit width (in arcsec on the sky) and grating (gpm).

^b $R = \lambda/\Delta\lambda$, where $\Delta\lambda$ is the FWHM.

^cThe total exposure time in minutes.

^dfrom Bechtold et al. 1994.

Table 8. Optical Photometric Observations

Quasar	telescope	date (UT)	U	B	V	R	I
Q0000-263	CTIO 0.9-m	93 Sep 12	17.33 ± 0.03	16.89 ± 0.03
	CTIO 0.9-m	93 Sep 12	17.34 ± 0.03	...
	CTIO 0.9-m	93 Sep 13	...	20.21 ± 0.03
Q0014+813	FLWO 1.2-m	93 Oct 27	...	17.56 ± 0.04	...	16.14 ± 0.02	15.66 ± 0.02
	FLWO 1.2-m	93 Oct 27	...	17.56 ± 0.07
	FLWO 1.2-m	93 Oct 27	...	17.53 ± 0.04
Q0055-269	CTIO 0.9-m	93 Sep 12	17.57 ± 0.03	17.46 ± 0.03
	CTIO 0.9-m	93 Sep 13	...	18.68 ± 0.03
Q0114-089	CTIO 0.9-m	93 Sep 12	17.21 ± 0.03	16.93 ± 0.03
	CTIO 0.9-m	93 Sep 13	...	18.12 ± 0.03
Q0130-403	CTIO 0.9-m	93 Sep 12	16.86 ± 0.03	16.56 ± 0.03
	CTIO 0.9-m	93 Sep 13	...	17.69 ± 0.03
Q0347-383	CTIO 0.9-m	93 Sep 12	17.56 ± 0.03	17.23 ± 0.03
	CTIO 0.9-m	93 Sep 13	...	18.63 ± 0.03
Q0351-390	CTIO 0.9-m	93 Sep 12	17.05 ± 0.03	16.84 ± 0.03
	CTIO 0.9-m	93 Sep 13	...	17.85 ± 0.03
Q0420-388A	CTIO 0.9-m	93 Sep 12	16.64 ± 0.03	16.28 ± 0.03
	CTIO 0.9-m	93 Sep 13	...	17.80 ± 0.03
Q0636+680	FLWO 1.2-m	93 Oct 26	...	17.35 ± 0.01	...	16.25 ± 0.01	15.77 ± 0.02
	FLWO 1.2-m	93 Oct 27	16.34 ± 0.01	15.90 ± 0.02
Q0956+122	FLWO 1.2-m	93 Oct 26	...	18.22 ± 0.04	...	17.09 ± 0.02	16.88 ± 0.03
	FLWO 1.2-m	93 Oct 27	17.17 ± 0.04	16.82 ± 0.05
Q1107+48	FLWO 1.2-m	94 Apr 2	17.37 ± 0.05	17.24 ± 0.03	16.92 ± 0.02	16.63 ± 0.03	16.24 ± 0.04
Q1159+123	FLWO 1.2-m	94 Apr 2	...	18.79 ± 0.06	17.30 ± 0.02	17.33 ± 0.04	16.91 ± 0.06
Q1208+101	FLWO 1.2-m	94 Apr 3	...	18.79 ± 0.11	17.71 ± 0.04	16.96 ± 0.07	16.63 ± 0.08
Q1358+391	FLWO 1.2-m	94 Apr 2	...	19.06 ± 0.12	17.79 ± 0.04	17.74 ± 0.07	17.31 ± 0.10
Q1935-692	CTIO 0.9-m	93 Sep 13	...	18.43 ± 0.03	...	17.35 ± 0.03	16.96 ± 0.03
Q1946+7658	FLWO 1.2-m	93 Oct 26,7	17.32 ± 0.12	16.94 ± 0.03	16.20 ± 0.02	15.89 ± 0.01	15.37 ± 0.01
		93 Oct 26,7	16.20 ± 0.02	15.87 ± 0.02	15.36 ± 0.02
		93 Oct 26,7	16.19 ± 0.02
		93 Oct 26,7	16.21 ± 0.02
Q2000-330	CTIO 0.9-m	93 Sep 13	...	18.95 ± 0.03	...	17.07 ± 0.02	16.77 ± 0.03
Q2126-158	CTIO 0.9-m	93 Sep 13	...	18.08 ± 0.03	...	16.74 ± 0.02	16.27 ± 0.03
Q2204-408	CTIO 0.9-m	93 Sep 13	...	18.52 ± 0.03	...	17.43 ± 0.02	16.97 ± 0.03

Note. — As mentioned in the text, the CTIO observations were made in photometric conditions. During the runs at FLWO, however, we did not have strictly photometric weather, so some observations were repeated.

Table 9. Adopted calibration data for IR and optical photometry

Filter	λ_0 [μm]	λ_- [μm]	λ_+ [μm]	$F_\nu(\lambda_0; \text{Vega})$ [Jy]	$F_\nu(\lambda_0; \text{PL})$ [Jy] ^a	Δm ^b
U	0.365	0.337	0.392	1353	1759	-0.28
B	0.434	0.384	0.484	4390 ^c	4970	-0.13
V	0.542	0.495	0.589	3630	3610	0.006
R	0.628	0.566	0.690	3080	3040	0.014
I	0.836	0.725	0.948	2265	2265	0.0
J ^d	1.25	1.15	1.35	1603
H ^d	1.60	1.40	1.80	1075
K ^d	2.22	1.97	2.47	667
L' ^d	3.4	3.3	3.5	309
N ^d	10.6	8.2	13.21	36

^a $F_\nu(\lambda_0; PL)$ is the flux within a band that would be expected for a power law as opposed to a stellar spectrum. We compute it by scaling the zero magnitude Vega flux by the ratio of the normalized convolution of a power law spectrum ($F_\nu(PL)$) with the filter (ϕ_f) and detector (ϕ_d) response functions to the likewise convolved Vega spectrum ($F_\nu(\text{Vega})$; from Hayes 1985). ($F_\nu(\lambda_0; PL) = F_\nu(\lambda_0; \text{Vega}) \times [\int F_\nu(\text{Vega}) \phi_f \phi_d d\nu / F_\nu(\lambda_0; \text{Vega})] \times [F_\nu(\lambda_0; PL) / \int F_\nu(PL) \phi_f \phi_d d\nu]$.) We computed $F_\nu(\lambda_0; PL)$ assuming both $\alpha = -0.3$ (Francis et al. 1993) and $\alpha = -1.0$ (Elvis et al. 1994), and this column gives the average of these results, which did not differ by much. These fluxes, rather than those of Vega, were used to flux calibrate the optical photometry (§4.4) but not the IR (§4.2).

^bSynthetic color correction for spectra of a power law form:

$$\Delta m = -2.5 \log(F_{\nu, PL} / F_{\nu, \text{Vega}}).$$

^cVega spectrum extrapolated over H γ absorption.

^dCentral wavelengths and bandpasses for the near-IR bands from: G. Rieke and M. Rieke, private communication. References for zero-magnitude fluxes: Campins, Rieke & Lebofsky 1985 (J, H and K), Cutri 1994 (private communication, L'), and Rieke, Lebofsky & Low 1985 (N).

Table 10. Scaling factors applied to spectra

Quasar/ $\lambda\lambda$	source of spectrum	λ range	g	$\frac{\sigma(F_p)}{F_p}$ a	$\frac{\sigma\langle A \rangle}{\langle A \rangle}$
Q0000 – 263					
optical	MMT Red	4000-8800	1.1791 ^g	0.023	0.036
	CTIO	5100-9600	1.0494 ^g	0.023	0.043
J	OSIRIS	1.20-1.33, 1.23-1.35	1.7425 ^d	0.046	0.015
H	OSIRIS	1.41-1.46, 1.48-1.83	1.7425 ^d	0.046	0.015
K	OSIRIS	1.94-2.33	1.7425 ^d	0.046	0.015
Q0014 + 813					
optical	MMT Red	3700-8800	1.0585 ^h	0.014	0.010
J	CRSP g3	1.09-1.36	0.6439 ^b	0.011	0.005
J	CRSP g1	1.17-1.28	0.2541 ^b	0.011	0.005
K	Fspec	1.97-2.40	1.5909 ^d	0.0178	0.006
Q0055 – 269					
optical	CTIO	3600-9600	1.1133 ^g	0.023	0.033
J	CRSP g3	1.11-1.35	0.6306 ⁱ	0.054	0.012
J	OSIRIS	1.20-1.24, 1.23-1.35	1.6415 ^f	0.054	0.019
H	OSIRIS	1.42-1.49, 1.49-1.82	1.6415 ^f	0.054	0.019
K	OSIRIS	1.98-2.41	1.6415 ^f	0.054	0.019
Q0114 – 089					
optical	CTIO	5100-9600	1.0424 ^g	0.023	0.007
K	Fspec	1.98-2.39	2.2642 ^d	0.092	0.022
Q0347 – 383					
optical	CTIO	3500-9600	1.0792 ^g	0.023	0.013
J	OSIRIS	1.20-1.24, 1.23-1.35	1.3156 ^e	0.081	0.013
H	OSIRIS	1.41-1.49, 1.49-1.82	1.3156 ^e	0.081	0.013
K	OSIRIS	1.98-2.37	1.3156 ^e	0.081	0.013
Q0420 – 388					
optical	CTIO	3500-9600	1.0617 ^g	0.028	0.007
J	OSIRIS	1.19-1.22, 1.22-1.35	1.2281 ^e	0.076	0.008
H	OSIRIS	1.40-1.47, 1.47-1.81	1.2281 ^e	0.076	0.008
K	OSIRIS	1.96-2.35	1.2281 ^e	0.076	0.008
Q0636 + 680					
optical	MMT Red	4200-8400	1.0820 ^h	0.009	0.005
J	CRSP g3	1.11-1.34	0.7541 ^b	0.046	0.004
H	Fspec	1.50-1.78	3.4163 ^c	0.046	0.008
K	CRSP g1	1.96-2.10	0.9610 ^d	0.046	0.007
K	CRSP g3	1.93-2.33	0.7910 ^d	0.046	0.006
K	Fspec	1.96-2.40	1.2347 ^d	0.046	0.007
Q0956 + 122					
optical	FLWO 1.5-m FAST	3700-7600	1.0328 ^h	0.029	0.006
J	CRSP g3	1.10-1.36	0.9896 ^b	0.046	0.007
K	Fspec	1.97-2.39	1.5811 ^d	0.046	0.012
K	CRSP	2.08-2.22	2.4652 ^d	0.046	0.017
Q1159 + 123					
optical	S.O. 2.3-m	4600-7600	1.3428 ^h	0.036	0.007
J	CRSP g3	1.10-1.36	0.7565 ^b	0.036	0.012
K	Fspec	1.97-2.39	2.0722 ^d	0.065	0.017
Q1208 + 101					
optical	MMT Red	4200-8400	1.6688 ^h	0.061	0.018
	MMT Red	4000-6600	1.6140 ^h	0.061	0.019
K	CRSP g3	2.01-2.42	0.4273 ^d	0.107	0.009

Table 10—Continued

Quasar/λλ	source of spectrum	λ range	g	$\frac{\sigma(F_p)}{F_p}$ ^a	$\frac{\sigma <A>}{<A>}$
Q1935 – 692					
optical	CTIO	3500-9600	1.1328 ^g	0.028	0.007
J	OSIRIS	1.20-1.22, 1.22-1.35	0.382 ^e	0.104	0.016
H	OSIRIS	1.42-1.47, 1.47-1.81	0.382 ^e	0.104	0.016
K	OSIRIS	1.96-2.35	0.382 ^e	0.104	0.016
Q1946 + 7658					
optical	MMT Blue+ S.O.90''	3700-9200	0.9252 ^h	0.013	0.005
J	CRSP (night 3)	1.10-1.34	0.3915 ^b	0.0094	0.004
K	Fspec	1.96-2.40	1.4259 ^d	0.017	0.007
Q2000 – 330					
optical	CTIO	3500-9600	1.0317 ^g	0.014	0.029
J	OSIRIS	1.20-1.22, 1.22-1.35	0.9885 ^e	0.082	0.010
H	OSIRIS	1.41-1.47, 1.47-1.79	0.9885 ^e	0.082	0.010
K	OSIRIS	1.98-2.35	0.9885 ^e	0.082	0.010
Q2126 – 158					
optical	MMT Red	4200-8800	1.0070 ^g	0.014	0.015
	CTIO	5100-9600	1.0108 ^g	0.014	0.013
J	CRSP g3	1.10-1.35	0.8913 ^b	0.039	0.007
J	OSIRIS	1.20-1.22, 1.22-1.35	0.5477 ^d	0.078	0.014
H	OSIRIS	1.41-1.47, 1.47-1.81	0.5477 ^d	0.078	0.014
K	OSIRIS	1.96-2.35	0.5477 ^d	0.078	0.014
	Fspec	1.96-2.40	2.0551 ^d	0.078	0.013
Q2204 – 408					
optical	CTIO	3500-9600	1.1321 ^g	0.014	0.015
J	OSIRIS	1.19-1.22, 1.22-1.35	1.6640 ^e	0.081	0.022
H	OSIRIS	1.43-1.47, 1.48-1.80	1.6640 ^e	0.081	0.022
K	OSIRIS	1.96-2.35	1.6640 ^e	0.081	0.022

^a $\sigma(F_p)/F_p$ is equal to $0.4 \ln(10) \sigma(m)$ where the values $\sigma(m)$ are given in the logs of optical and IR photometry

^bNormalized to match MMT J band photometry

^cNormalized to match MMT H band photometry

^dNormalized to match MMT K band photometry

^eNormalized to match OSIRIS H band photometry

^fNormalized to match OSIRIS K band photometry

^gNormalized to match CTIO R band photometry

^hNormalized to match 48''R band photometry

ⁱNormalized to match the average over the OSIRIS J band spectrum

Table 11. Galactic and Ly α column densities toward the high redshift quasars

Quasar	α (1950)	δ (1950)	z_{QSO}	$N_{HI}(\text{Gal})^a$	$z_{dLy\alpha}$	$N_{HI}(Ly\alpha)^a$
Q0000 – 263	00 00 49.5	–26 20 01	4.111	1.43 ^b	3.395 ^c	20.00 ^c
Q0014 + 813	00 14 04.50	+81 18 29 ^d	3.3866	14.30 ^b
Q0055 – 269	00 55 32.6	–26 59 25 ^d	3.6625	1.77 ^b
Q0114 – 089	01 14 53	–08 57 20 ^d	3.1626	2.44 ^e
Q0347 – 383	03 47 54.20	–38 19 34 ^d	3.222	1.98 ^e	3.0244 ^f	6.31 ^f
Q0420 – 388A	04 20 29.90	–38 51 51 ^d	3.123	1.91 ^g
Q0636 + 680	06 36 47.60	+68 01 26 ^d	3.1775	5.11 ^b
Q0956 + 122	09 56 11.10	+12 17 07 ^d	3.306	2.88 ^e
Q1159 + 123	11 59 14.20	+12 23 12 ^d	3.502	2.04 ^b
Q1208 + 101	12 08 23.8	+10 11 08 ^d	3.811	1.59 ^b
Q1935 – 692	19 35 11.60	–69 14 51 ^d	3.17	5.40 ^e
Q1946 + 7658	19 46 41.00	+76 58 26.00	3.02	7.20 ^b	2.841 ^h	1.5 ^h
Q2000 – 330	20 00 13.06	–33 00 12.30	3.7832	7.44 ^b
Q2126 – 158	21 26 26.8	–15 51 50 ^d	3.266	4.85 ^g
Q2204 – 408	22 04 33.20	–40 51 37 ^d	3.169	1.40 ^e

^aColumn densities in the Galaxy, $N_{HI}(\text{Gal})$ and the damped Ly α systems, $N_{HI}(Ly\alpha)$, are in units of 10^{20} cm^{-2} .

^bfrom Table 1(e) of Murphy et al. 1996. $\tau \ll 1$ is assumed (and so the peak observed brightness temperature, $T_{peak} = T_{spin}$). The differences between the column densities they determine for $\tau \ll 1$ and for $T_{spin} = 150\text{K}$ are less 5% for the above quasars. Accurate to $< 10^{19} \text{ cm}^{-2}$

^c $N_{HI}(Ly\alpha)$ and z_{abs} from Lanzetta et al. (1991).

^dpositions from Schneider et al. 1992

^e N_{HI} from Stark et al. (1992)

^ffrom Williger et al. (1989).

^gfrom Table 1 of Elvis, Lockman & Wilkes (1989). All values are for $T_{spin} = 250\text{K}$ and are accurate to $< 10^{19} \text{ cm}^{-2}$

^hThe redshift and column density of the damped Ly α system in the foreground of HS1946+7658 are from Hagen et al. (1992; redshift) and Dobrzycki & Bechtold (1996; redshift and column density).

Table 12. Parameters used in correcting for ‘Ly α forest’ absorption

Quasar	ref ^a high R	source of ^b spectrophot	smooth ^c	shift ^d	λ^e range	fit ^f order	valid fit ^g range (Å)
Q0000-263	3	1	2	7	5850-6250	3	5850-6250
Q0000-263	3	2	1	16	5850-6250	3	5850-6250
Q0014+813	1	1	3	22	4580-5425	5	4600-5400
Q0420-388(1)	5	2	1	13	3770-3910	4 (fit to 1 only)	3775-
Q0420-388(2)	5		1	13	3965-4140	8 (fit to 1-6)	
Q0420-388(3)	5		1	13	4195-4390	8 (fit to 1-6)	
Q0420-388(4)	5		1	22	4435-4640	8 (fit to 1-6)	
Q0420-388(5)	5		1	24	4695-4920	3 (fit to 5 only)	
Q0420-388(6)	5		1	22	4960-5210	2 (fit to 6 only)	5200
Q0636+680	1	1	3	44	4225-5125	9	4250-5150
Q0636+680	3	1	3	33	4935-5100	2	4940-5100
Q1208+101	4	1	1	0	5490-6090	3	5475-6100
Q1208+101	4	4	1	5	5490-6090	3	5475-6100
Q1946+7658(1)	2	3	2	13	3550-4100	5 (fit to 1 only)	3600-4100
Q1946+7658(2)	2	3	2	9	4100-5000	5 (fit to 2 only)	4100-5000
Q2126-158(4)	5	1	3	26	4300-4500	5 (fit to 4-8)	4320-
Q2126-158(5)	5		3	26	4550-4750	5 (fit to 4-8)	
Q2126-158(6)	5		3	11	4810-5030	5 (fit to 4-8)	
Q2126-158(7)	5		2	11	5100-5320	5 (fit to 4-8)	
Q2126-158(8)	5		2	11	5380-5640	5 (fit to 4-8)	5620

^aThe telescope/instrument configurations and references for the high resolution spectra: (1) MMT Big Blue Reticon, $R \approx 65 \text{ km s}^{-1}$ - Bechtold 1994; (2) MMT Big Blue Reticon, $R \approx 50 \text{ km s}^{-1}$ - Dobrzycki & Bechtold 1996; (3) Palomar 200-in $R \approx 75 \text{ km s}^{-1}$, Bechtold 1994; (4) Palomar 200-in $R \approx 100 \text{ km s}^{-1}$, Bechtold 1994; (5) Las Campanas Observatory (LCO) $R \approx 19 \text{ km s}^{-1}$. The high resolution spectra of Q0420-388, Q1946+7658 and Q2126-158 were obtained at different settings to extend the wavelength coverage. These segments (numbered for identification in column 7) were considered individually until the fitting procedure, in which a fit was tried to all segments at once and to each individually, and the resulting polynomial fit to the ‘correction function’ was chosen - by eye - to be either the single or spliced polynomial, as indicated in column 7.

^bThe telescope/grating combination with which the spectrophotometric data that were corrected were obtained: (1) MMT, 150 gpm; (2) CTIO 1.5-m, 150 gpm; (3) Steward Observatory 2.3-m 300 gpm; (4) MMT, 300 gpm.

^cThe number of pixels, N, to either side of the central pixel whose value is replaced by the average in the smoothing procedure with a box car of width $2N+1$.

^dThe number of pixels by which the spectrophotometry needed to be shifted to match the wavelength calibration of the high resolution data. Positive is increasing wavelength.

^eSpectral range of high resolution spectrum = range over which the polynomial fit to the ratio of spectra was made.

^fOrder of best-fitting polynomial

^gSpectral range over which the correction is valid. At the edges of each spectrum, the smoothing procedure included 0’s when there were no data. This resulted in steep artificial gradients which do not correspond with the shape of the actual data. Hence, by eye, we chose the range over which the data appear uncorrupted.

Table 13. Construction of quasi-simultaneous and simultaneous low z SEDs

Object(yr)	IUE obs	IUE date	optical spec ^a	optical phot ^a	Comments ^b	used? ^c
Q0007+106	SWP01806	78 Jun 18	1980 Nov 15	1986 Sep 28	N	✓
	LWR01687	78 Jun 18				
	SWP23248	84 Jun 12				
	LWP03560	84 Jun 12				
Q0026+129	SWP10953	81 Jan 4	1980 Nov 14	1981 Feb 5	S	✓
	LWR09629	81 Jan 4				
Q0050+124	SWP18557	82 Nov 15	1986	1986 Sep 28	N	✓
	LWR14626	82 Nov 14				
	SWP05497	79 Jun 12				
	LWR04765	79 Jun 12				
	SWP05427	79 Jun 2				
	LWR04673	79 Jun 2				
Q0052+251	SWP19224	83 Feb 8	1980 Nov 15	...	N	✓
	LWR15214	83 Feb 8				
Q0054+144	SWP30040	87 Jan 7	...	1978	N	X
	LWP11207	87 Jul 14				
Q0121-590(79)	SWP01804	78 Jun 18	...	1979 Oct 24-29	Q	✓
	LWR01685	78 Jun 18				
Q0121-590(82)	SWP17521	82 Jul 30	...	1983 Oct 11,12	Q but big break between opt & UV	X
	LWR13801	82 Jul 30				
Q0134+329	SWP34804	88 Nov 25	1978 Feb	1985 Sep 16	N, a lot of scatter at the short- λ end of the LWP spectrum	✓ ^d
	LWP14528	88 Nov 25				
Q0205+024	SWP18772	82 Dec 10	1978 Feb	1978	N	✓
	LWR14813	82 Dec 10		1986 Sep 25		
Q0312-770	SWP14485	81 Jul 16	...	1977	N,R	X
	SWP16423	82 Feb 25				
	SWP16816	82 Apr 23				
	LWP09887	87 Jan 8				
Q0804+761(82)	SWP17393	82 Jul 10	1980 Nov 15	...	N	✓
	LWR13645	82 Jul 10				
Q0804+761(86)	SWP27639	86 Jan 31	...	1986 Feb 3	S, but poor snr UV	X
	SWP27640	86 Jan 31				
	LWP07604	86 Jan 31				
Q0837-120	SWP04292	79 Feb 18	1978	1977	Q	✓
	LWR04214	79 Apr 8				
Q0844+349	SWP32433	87 Nov 30	1988 Sep 4	1986 Sep 26	Q	✓
	LWP12206	87 Nov 30				
	SWP32434	87 Nov 30				
	LWP12207	87 Nov 30				
Q1028+313	SWP28214	86 Apr 22	1988 Sep 4	1985 May 13	N	✓
	LWP12386	87 Dec 27				
Q1100+772	SWP01903	78 Jul 2	1980 Jun 5	...	N	✓
	LWR01776	78 Jul 4	1974 Jun			
Q1116+215	SWP17416	82 Jul 13	1980 Jun 5	1986 May 13	N	✓
	LWR13669	82 Jul 13	1988 Sep 4			
Q1146-037	LWR12158	81 Dec 17	...	1977	N,R	X
	LWR11083	81 Jul 17		1986		
	LWR11098	81 Jul 19				
	SWP32758	88 Jan 20				
Q1202+281	SWP19049	83 Jan 20	1980 Nov 15	1981 Jan 4, Feb 2	N	X
	LWR15078	83 Jan 20		1985 May 13		
	SWP24580	84 Nov 29				
	LWP04904	84 Nov 29				

Table 13—Continued

Object(yr)	IUE obs	IUE date	optical spec ^a	optical phot ^a	Comments ^b	used? ^c
Q1202+281(85)	SWP24580 LWP04904	84 Nov 29 84 Nov 29	...	1985 May 13	S	✓
Q1211+143	SWP27210 LWP07223 SWP30302 LWP10115	85 Dec 2 85 Dec 2 87 Feb 13 87 Feb 13	1980 Jun 5 1988 Sep 4	1985 Apr 12, May 14 1987 Jan 25	N	X
Q1211+143(85)	SWP27210 LWP07223	85 Dec 2 85 Dec 2	...	1985 Apr 12, May 14	S	X
Q1211+143(87)	SWP30302 LWP10115	87 Feb 13 87 Feb 13	...	1987 Jan 25	S	✓
Q1219+755	SWP19238 LWP01799	83 Feb 12 83 Feb 14	...	1985 May 11 1986 May 13	N	✓
Q1307+085	SWP08915 LWP02826	80 May 4 84 Feb 21	1980 Jul 20 1988 Sep 4	1986 May 13	N	✓
Q1352+183	SWP20706 LWR16428 SWP20112	83 Aug 17 83 Jul 25 83 May 31	1980 Jun 5	...	N	✓
Q1416-129	SWP08916 SWP33030 LWR16072	80 May 4 88 Mar 3 83 Jun 5	1980 Jul 20 1988 Jun 10, Sep 4	1985 Apr 12, May 14	N	✓
Q1426+015	SWP25338 LWP05446	85 Feb 29 85 Mar 1	...	1985 Apr 12	S	✓
Q1545+210	SWP20764 LWR16665	83 Aug 27 83 Aug 27	...	1983 May 3	S	✓
Q1613+658	SWP21962 LWP02615	84 Jan 7 84 Jan 13	1980 Jun 4	...	N	✓
Q1635+119	SWP33232	88 Apr 9	...	1981 1985	N, R	X
Q1721+343	SWP28261 LWP08171	86 May 4 86 May 10	...	1985 May 13	Q	✓
Q1803+676	SWP31032 LWP10810	87 May 23 87 May 22	1988 Jun 11	1985 May 11	S	✓
Q2130+099(79)	SWP05389 LWR04610	79 May 29 79 May 27	1980 Jul 19	...	Q	✓
Q2130+099(85)	SWP27211 LWP07205	85 Dec 2 85 Nov 30	...	1985 May 11 1986 Sep 26	S	X
Q2135-147	SWP18741 LWP01739	82 Dec 6 82 Dec 7	...	1982 Jun 16, Jul 2	S	✓
Q2251-178	SWP07485 LWR06470	79 Dec 4 79 Dec 4	...	1979	S	✓

^aReferences to the sources of the optical spectrophotometry and photometry are given in Elvis et al. (1994)

^bNotes on the spectra: S=simultaneous (data taken within 1 year); Q=quasi-simultaneous (data taken within 2 years); N=non-simultaneous (time span greater than 2 years); R=was rejected from the sample, as noted in Table 2

^cused (✓) or not used (X) in data analysis

^dused in analysis, except when its luminosity at $\lambda_{rest} = 1460 \text{ \AA}$ is needed, e.g. 1285-1460\text{\AA} spectral index

Table 14. Narrow Bands

central wavelength	spectral range	continuum?	comments
1115Å	1100 - 1130Å	yes	close to a continuum window used by Zheng et al. 1997 (HST quasar composite)
1160Å	1150 - 1170Å	yes	just blueward of Ly α
1285Å	1275 - 1295Å	yes	between Ly α and SiIV/OIV]; from Francis et al. (1991)
1460Å	1450 - 1470Å	yes	between SiIV/OIV] and CIV
2200Å	2180 - 2220Å	yes	from Francis et al. (1991)
2500Å	2480 - 2520Å	no	FeII multiplets 1-6,33-36 and 64 (Joly 1993)
2660Å	2640 - 2680Å	yes	blueward of MgII
3023Å	3001 - 3041Å	yes	redward of MgII
4200Å	4180 - 4220Å	yes	for low z , between IUE and optical data; for high z , between optical and IR; Francis et al. (1991)
4750Å	4730 - 4770Å	yes	blueward of H β /[OIII]
5100Å	5080 - 5120Å	yes	redward of H β /[OIII];
7500Å	7480 - 7520Å	yes	long wavelength constraint

Table 15. Narrow band luminosities (High z Sample)

λ_o	$\log \nu L_\nu^{a,b}$	σ_{avg}	σ_{var}	N ^c	Q ^d	$\log \nu L_\nu$	σ_{avg}	σ_{var}	N	Q	$\log \nu L_\nu$	σ_{avg}	σ_{var}	N	Q
Q0000 – 263					Q0014 + 813					Q0055 – 269					
1285Å	47.72	0.01	0.02	29	3	48.06	0.01	0.01	13	3	47.21	0.02	0.03	11	3
1460Å	47.66	0.01	0.02	29	3	48.01	0.01	0.01	14	3	47.13	0.02	0.04	12	3
2200Å	47.55	0.11	0.18	24,33	2	47.74	0.02	0.02	21,34	1	47.13	0.06	0.09	22,30	2
2500Å	47.52	0.03	0.09	18	3	47.78	0.01	0.01	12	3	47.12	0.02	0.04	18	3
2660Å	47.49	0.10	0.10	1	3	47.74	0.00	0.01	25	3	47.13	0.02	0.08	41	3
3023Å	47.45	0.03	0.09	15	3	47.70	0.01	0.01	16	3	47.06	0.05	0.07	21,41	2
4200Å	47.34	0.03	0.06	10	3	47.63	0.01	0.01	13,1	2	46.85	0.06	0.09	13,16	1
4750Å	0,0	0	47.57	0.01	0.01	10	3	46.83	0.03	0.10	12	3
5100Å	0,0	0	47.53	0.01	0.01	10	3	46.85	0.05	0.14	10	3
7500Å	0,0	0	47.57	0.07	0.07	1,13	2	0,0	0
Q0114 – 089					Q0347 – 383					Q0420 – 388A					
1285Å	47.27	0.01	0.02	10	3	47.22	0.01	0.01	11	3	47.46	0.01	0.02	10	3
1460Å	47.23	0.01	0.02	11	3	47.14	0.01	0.02	11	3	47.45	0.01	0.01	10	3
2200Å	47.08	0.01	0.05	21	3	47.10	0.03	0.12	22	3	47.37	0.01	0.03	21	3
2500Å	47.06	0.08	0.13	1,27	2	47.06	0.10	0.16	23,27	2	47.39	0.05	0.08	28,26	2
2660Å	47.04	0.08	0.12	1,27	2	47.08	0.09	0.14	23,27	2	47.37	0.05	0.08	28,26	2
3023Å	46.99	0.07	0.10	1,27	2	46.99	0.05	0.11	14	3	47.33	0.04	0.06	14	3
4200Å	46.90	0.05	0.06	13,1	2	46.80	0.04	0.07	11	3	47.26	0.03	0.04	12	3
4750Å	46.97	0.05	0.08	4	1	46.81	0.06	0.15	8	3	47.26	0.05	0.06	2	3
5100Å	46.83	0.05	0.08	9	3	46.74	0.06	0.15	9	3	47.23	0.03	0.04	8	3
7500Å	0,0	0	0,0	0	0,0	0
Q0636 + 680					Q0956 + 122					Q1159 + 123					
1285Å	47.73	0.01	0.01	13	3	47.37	0.01	0.02	59	3	47.31	0.02	0.02	24	3
1460Å	47.67	0.00	0.01	14	3	47.28	0.01	0.02	61	3	47.27	0.02	0.03	24	3
2200Å	47.60	0.02	0.02	20,35	2	47.17	0.04	0.06	21,2	2	47.20	0.03	0.03	21,1	2
2500Å	47.59	0.02	0.02	20,35	2	47.15	0.03	0.04	21,2	2	47.20	0.02	0.02	17	3
2660Å	47.58	0.02	0.02	12	3	47.14	0.02	0.02	16	3	47.20	0.02	0.02	17	3
3023Å	47.59	0.02	0.03	16	3	47.09	0.02	0.02	17	3	47.11	0.02	0.03	8	1
4200Å	47.54	0.03	0.07	15	3	47.00	0.03	0.04	13,1	2	47.12	0.04	0.05	14,1	2
4750Å	47.45	0.01	0.03	50	3	46.92	0.02	0.04	10	3	47.10	0.03	0.06	11	3
5100Å	47.44	0.01	0.02	20	3	46.83	0.02	0.04	10	3	47.11	0.03	0.04	11	3
7500Å	47.32	0.08	0.08	1,13	2	0,0	0	0,0	0
Q1208 + 101					Q1935 – 692					Q1946 + 7658					
1285Å	47.50	0.02	0.03	46	3	47.32	0.01	0.02	11	3	47.87	0.01	0.02	29	3
1460Å	47.50	0.03	0.03	15	3	47.25	0.01	0.02	11	3	47.81	0.01	0.01	30	3
2200Å	47.35	0.03	0.04	1,39	2	47.10	0.02	0.07	22	3	47.86	0.01	0.03	58	1
2500Å	47.29	0.03	0.03	1,39	2	47.09	0.12	0.19	29,27	2	47.74	0.02	0.04	19,73	2
2660Å	47.24	0.02	0.02	16,1	2	47.06	0.10	0.16	29,27	2	47.73	0.02	0.03	19,73	2
3023Å	47.17	0.03	0.03	16,1	2	46.89	0.06	0.14	15	3	47.69	0.01	0.01	14	3
4200Å	46.91	0.05	0.05	12	3	46.62	0.05	0.08	12	3	47.61	0.01	0.01	12,1	2
4750Å	46.88	0.05	0.05	13	3	46.66	0.05	0.08	9	3	47.61	0.02	0.03	12,1	2
5100Å	0,0	0	46.59	0.05	0.08	9	3	47.53	0.01	0.02	9	3
7500Å	0,0	0	0,0	0	47.40	0.05	0.06	1,12	2

Table 15—Continued

λ_o	$\log \nu L_\nu^{a,b}$	σ_{avg}	σ_{var}	N ^c	Q ^d	$\log \nu L_\nu$	σ_{avg}	σ_{var}	N	Q	$\log \nu L_\nu$	σ_{avg}	σ_{var}	N	Q
Q2000 – 330															
1285Å	47.59	0.01	0.02	12	3	47.54	0.01	0.01	24	3	47.12	0.01	0.02	11	3
1460Å	47.53	0.01	0.02	12	3	47.51	0.01	0.01	24	3	47.11	0.01	0.01	11	3
2200Å	47.40	0.06	0.10	47,31	2	47.45	0.02	0.07	21	3	47.15	0.01	0.04	22	3
2500Å	47.40	0.04	0.07	8	3	47.39	0.03	0.04	20,27	2	47.18	0.11	0.19	27,27	2
2660Å	47.31	0.04	0.06	17	3	47.36	0.02	0.02	15	3	47.17	0.11	0.19	27,27	2
3023Å	47.33	0.05	0.13	17	3	47.34	0.02	0.05	31	3	47.20	0.06	0.18	14	3
4200Å	47.18	0.04	0.05	9	3	47.24	0.04	0.05	12	3	46.98	0.05	0.10	11	3
4750Å	47.12	0.04	0.06	10	3	47.21	0.03	0.05	19	3	47.00	0.05	0.12	9	3
5100Å	0,0	0	47.21	0.03	0.05	18	3	46.94	0.05	0.09	9	3
7500Å	0,0	0	47.18	0.18	0.19	1,13	2	0,0	0

^aValues of $\log L$ are $\log_{10} < \nu L_\nu >$ where the average is taken over the indicated spectral range. When no datapoints lie within the band, the value νL_ν is determined, as described in the text, by interpolating between the averaged fluxes, $< \nu L_\nu >$, where the averages are taken over the first 50Å longwards and shortwards of the nearest datapoint on the long and short wavelength sides of the band, respectively.

^bN is the number of datapoints within the band. When no datapoints lie within the band, the column for N contains the number of datapoints within the 50Å bands on the long and short wavelength sides (N_{long} , N_{short}).

^cWhen no datapoints lie within the band and the band lies beyond the extent of our dataset, a value for νL_ν could not be computed.

^dThe numbers in this column indicate the confidence that the computed luminosity represents the continuum level: 3 signifies that the luminosity was computed directly from points within the band and represents the continuum level well; 2 that it was interpolated but looks reasonable; 1 that it does not represent the continuum level well; and 0 that it could not be computed because of insufficient data coverage to the red.

Table 16. Narrow band luminosities (Low z Sample)

λ_o	$\log \nu L_\nu$	^a σ_{avg}	σ_{var}	N ^b	Q ^c	$\log \nu L_\nu$	σ_{avg}	σ_{var}	N	Q	$\log \nu L_\nu$	σ_{avg}	σ_{var}	N	Q		
Q0007 + 106						Q0026 + 129						Q0050 + 124					
1285Å	44.91	0.03	0.09	33	3	45.27	0.05	0.10	15	3	44.44	0.04	0.12	55	3		
1460Å	44.86	0.04	0.14	35	3	45.19	0.04	0.06	17	3	44.45	0.04	0.10	50	3		
2200Å	44.88	0.03	0.10	44	3	45.22	0.05	0.11	12	3	44.59	0.04	0.11	67	3		
2500Å	44.95	0.03	0.07	46	3	45.14	0.05	0.10	21	3	44.75	0.03	0.05	66	3		
2660Å	44.90	0.03	0.06	46	3	45.18	0.05	0.11	10	1	44.69	0.03	0.06	69	3		
3023Å	44.79	0.04	0.06	1,33	2	45.02	0.02	0.02	1,1	2	44.75	0.04	0.12	21	3		
4200Å	44.53	0.04	0.04	1,1	2	44.89	0.00	0.00	1,1	2	44.56	0.02	0.02	1	3		
4750Å	44.51	0.03	0.03	1,1	2	44.84	0.00	0.00	1	3	44.56	0.01	0.01	1	3		
5100Å	44.50	0.05	0.05	1,1	2	44.78	0.02	0.02	1,1	2	44.57	0.04	0.03	2	3		
7500Å	44.40	0.03	0.03	1,1	2	44.80	0.01	0.01	1,1	2	44.56	0.02	0.02	1	3		
Q0052 + 251						Q0121 – 590(78)						Q0134 + 329					
1285Å	45.47	0.04	0.06	20	3	45.12	0.04	0.06	18	3	45.46	0.05	0.15	21	3		
1460Å	45.38	0.04	0.07	20	3	45.06	0.04	0.05	18	3	45.65	0.21	0.21	1	1		
2200Å	45.28	0.05	0.12	23	3	44.96	0.04	0.07	23	3	45.44	0.06	0.20	25	3		
2500Å	45.33	0.05	0.09	21	3	44.98	0.04	0.06	22	3	45.42	0.02	0.02	1,1	2		
2660Å	45.40	0.05	0.12	16	1	44.94	0.05	0.07	22	3	45.42	0.02	0.02	1,1	2		
3023Å	45.15	0.01	0.01	1,1	2	44.86	0.05	0.07	22	3	45.43	0.02	0.02	1,1	2		
4200Å	44.91	0.02	0.02	1,1	2	44.59	0.02	0.03	10	3	45.35	0.04	0.04	1,1	2		
4750Å	44.79	0.03	0.03	1,1	2	44.55	0.04	0.05	10,10	2	45.16	0.06	0.06	1,1	2		
5100Å	44.75	0.04	0.04	1,1	2	44.52	0.04	0.05	10,10	2	45.33	0.05	0.05	1	1		
7500Å	44.67	0.04	0.04	2,1	2	44.16	0.09	0.09	1,1	2	45.06	0.08	0.08	1,1	2		
Q0205 + 024						Q0804 + 761(82)						Q0837 – 120					
1285Å	45.09	0.05	0.10	17	3	45.18	0.05	0.08	18	3	45.35	0.06	0.12	9	3		
1460Å	45.13	0.05	0.08	20	3	45.11	0.04	0.06	19	3	45.30	0.05	0.11	21	3		
2200Å	45.19	0.05	0.09	25	3	45.10	0.04	0.07	24	3	45.10	0.05	0.08	26	3		
2500Å	45.20	0.05	0.08	25	3	45.18	0.04	0.05	24	3	45.05	0.05	0.13	26	3		
2660Å	45.15	0.05	0.10	24	3	45.15	0.04	0.06	24	3	45.35	0.07	0.10	3	1 ^d		
3023Å	45.05	0.02	0.02	1,1	2	45.18	0.04	0.04	1,7	2	44.84	0.13	0.13	1	3		
4200Å	44.85	0.03	0.03	1,1	2	44.92	0.06	0.06	1,1	2	44.58	0.11	0.11	1,1	2		
4750Å	44.83	0.04	0.05	1,2	2	44.80	0.09	0.09	1,1	2	44.54	0.18	0.18	1,1	2		
5100Å	44.73	0.03	0.04	1,2	2	44.72	0.10	0.10	1,1	2	44.44	0.19	0.19	1,1	2		
7500Å	44.57	0.05	0.05	1,1	2	44.60	0.14	0.14	1,1	2	44.46	0.21	0.21	1,1	2		
Q0844 + 349						Q1028 + 313						Q1100 + 772					
1285Å	44.62	0.05	0.09	36	3	45.11	0.05	0.09	20	3	45.69	0.05	0.09	22	3		
1460Å	44.65	0.05	0.11	35	3	45.02	0.05	0.09	20	3	45.63	0.04	0.06	22	3		
2200Å	44.66	0.05	0.15	35	3	44.95	0.04	0.07	25	3	45.55	0.04	0.07	28	3		
2500Å	44.66	0.04	0.06	46	3	45.00	0.04	0.05	25	3	45.66	0.07	0.11	1,29	2		
2660Å	44.61	0.04	0.05	46	3	44.92	0.05	0.08	25	3	45.65	0.02	0.02	1,1	2		
3023Å	44.65	0.07	0.16	10	3	44.95	0.08	0.10	1,32	2	45.62	0.01	0.01	1,1	2		
4200Å	44.47	0.11	0.11	1,1	2	44.73	0.10	0.10	1,1	2	45.41	0.02	0.02	1,1	2		
4750Å	44.45	0.11	0.11	1,1	2	44.68	0.11	0.10	1,2	2	45.36	0.02	0.02	1,1	2		
5100Å	44.38	0.14	0.14	1	3	44.61	0.11	0.11	1,2	2	45.33	0.02	0.02	1,1	2		
7500Å	44.13	0.26	0.26	1,1	2	44.57	0.18	0.18	1,1	2	45.30	0.02	0.02	1,1	2		

Table 16—Continued

λ_o	$\log \nu L_\nu$	^a σ_{avg}	σ_{var}	N ^b	Q ^c	$\log \nu L_\nu$	σ_{avg}	σ_{var}	N	Q	$\log \nu L_\nu$	σ_{avg}	σ_{var}	N	Q
	Q1116 + 215					Q1202 + 281(85)					Q1211 + 143(87)				
1285Å	45.74	0.04	0.07	20	3	44.81	0.05	0.10	11	3	44.94	0.05	0.07	19	3
1460Å	45.70	0.04	0.05	20	3	44.75	0.05	0.11	12	3	44.99	0.05	0.07	19	3
2200Å	45.57	0.04	0.06	25	3	44.70	0.05	0.12	24	3	44.96	0.05	0.08	23	3
2500Å	45.68	0.04	0.06	26	3	44.82	0.04	0.07	25	3	45.05	0.04	0.06	23	3
2660Å	45.81	0.05	0.09	25	1	44.78	0.05	0.10	24	3	45.01	0.04	0.06	23	3
3023Å	45.62	0.01	0.01	1,1	2	44.96	0.06	0.08	1,16	1 ^e	45.01	0.04	0.05	1,29	2
4200Å	45.40	0.02	0.01	2,2	2	44.71	0.04	0.04	1,1	2	44.92	0.00	0.00	1,1	2
4750Å	45.30	0.03	0.04	1,3	2	44.62	0.04	0.04	1,1	2	44.89	0.00	0.00	1,1	2
5100Å	45.26	0.02	0.03	1,3	2	44.56	0.04	0.04	1,1	2	44.87	0.00	0.00	1,1	2
7500Å	45.09	0.04	0.04	1,1	2	44.40	0.07	0.07	1,1	2	44.77	0.00	0.00	1,1	2
	Q1219 + 755					Q1307 + 085					Q1352 + 183				
1285Å	44.49	0.05	0.07	18	3	45.30	0.05	0.08	20	3	45.08	0.05	0.09	38	3
1460Å	44.44	0.05	0.08	18	3	45.23	0.05	0.07	20	3	44.96	0.04	0.07	38	3
2200Å	44.43	0.05	0.09	23	3	45.10	0.05	0.08	25	3	44.87	0.05	0.09	24	3
2500Å	44.53	0.04	0.05	22	3	45.16	0.04	0.06	24	3	44.93	0.05	0.08	25	3
2660Å	44.50	0.04	0.06	23	3	45.16	0.04	0.06	16	3	44.93	0.05	0.11	21	3
3023Å	44.51	0.06	0.07	2,29	2	45.18	0.04	0.07	2,2	2	44.98	0.02	0.02	1,1	2
4200Å	44.26	0.16	0.17	2,2	2	44.98	0.05	0.08	3,3	2	44.79	0.01	0.01	1,1	2
4750Å	44.24	0.17	0.17	2,2	2	44.97	0.07	0.07	2,1	2	44.70	0.02	0.02	1,1	2
5100Å	44.22	0.18	0.19	2,2	2	44.90	0.04	0.04	2,1	2	44.65	0.02	0.02	1,1	2
7500Å	44.07	0.30	0.28	2,2	2	44.75	0.10	0.10	1,2	2	44.57	0.01	0.02	2,1	2
	Q1416 - 129					Q1426 + 015					Q1545 + 210				
1285Å	44.94	0.04	0.14	30	3	45.31	0.04	0.06	18	3	45.40	0.05	0.14	22	3
1460Å	44.92	0.05	0.15	16	3	45.30	0.04	0.05	18	3	45.41	0.04	0.07	21	3
2200Å	45.02	0.05	0.13	16	3	45.14	0.04	0.07	23	3	45.45	0.05	0.08	27	3
2500Å	44.96	0.05	0.08	24	3	45.13	0.04	0.05	23	3	45.50	0.06	0.21	27	3
2660Å	44.96	0.05	0.11	17	3	45.10	0.04	0.05	23	3	45.49	0.10	0.15	1,34	2
3023Å	44.83	0.15	0.26	2,2	2	45.13	0.05	0.05	1,29	2	45.46	0.04	0.04	1,1	2
4200Å	44.52	0.16	0.27	3,2	2	44.76	0.05	0.05	1,1	2	45.21	0.01	0.01	1,1	2
4750Å	44.45	0.12	0.15	2,3	2	44.71	0.06	0.06	1,1	2	45.17	0.00	0.00	1,1	2
5100Å	44.35	0.17	0.27	3,2	2	44.68	0.07	0.07	1,1	2	45.16	0.00	0.00	1,1	2
7500Å	43.91	0.43	0.43	2,1	2	44.57	0.12	0.12	1,1	2	45.09	0.01	0.01	1,1	2
	Q1613 + 658					Q1721 + 343					Q1803 + 676				
1285Å	45.03	0.05	0.11	19	3	45.65	0.05	0.12	20	3	44.98	0.05	0.09	19	3
1460Å	44.90	0.05	0.10	20	3	45.56	0.04	0.06	21	3	44.89	0.05	0.07	19	3
2200Å	44.92	0.04	0.06	24	3	45.45	0.04	0.07	26	3	44.96	0.05	0.10	24	3
2500Å	45.01	0.05	0.08	24	3	45.52	0.04	0.05	26	3	45.01	0.04	0.06	25	3
2660Å	44.97	0.04	0.05	24	3	45.55	0.05	0.08	9	3	44.94	0.04	0.07	24	3
3023Å	44.83	0.02	0.02	1,1	2	45.43	0.06	0.08	1,32	2	44.87	0.01	0.01	1,1	2
4200Å	44.63	0.02	0.02	1,1	2	45.20	0.05	0.05	1,1	2	44.69	0.03	0.03	2,1	2
4750Å	44.59	0.03	0.03	1,1	2	45.12	0.06	0.06	1,1	2	44.66	0.02	0.02	1	3
5100Å	44.54	0.03	0.03	1,1	2	45.08	0.07	0.07	1,1	2	44.61	0.04	0.04	2,1	2
7500Å	44.54	0.05	0.05	7,1	2	45.00	0.09	0.09	4,1	2	44.50	0.04	0.04	1,1	2

Table 16—Continued

λ_o	$\log \nu L_\nu$	σ_{avg}	σ_{var}	N ^b	Q ^c	$\log \nu L_\nu$	σ_{avg}	σ_{var}	N	Q	$\log \nu L_\nu$	σ_{avg}	σ_{var}	N	Q
Q2130 + 099(85)															
1285Å	44.55	0.05	0.12	18	3	45.10	0.05	0.12	17	3	44.68	0.05	0.08	18	3
1460Å	44.62	0.05	0.10	18	3	45.07	0.05	0.09	20	3	44.72	0.05	0.08	17	3
2200Å	44.57	0.05	0.12	22	3	45.06	0.05	0.08	26	3	44.56	0.05	0.10	22	3
2500Å	44.64	0.04	0.05	23	3	45.18	0.04	0.07	26	3	44.70	0.04	0.05	23	3
2660Å	44.54	0.04	0.05	22	3	45.08	0.06	0.15	18	3	44.58	0.05	0.09	23	3
3023Å	44.50	0.05	0.10	8	3	45.19	0.01	0.02	2,2	2	44.71	0.10	0.15	1,22	2
4200Å	44.37	0.05	0.06	3,3	2	45.03	0.01	0.01	2,2	2	44.26	0.08	0.08	1,1	1
4750Å	44.31	0.04	0.05	3,3	2	44.96	0.02	0.02	2,2	2	44.42	0.04	0.04	1,1	2
5100Å	44.27	0.04	0.04	3	3	44.94	0.02	0.03	2,2	2	44.48	0.03	0.03	1,1	2
7500Å	44.12	0.11	0.13	2,3	2	44.89	0.02	0.02	2	3	44.52	0.04	0.04	1,1	2

^aValues of $\log L$ are $\log_{10} < \nu L_\nu >$ where the average is taken over the indicated spectral range. When no datapoints lie within the band, the value νL_ν is determined, as described in the text, by interpolating between the averaged fluxes, $< \nu L_\nu >$, where the averages are taken over the first 50Å longwards and shortwards of the nearest datapoint on the long and short wavelength sides of the band, respectively.

^bN is the number of datapoints within the band. When no datapoints lie within the band, the column for N contains the number of datapoints within the 50Å bands on the long and short wavelength sides (N_{long} , N_{short}).

^cThe numbers in this column indicate the confidence that the computed luminosity represents the continuum level: 3 signifies that the luminosity was computed directly from points within the band and represents the continuum level well; 2 that it was interpolated but looks reasonable; 1 that it does not represent the continuum level well; and 0 that it could not be computed because of insufficient data coverage to the red.

^dAt the redshift of Q0837-120, the 2660Å band falls on long wavelength edge of the LWP spectrum (LWR04214) which is (noisy and) rising to longer wavelengths, possibly because it is close to MgIIλ2798. Hence, the average at 2660Å overestimates the continuum level.

^eThe 3023Å average in Q1202+281 (1985) is interpolated from the IUE spectrum and the B band photometry. The edge of the LWP spectrum (LWP04904) rises toward longer wavelengths, probably as it approaches MgIIλ2978. Thus the interpolated value overestimates the continuum.

Table 17. UV luminosities

Quasar	1100-1130Å				1150-1170Å			
	$\log(\nu L_\nu)$	σ_{avg}	σ_{var}	N	$\log(\nu L_\nu)$	σ_{avg}	σ_{var}	N
Q0000-263 ^a	47.48	0.02	0.12	44	47.46	0.03	0.12	29
Q0000-263	47.78	0.04	0.04	185
Q0000-263	47.79	0.05	0.05	185
Q0014+813 ^a	47.99	0.01	0.03	21	47.94	0.01	0.05	13
Q0014+813	48.08	0.04	0.05	526	48.09	0.04	0.05	350
Q0055-269 ^a	47.06	0.03	0.10	18	47.07	0.03	0.10	11
Q0114-089
Q0347-383 ^a	47.09	0.02	0.07	16	46.74	0.10	0.31	11
Q0420-388 ^a	47.33	0.02	0.06	16	47.38	0.02	0.05	11
Q0420-388	47.46	0.04	0.04	1896	47.48	0.04	0.05	1213
Q0636+680 ^a	47.63	0.01	0.03	20	47.64	0.01	0.04	13
Q0636+680	47.75	0.04	0.04	501	47.80	0.04	0.05	334
Q0956+122 ^a	47.32	0.01	0.05	88	47.18	0.02	0.10	58
Q1159+123 ^a	47.11	0.02	0.11	37	47.05	0.03	0.12	24
Q1208+101 ^a	47.29	0.02	0.10	69	47.28	0.02	0.10	45
Q1208+101	47.45	0.04	0.05	118
Q1208+101	47.47	0.04	0.04	118
Q1935-692 ^a	47.24	0.02	0.09	16	47.21	0.02	0.07	11
Q1946+7658 ^a	47.71	0.02	0.10	44	47.53	0.05	0.25	29
Q1946+7658	47.83	0.04	0.04	501	47.84	0.04	0.04	334
Q2000-330 ^a	47.44	0.04	0.14	18	47.26	0.04	0.15	12
Q2126-158 ^a	47.36	0.01	0.05	20	47.46	0.01	0.04	14
Q2126-158	47.51	0.04	0.05	1896	47.52	0.04	0.05	1212
Q2204-408 ^a	46.81	0.03	0.10	15	46.99	0.03	0.08	11
Q0007+106	44.82	0.10	0.20	2	44.85	0.03	0.09	34
Q0026+129	45.17	0.05	0.09	18	45.23	0.05	0.12	15
Q0050+124	44.41	0.04	0.11	30
Q0052+251	45.52	0.04	0.05	29	45.51	0.05	0.07	19
Q0121-590(79)
Q0134+329	45.50	0.05	0.10	15	45.50	0.05	0.09	8
Q0205+024	45.06	0.05	0.08	29	45.19	0.05	0.09	16
Q0804+761(82)	45.28	0.05	0.07	12	45.23	0.04	0.06	19
Q0837-120	45.32	0.05	0.09	26	45.34	0.05	0.12	17
Q0844+349	44.62	0.05	0.09	26
Q1028+313	45.12	0.05	0.09	30	45.11	0.05	0.07	20
Q1100+772	45.68	0.05	0.10	34	45.79	0.05	0.08	22
Q1116+215	45.74	0.04	0.06	30	45.73	0.04	0.06	20
Q1202+281(85)	44.65	0.05	0.11	16	44.81	0.06	0.14	10
Q1211+143(87)	44.98	0.05	0.09	19
Q1219+755	44.51	0.05	0.09	18
Q1307+085	45.41	0.04	0.07	29	45.31	0.05	0.07	19
Q1352+183	45.13	0.04	0.07	58	45.04	0.05	0.10	38
Q1416-129	44.99	0.04	0.23	43	45.01	0.04	0.12	26
Q1426+015	45.37	0.04	0.05	19
Q1545+210	45.39	0.05	0.15	32	45.52	0.05	0.14	21
Q1613+658	45.01	0.05	0.09	28	44.99	0.05	0.11	19
Q1721+343	45.54	0.05	0.10	31	45.57	0.05	0.11	21
Q1803+676	44.90	0.05	0.10	29	45.01	0.05	0.11	19
Q2130+099(85)	44.63	0.06	0.13	7
Q2135-147	45.02	0.05	0.12	28	45.08	0.05	0.11	20
Q2251-178	44.77	0.05	0.08	17

^aData not corrected for Ly α forest absorption.

Table 18. Linear Least Square fits from 1285 – 5100Å

Quasar	All 9 points from 1285-5100Å			5 points, excluding ‘3000Å bump’			
	χ^2_r (dof) ^a	P(χ^2) ^b	α_{ouv}	χ^2_r (dof) ^a	P(χ^2) ^b	α_{ouv}	Δ^c
High redshift sample							
Q0000-263	1.7 (5)	0.8777	-0.30 ± 0.02	4.3 (1)	0.9609	-0.29 ± 0.02	0.01
Q0014+813	16.4 (6)	1.0	-0.14 ± 0.03	2.9 (3)	0.9674	-0.13 ± 0.01	0.01
Q0055-269	8.1 (6)	1.0	-0.40 ± 0.10	3.8 (2)	0.9765	-0.40 ± 0.04	0.00
Q0114-089	1.6 (6)	0.8707	-0.27 ± 0.02	2.0 (2)	0.8672	-0.26 ± 0.01	0.00
Q0347-383	5.8 (7)	1.0	-0.23 ± 0.07	3.6 (3)	0.9868	-0.25 ± 0.04	-0.02
Q0420-388	1.7 (7)	0.8941	-0.61 ± 0.02	1.8 (3)	0.8565	-0.61 ± 0.01	-0.00
Q0636+680	9.0 (7)	1.0	-0.57 ± 0.04	16.8 (3)	1.0	-0.56 ± 0.05	0.01
Q0956+122	4.3 (7)	0.9999	-0.22 ± 0.05	6.4 (3)	0.9997	-0.22 ± 0.06	-0.00
Q1159+123	1.8 (6)	0.8965	-0.67 ± 0.02	2.2 (3)	0.9140	-0.67 ± 0.02	0.01
Q1208+101	5.4 (6)	1.0	0.15 ± 0.09	4.0 (2)	0.9810	0.16 ± 0.05	0.01
Q1935-692	6.3 (7)	1.0	0.27 ± 0.10	2.6 (3)	0.9472	0.23 ± 0.06	-0.03
Q1946+7658	7.3 (6)	1.0	-0.50 ± 0.03	8.8 (3)	1.0	-0.51 ± 0.03	-0.01
Q2000-330	2.0 (6)	0.9428	-0.20 ± 0.05	2.7 (2)	0.9350	-0.20 ± 0.02	0.01
Q2126-158	2.9 (7)	0.9949	-0.41 ± 0.03	1.8 (3)	0.8459	-0.42 ± 0.01	-0.01
Q2204+408	16.2 (7)	1.0	-0.72 ± 0.11	1.8 (3)	0.8574	-0.74 ± 0.03	-0.02
Low redshift sample							
Q0007+106	11.7 (7)	1.0	-0.25 ± 0.16	1.8 (3)	0.8453	-0.30 ± 0.02	-0.05
Q0026+129	22.3 (6)	1.0	-0.22 ± 0.09	178.0 (3)	1.0	-0.26 ± 0.03	-0.05
Q0050+124	18.2 (7)	1.0	-1.20 ± 0.17	1.8 (3)	0.8608	-1.23 ± 0.01	-0.03
Q0052+251	19.6 (6)	1.0	0.18 ± 0.13	3.8 (3)	0.9898	0.15 ± 0.04	-0.03
Q0121-590(78)	5.9 (7)	1.0	0.04 ± 0.11	1.8 (3)	0.8510	0.01 ± 0.01	-0.03
Q0134+329	5.0 (5)	0.9999	-0.59 ± 0.14	11.0 (1)	0.9991	-0.61 ± 0.16	-0.02
Q0205+024	9.6 (7)	1.0	-0.36 ± 0.17	3.2 (3)	0.9766	-0.43 ± 0.06	-0.07
Q0804+761(82)	8.0 (7)	1.0	-0.35 ± 0.17	2.6 (3)	0.9516	-0.36 ± 0.08	-0.02
Q0837-120	2.4 (6)	0.9714	0.54 ± 0.08	1.8 (3)	0.8504	0.51 ± 0.03	-0.03
Q0844+349	2.8 (7)	0.9933	-0.59 ± 0.10	1.9 (3)	0.8720	-0.61 ± 0.04	-0.02
Q1028+313	2.6 (7)	0.9891	-0.25 ± 0.10	2.0 (3)	0.8811	-0.26 ± 0.04	-0.01
Q1100+772	18.0 (7)	1.0	-0.45 ± 0.12	2.2 (3)	0.9157	-0.45 ± 0.02	-0.00
Q1116+215	33.9 (6)	1.0	-0.24 ± 0.12	3.6 (3)	0.9875	-0.24 ± 0.05	0.00
Q1202+281(85)	3.4 (6)	0.9979	-0.70 ± 0.09	3.5 (3)	0.9844	-0.70 ± 0.07	-0.00
Q1211+143(87)	322.2 (7)	1.0	-0.86 ± 0.08	235.8 (3)	1.0	-0.87 ± 0.04	-0.01
Q1219+755	4.2 (7)	0.9999	-0.56 ± 0.14	1.7 (3)	0.8409	-0.58 ± 0.02	-0.01
Q1307+085	2.9 (7)	0.9953	-0.42 ± 0.08	2.0 (3)	0.8921	-0.40 ± 0.04	0.02
Q1352+183	13.9 (7)	1.0	-0.42 ± 0.11	13.7 (3)	1.0	-0.40 ± 0.07	0.02
Q1416-129	9.9 (7)	1.0	0.01 ± 0.22	1.8 (3)	0.8591	-0.07 ± 0.05	-0.08
Q1426+015	4.3 (7)	0.9999	0.10 ± 0.12	1.8 (3)	0.8637	0.09 ± 0.03	-0.01
Q1545+210	106.5 (7)	1.0	-0.54 ± 0.16	4.7 (3)	0.9970	-0.57 ± 0.02	-0.04
Q1613+658	9.1 (7)	1.0	-0.24 ± 0.15	2.5 (3)	0.9452	-0.28 ± 0.05	-0.04
Q1721+343	4.6 (7)	1.0	-0.09 ± 0.13	2.0 (3)	0.8880	-0.10 ± 0.04	-0.01
Q1803+676	10.2 (7)	1.0	-0.41 ± 0.14	2.3 (3)	0.9275	-0.46 ± 0.04	-0.05
Q2130+099(85)	4.2 (7)	0.9999	-0.46 ± 0.11	2.6 (3)	0.9487	-0.49 ± 0.06	-0.04
Q2135-147	19.6 (7)	1.0	-0.78 ± 0.12	6.3 (3)	0.9997	-0.78 ± 0.04	0.00
Q2251-178	3.7 (6)	0.9989	-0.60 ± 0.13	4.2 (2)	0.9852	-0.56 ± 0.07	0.04

^aReduced χ^2 of the power law fit. The number of degrees of freedom is shown in parenthesis.

^bProbability of randomly obtaining a value of χ^2_r better than that computed from the fit. These are all quite high, indicating either the fits are poor, or the errors are underestimated.

^c Δ is the difference between the spectral indices computed using all points and using all but the 3000Å bump points.

Table 19. Statistics on the 1285-5100Å optical/UV spectral indices, α_{ouv}

Sample ^a	N_{obj}	median	mean	σ_{N-1}	$\frac{\sigma_{N-1}}{\sqrt{N}}$
low z (E)	27	−0.40	−0.38	0.35	0.07
high z (E)	15	−0.29	−0.32	0.28	0.07
low+high z (E)	42	−0.40	−0.36	0.32	0.05
low z (A)	27	−0.41	−0.36	0.36	0.07
high z (A)	15	−0.30	−0.32	0.28	0.07
low+high z (A)	42	−0.38	−0.34	0.33	0.05

^a (A): Power law fits were made to all good luminosities (marked 3 or 2 in tables 15 and 16) between 1285Å and 5100Å; (E): Luminosities between 2000Å and 4000Å were excluded from the power law fits.

Table 20. UV and optical point-to-point spectral indices

Object	$\alpha_{1115\text{\AA}}^{1285\text{\AA}}$	$\alpha_{1160\text{\AA}}^{1285\text{\AA}}$	$\alpha_{1285\text{\AA}}^{1460\text{\AA}}$	$\alpha_{1285\text{\AA}}^{2200\text{\AA}}$	$\alpha_{1285\text{\AA}}^{3023\text{\AA}}$	$\alpha_{4200\text{\AA}}^{5100\text{\AA}}$	$\alpha_{3023\text{\AA}}^{5100\text{\AA}}$
High z sample							
Q0000 - 263	...	0.51 \pm 1.03 ^a	0.12 \pm 0.37	-0.27 \pm 0.47	-0.28 \pm 0.09
Q0014 + 813	-0.71 \pm 0.72	-0.46 \pm 1.00	-0.09 \pm 0.20	0.36 \pm 0.08	-0.03 \pm 0.03	0.15 \pm 0.15	-0.23 \pm 0.05
Q0055 - 269	0.44 \pm 0.48	-0.66 \pm 0.27	-0.60 \pm 0.14	-0.95 \pm 0.96	-0.06 \pm 0.31
Q0114 - 089	-0.28 \pm 0.30	-0.17 \pm 0.08	-0.24 \pm 0.18	-0.12 \pm 0.80	-0.28 \pm 0.36
Q0347 - 383	0.47 \pm 0.31	-0.48 \pm 0.13	-0.36 \pm 0.13	-0.27 \pm 0.86	0.09 \pm 0.33
Q0420 - 388	-0.97 \pm 0.74	-0.55 \pm 1.02	-0.80 \pm 0.34	-0.59 \pm 0.08	-0.65 \pm 0.10	-0.64 \pm 0.57	-0.54 \pm 0.22
Q0636 + 680	-0.69 \pm 0.71	0.55 \pm 0.99	0.22 \pm 0.13	-0.44 \pm 0.07	-0.62 \pm 0.06	0.19 \pm 0.35	-0.31 \pm 0.11
Q0956 + 122	0.57 \pm 0.33	-0.16 \pm 0.18	-0.25 \pm 0.07	1.01 \pm 0.46	0.14 \pm 0.13
Q1159 + 123	-0.17 \pm 0.42	-0.52 \pm 0.13	-0.45 \pm 0.07	-0.85 \pm 0.57	-1.01 \pm 0.16
Q1208 + 101	...	-1.65 \pm 1.10 ^b	-1.01 \pm 0.62	-0.38 \pm 0.16	-0.12 \pm 0.09
Q1935 - 692	0.35 \pm 0.34	-0.05 \pm 0.10	0.15 \pm 0.16	-0.61 \pm 0.83	0.36 \pm 0.33
Q1946 + 7658	-1.70 \pm 0.71	-1.76 \pm 0.99	0.03 \pm 0.17	-0.97 \pm 0.04	-0.51 \pm 0.02	-0.14 \pm 0.18	-0.33 \pm 0.05
Q2000 - 330	0.24 \pm 0.38	-0.16 \pm 0.28	-0.28 \pm 0.13
Q2126 - 158	-1.46 \pm 0.71	-1.51 \pm 0.99	-0.41 \pm 0.17	-0.62 \pm 0.08	-0.47 \pm 0.06	-0.64 \pm 0.53	-0.39 \pm 0.15
Q2204 - 408	-0.75 \pm 0.25	-1.12 \pm 0.07	-1.20 \pm 0.16	-0.58 \pm 0.78	0.10 \pm 0.33
Low z sample							
Q0007 + 106	-2.54 \pm 1.72	-2.36 \pm 1.07	-0.10 \pm 0.90	-0.85 \pm 0.20	-0.66 \pm 0.14	-0.58 \pm 0.71	0.28 \pm 0.27
Q0026 + 129	-2.54 \pm 1.11	-1.89 \pm 1.61	0.45 \pm 1.20	-0.82 \pm 0.31	-0.35 \pm 0.14	0.28 \pm 0.24	0.06 \pm 0.12
Q0050 + 124	...	-1.60 \pm 1.16	-1.12 \pm 0.89	-1.64 \pm 0.21	-1.82 \pm 0.14	-1.17 \pm 0.53	-0.25 \pm 0.24
Q0052 + 251	-0.12 \pm 1.01	-0.12 \pm 1.43	0.70 \pm 1.14	-0.19 \pm 0.29	-0.13 \pm 0.12	0.82 \pm 0.48	0.74 \pm 0.16
Q0121 - 590(78)	0.09 \pm 1.13	-0.32 \pm 0.27	-0.30 \pm 0.17	-0.16 \pm 0.49	0.50 \pm 0.26
Q0134 + 329	-0.20 \pm 1.17	0.11 \pm 1.66	-4.54 \pm 3.92	-0.94 \pm 0.34	-0.94 \pm 0.16	-0.73 \pm 0.70	-0.55 \pm 0.23
Q0205 + 024	-1.44 \pm 1.09	1.32 \pm 1.54	-1.73 \pm 1.21	-1.43 \pm 0.29	-0.90 \pm 0.14	0.43 \pm 0.51	0.39 \pm 0.17
Q0804 + 761(82)	0.70 \pm 1.07	0.15 \pm 1.45	0.17 \pm 1.17	-0.67 \pm 0.28	-1.01 \pm 0.16	1.39 \pm 1.35	1.02 \pm 0.46
Q0837 - 120	-1.38 \pm 1.19	-1.26 \pm 1.73	-0.19 \pm 1.35	0.06 \pm 0.31	0.37 \pm 0.39	0.61 \pm 2.57	0.73 \pm 1.00
Q0844 + 349	...	-1.02 \pm 1.46	-1.50 \pm 1.18	-1.14 \pm 0.29	-1.08 \pm 0.22	-0.01 \pm 2.18	0.20 \pm 0.70
Q1028 + 313	-0.86 \pm 1.06	-0.96 \pm 1.46	0.73 \pm 1.19	-0.29 \pm 0.28	-0.58 \pm 0.24	0.38 \pm 1.73	0.51 \pm 0.58
Q1100 + 772	-1.16 \pm 1.06	1.40 \pm 1.47	-0.05 \pm 1.16	-0.44 \pm 0.28	-0.83 \pm 0.13	-0.04 \pm 0.35	0.27 \pm 0.11
Q1116 + 215	-0.89 \pm 1.02	-1.16 \pm 1.42	-0.43 \pm 1.13	-0.27 \pm 0.27	-0.67 \pm 0.12	0.71 \pm 0.41	0.57 \pm 0.11
Q1202 + 281(85)	-3.58 \pm 1.16	-0.84 \pm 1.78	0.01 \pm 1.32	-0.52 \pm 0.30	-1.42 \pm 0.22	0.72 \pm 0.67	0.76 \pm 0.34
Q1211 + 143(87)	...	-0.02 \pm 1.47	-1.89 \pm 1.16	-1.11 \pm 0.28	-1.20 \pm 0.17	-0.37 \pm 0.02	-0.38 \pm 0.19
Q1219 + 755	...	-0.42 \pm 1.47	-0.08 \pm 1.17	-0.75 \pm 0.28	-1.06 \pm 0.21	-0.52 \pm 2.86	0.29 \pm 0.85
Q1307 + 085	0.68 \pm 1.03	-0.89 \pm 1.45	0.29 \pm 1.16	-0.11 \pm 0.28	-0.66 \pm 0.17	-0.02 \pm 0.76	0.22 \pm 0.24
Q1352 + 183	-0.28 \pm 1.03	-1.95 \pm 1.45	1.11 \pm 1.14	-0.10 \pm 0.28	-0.74 \pm 0.13	0.61 \pm 0.22	0.47 \pm 0.10
Q1416 - 129	-0.28 \pm 0.83	0.51 \pm 1.14	-0.60 \pm 1.09	-1.32 \pm 0.27	-0.70 \pm 0.41	0.98 \pm 2.82	1.11 \pm 0.99
Q1426 + 015	...	0.34 \pm 1.40	-0.70 \pm 1.12	-0.28 \pm 0.27	-0.52 \pm 0.17	-0.08 \pm 1.03	0.97 \pm 0.37
Q1545 + 210	-1.16 \pm 1.17	1.56 \pm 1.66	-1.20 \pm 1.23	-1.21 \pm 0.29	-1.15 \pm 0.17	-0.33 \pm 0.10	0.32 \pm 0.17
Q1613 + 658	-1.37 \pm 1.09	-1.88 \pm 1.56	1.33 \pm 1.24	-0.52 \pm 0.28	-0.46 \pm 0.14	0.04 \pm 0.40	0.27 \pm 0.15
Q1721 + 343	-2.80 \pm 1.11	-2.92 \pm 1.56	0.68 \pm 1.20	-0.12 \pm 0.29	-0.39 \pm 0.22	0.50 \pm 0.96	0.55 \pm 0.40
Q1803 + 676	-2.24 \pm 1.07	-0.34 \pm 1.52	0.71 \pm 1.18	-0.90 \pm 0.29	-0.70 \pm 0.13	-0.07 \pm 0.53	0.15 \pm 0.16
Q2130 + 099(85)	...	0.76 \pm 1.81	-2.25 \pm 1.26	-1.09 \pm 0.30	-0.86 \pm 0.19	0.15 \pm 0.73	0.01 \pm 0.28
Q2135 - 147	-2.30 \pm 1.14	-1.38 \pm 1.59	-0.57 \pm 1.25	-0.86 \pm 0.29	-1.26 \pm 0.14	0.05 \pm 0.29	0.12 \pm 0.11
Q2251 - 178	...	1.21 \pm 1.47	-1.77 \pm 1.18	-0.51 \pm 0.28	-1.09 \pm 0.30	-3.68 \pm 1.00	-0.01 \pm 0.46

^aUsed the Ly α forest corrected spectrophotometry from CTIO. The spectral index that is measured from the corrected MMT spectrophotometry is similar: $\alpha(1160, 1285) = 0.57 \pm 1.06$.

^bUsed the Ly α forest corrected shorter wavelength spectrophotometry from the MMT. The spectral index that is measured from the longer wavelength set is $\alpha(1160, 1285) = -2.01 \pm 1.10$.

Table 21. Linear-regression fits

α	α_o	$\log(L_\nu)$	$\log(1+z)$	p_{K-T} ^a	N_{obj}	reference
α_{uv} vs. L_{uv} : $H_o = 75$ km/s/Mpc, $q_o = 0.1$						
$\alpha(1285\text{\AA}, 1460\text{\AA})$ ^b	-6.0 ± 5.0	0.13 ± 0.11	...	58	41	this work
$\alpha(1285\text{\AA}, 2200\text{\AA})$	-7.12 ± 2.49	0.14 ± 0.05	...	99	42	this work
$\alpha(1285\text{\AA}, 1460\text{\AA})$ ^b	-0.34 ± 0.18	...	0.45 ± 0.46	82	41	this work
$\alpha(1285\text{\AA}, 2200\text{\AA})$	-0.71 ± 0.09	...	0.48 ± 0.23	98	42	this work
α_{uv} vs. L_{uv} : Comparison with O'Brien et al. (1988; $H_o = 50$ km/s/Mpc, $q_o = 0$)						
$\alpha_{UV,OGW88}$	-1.58	0.02 ± 0.05	0.71 ± 0.20	$93, < 80$ ^d	68	O'Brien et al. 1988
$\alpha_{UV,OGW88}$ ^c	-5.64 ± 1.43	0.16 ± 0.05	...	> 99	68	O'Brien et al. 1988
$\alpha(1285\text{\AA}, 1460\text{\AA})$ ^b	-3.8 ± 3.2	0.12 ± 0.10	...	54	41	this work
$\alpha(1285\text{\AA}, 2200\text{\AA})$	-4.7 ± 1.6	0.13 ± 0.05	...	99.0	42	this work
α_{uv} vs. L_{uv} : Comparison with Cheng et al. (1991; $H_o = 50$ km/s/Mpc, $q_o = 1$)						
$\alpha_{UV,CGK91}$	0.88 ± 0.06 ^e	0.06 ± 0.08	0.82 ± 0.35	99.5 ^f , NS ^g		Cheng et al. 1991
$\alpha_{UV,CGK91}$	0.85 ± 0.06 ^e	0.2 ± 0.05		Cheng et al. 1991
$\alpha(1285\text{\AA}, 1460\text{\AA})$ ^b	-5.5 ± 4.4	0.17 ± 0.14	...	56	41	this work
$\alpha(1285\text{\AA}, 2200\text{\AA})$	-6.7 ± 2.2	0.20 ± 0.07	...	98.98	42	this work
α_{ouv} vs. $L_{1285\text{\AA}}$: $H_o = 75$ km/s/Mpc, $q_o = 0.1$						
α_{ouv}	-2.7 ± 1.9	0.05 ± 0.04	...	97	42	high+low z, this work
α_{ouv}	-5.3 ± 13.68	0.11 ± 0.29	...	54	15	high z, this work
α_{ouv}	-23.01 ± 7.58	0.50 ± 0.17	...	99.5	27	low z, this work
α_{ouv} vs. $L_{4200\text{\AA}}$: $H_o = 75$ km/s/Mpc, $q_o = 0.1$						
α_{ouv}	-0.99 ± 1.98	0.01 ± 0.04	...	33	42	high+low z, this work
α_{ouv}	17.03 ± 11.00	-0.37 ± 0.23	...	65	15	high z, this work
α_{ouv}	-0.45 ± 9.58	0.002 ± 0.214	...	12	27	low z, this work
α_{ouv} vs. $L_{4750\text{\AA}}$: $H_o = 75$ km/s/Mpc, $q_o = 0.1$						
α_{ouv}	-0.85 ± 2.04	0.01 ± 0.05	...	21	42	high+low z, this work
α_{ouv}	20.08 ± 12.27	-0.43 ± 0.26	...	83	15	high z, this work
α_{ouv}	1.47 ± 10.55	-0.04 ± 0.24	...	9	27	low z, this work

^aOne minus the percentage probability of a chance correlation, based on a Kendall-tau correlation test.

^bQ0134+329 was not used in the fits because its 1460\text{\AA} luminosity, hence also its 1285-1460\text{\AA} slope, are discrepant.

^cO'Brien et al. measure the UV spectral index from Ly\alpha to 1900\text{\AA}.

^dThe first number is the significance of the $\alpha - \log(1+z)$ partial correlation, and the second, that of the $\alpha - \log L$ one.

^eCheng et al. (1991) have fit to normalized variables, hence the quite different intercept values.

^fOne-tailed significance of the $\alpha-z$ partial correlation when $\log L$ is included in the fit.

^gNo number given, but Cheng et al. state the relation between α and L is not significant.

^hSignificance not given.

Table 22. UV slope change

sample	Δ ^a	total ^b	average	σ_{N-1}	σ_{avg}	+	0	–
All	Δ_{02}^{23d}	23	1.28	1.27	0.26	10	13	0
	Δ_{12}^{23d}	32	0.28	1.79	0.32	7	20	5
	Δ_{02}^{24}	23	0.71	1.07	0.22	9	12	2
	Δ_{12}^{24}	32	–0.033	1.37	0.24	4	21	7
low z	Δ_{02}^{23d}	18	1.38	1.39	0.33	7	11	0
	Δ_{12}^{23d}	25	0.23	1.98	0.40	5	15	5
	Δ_{02}^{24}	18	0.72	1.20	0.28	6	10	2
	Δ_{12}^{24}	25	–0.13	1.46	0.29	3	16	6
high z	Δ_{02}^{23}	5	0.90	0.58	0.26	3	2	0
	Δ_{12}^{23}	7	0.46	0.86	0.33	2	5	0
	Δ_{02}^{24}	5	0.66	0.34	0.15	3	2	0
	Δ_{12}^{24}	7	0.32	0.97	0.37	1	5	1

^a $\Delta_{02}^{23} \equiv \alpha_{1115\text{\AA}}^{1285\text{\AA}} - \alpha_{1285\text{\AA}}^{1460\text{\AA}}$; $\Delta_{12}^{23} \equiv \alpha_{1160\text{\AA}}^{1285\text{\AA}} - \alpha_{1285\text{\AA}}^{1460\text{\AA}}$; $\Delta_{02}^{24} \equiv \alpha_{1115\text{\AA}}^{1285\text{\AA}} - \alpha_{1285\text{\AA}}^{2200\text{\AA}}$; and $\Delta_{12}^{24} \equiv \alpha_{1160\text{\AA}}^{1285\text{\AA}} - \alpha_{1285\text{\AA}}^{2200\text{\AA}}$

^bNumber of sample objects with measured spectral indices

^cNumber of objects showing a $> 1\sigma$ turndown (+), turnup (–) or whose spectral slopes on other either side of Ly α differ by less than 1σ (0).

^dStatistics involving α_{23} exclude Q0134+329 from the sample.

Table 23. Measures of the $\lambda \sim 3000\text{\AA}$ excess

Quasar	R(2500\AA) ^a	R(2660\AA) ^a	excess ^b	‘EW(2200-3023)’ ^c	quality ^d
High redshift sample					
Q0000 – 263	0.016 \pm 0.029	0.011 \pm 0.103	0.03 \pm 0.09	23 \pm 77	2333
Q0014 + 813	–0.035 \pm 0.007	–0.045 \pm 0.004	(–0.12 \pm 0.01)	(–93 \pm 6)	1333
Q0055 – 269	0.100 \pm 0.025	0.133 \pm 0.022	0.28 \pm 0.04	232 \pm 44	2332
Q0114 – 089	(0.005 \pm 0.082)	(0.002 \pm 0.077)	–0.01 \pm 0.08	–8 \pm 70	3222
Q0347 – 383	(0.070 \pm 0.099)	(0.112 \pm 0.090)	0.21 \pm 0.10	172 \pm 97	3223
Q0420 – 388A	(0.034 \pm 0.049)	(0.025 \pm 0.051)	0.04 \pm 0.05	35 \pm 46	3223
Q0636 + 680	(0.003 \pm 0.019)	0.005 \pm 0.020	0.02 \pm 0.02	19 \pm 19	2233
Q0956 + 122	(0.027 \pm 0.028)	0.036 \pm 0.020	0.06 \pm 0.03	51 \pm 27	2233
Q1159 + 123	–0.001 \pm 0.017	0.009 \pm 0.017	(–0.03 \pm 0.02)	(–28 \pm 18)	2331
Q1208 + 101	(0.093 \pm 0.026)	(0.079 \pm 0.024)	(0.22 \pm 0.03)	(179 \pm 31)	2222
Q1935 – 692	(0.137 \pm 0.117)	(0.135 \pm 0.104)	0.28 \pm 0.12	224 \pm 123	3223
Q1946 + 769	(0.028 \pm 0.022)	(0.024 \pm 0.016)	(0.11 \pm 0.02)	(84 \pm 17)	1223
Q2000 – 330	0.048 \pm 0.041	–0.022 \pm 0.038	0.04 \pm 0.05	33 \pm 45	2333
Q2126 – 158	(0.012 \pm 0.029)	–0.001 \pm 0.018	0.04 \pm 0.03	31 \pm 22	3233
Q2204 – 408	(0.134 \pm 0.111)	(0.128 \pm 0.114)	0.35 \pm 0.11	295 \pm 128	3223
Low redshift sample					
Q0007 + 106	0.245 \pm 0.032	0.210 \pm 0.032	0.56 \pm 0.04	460 \pm 52	3332
Q0026 + 129	0.109 \pm 0.048	(0.166 \pm 0.055)	(0.34 \pm 0.06)	(270 \pm 65)	3312
Q0050 + 124	0.243 \pm 0.033	0.185 \pm 0.033	0.57 \pm 0.04	472 \pm 53	3333
Q0052 + 251	0.204 \pm 0.047	(0.303 \pm 0.051)	(0.58 \pm 0.06)	(495 \pm 77)	3312
Q0121 – 590(78)	0.154 \pm 0.044	0.143 \pm 0.045	0.34 \pm 0.05	288 \pm 59	3333
Q0134 + 329	(0.065 \pm 0.024)	(0.081 \pm 0.024)	0.20 \pm 0.04	172 \pm 35	3222
Q0205 + 024	0.238 \pm 0.045	0.208 \pm 0.047	0.59 \pm 0.05	480 \pm 67	3332
Q0804 + 761(82)	0.192 \pm 0.044	0.187 \pm 0.044	0.51 \pm 0.05	440 \pm 63	3332
Q0837 – 120	0.121 \pm 0.049	(0.460 \pm 0.068)	(0.70 \pm 0.09)	(614 \pm 138)	3313
Q0844 + 349	0.121 \pm 0.044	0.085 \pm 0.044	0.29 \pm 0.06	243 \pm 63	3333
Q1028 + 313	0.129 \pm 0.044	0.062 \pm 0.046	0.24 \pm 0.06	202 \pm 65	3332
Q1100 + 772	(0.141 \pm 0.072)	(0.147 \pm 0.020)	0.31 \pm 0.06	270 \pm 58	3222
Q1116 + 215	0.160 \pm 0.044	(0.307 \pm 0.046)	(0.51 \pm 0.05)	(449 \pm 67)	3313
Q1202 + 281(85)	0.112 \pm 0.045	0.085 \pm 0.047	(0.31 \pm 0.06)	(228 \pm 70)	3331
Q1211 + 143(87)	0.119 \pm 0.044	0.085 \pm 0.044	0.22 \pm 0.05	182 \pm 53	3332
Q1219 + 755	0.176 \pm 0.044	0.160 \pm 0.044	0.42 \pm 0.06	353 \pm 68	3332
Q1307 + 085	0.045 \pm 0.044	0.066 \pm 0.045	0.11 \pm 0.05	107 \pm 49	3332
Q1352 + 183	0.057 \pm 0.045	0.074 \pm 0.049	0.16 \pm 0.05	153 \pm 48	3332
Q1416 – 129	0.269 \pm 0.046	0.296 \pm 0.050	0.86 \pm 0.08	702 \pm 130	3332
Q1426 + 015	0.111 \pm 0.044	0.112 \pm 0.044	0.31 \pm 0.05	279 \pm 58	3332
Q1545 + 210	0.203 \pm 0.059	0.203 \pm 0.099	0.54 \pm 0.09	449 \pm 112	3322
Q1613 + 658	0.232 \pm 0.045	0.206 \pm 0.044	0.50 \pm 0.05	411 \pm 63	3332
Q1721 + 343	0.148 \pm 0.044	0.203 \pm 0.046	0.37 \pm 0.06	319 \pm 67	3332
Q1803 + 676	0.212 \pm 0.044	0.162 \pm 0.045	0.46 \pm 0.05	373 \pm 52	3332
Q2130 + 099(85)	0.181 \pm 0.044	0.098 \pm 0.044	0.32 \pm 0.05	261 \pm 59	3333
Q2135 – 147	0.146 \pm 0.044	0.049 \pm 0.055	0.27 \pm 0.05	224 \pm 53	3332
Q2251 – 178	0.120 \pm 0.044	0.011 \pm 0.046	0.17 \pm 0.07	148 \pm 75	3332

^aValues in parentheses were not plotted or used in the analysis, since they rely solely on interpolated fluxes or were determined using a discrepant flux point.

^bThe excess is defined as $(L_{total} – L_c)/L_c$ between 2200\AA and 3023\AA, where L_c is determined from the power law fit through the average fluxes in the narrow continuum bands from 1285\AA- 5100\AA but not including those between 2000\AA and 4000\AA.

^c‘EW(2200-3023)’ is computed from the 4 narrow band average fluxes at 2200\AA, 2500\AA, 2660\AA, and 3023\AA and the continuum level as determined by the power law fits described in the previous note.

^dThe digits, left to right, represent the quality of the average narrow band fluxes at 2200\AA, 2500\AA, 2660\AA and 3023\AA, as follows: 3 — directly computed; 2 — had to be interpolated; and 1 — look discrepant.

Table 24. Optical change of slope

Sample	Short λ (UV) spectral index				Long λ (optical) spectral index			
	N_{obj}	avg	σ_{N-1}	σ_{avg}	N_{obj}	avg	σ_{N-1}	σ_{avg}
$\alpha(1285\text{\AA}, 3023\text{\AA})$								$\alpha(3023\text{\AA}, 5100\text{\AA})$
All	39	−0.676	0.437	0.070	39	0.176	0.464	0.074
high z	12	−0.437	0.342	0.099	12	−0.206	0.365	0.105
low z	27	−0.782	0.438	0.084	27	0.345	0.402	0.077
$\alpha(1285\text{\AA}, 2200\text{\AA})$								$\alpha(4200\text{\AA}, 5100\text{\AA})$
All	39	−0.609	0.449	0.072	39	−0.091	0.833	0.133
high z	12	−0.451	0.404	0.117	12	−0.289	0.551	0.159
low z	27	−0.679	0.457	0.088	27	−0.004	0.927	0.178
$\alpha(1285\text{\AA}, 1460\text{\AA})^a$								$\alpha(4200\text{\AA}, 5100\text{\AA})$
All	39	−0.330	1.091	0.175	39	−0.091	0.833	0.133
high z	12	−0.036	0.465	0.134	12	−0.289	0.551	0.159
low z	26	−0.304	0.981	0.192	27	−0.004	0.927	0.178
<i>t</i> -test				<i>t</i>	P_t			
$\alpha(1285\text{\AA}, 3023\text{\AA})$	vs.	$\alpha(3023\text{\AA}, 5100\text{\AA})$		−8.3	2.5×10^{-12}			
$\alpha(1285\text{\AA}, 2200\text{\AA})$	vs.	$\alpha(4200\text{\AA}, 5100\text{\AA})$		−3.4	1.0×10^{-3}			
$\alpha(1285\text{\AA}, 1460\text{\AA})^a$	vs.	$\alpha(4200\text{\AA}, 5100\text{\AA})$		−0.77	0.45			
K-S test				<i>D</i>	P_D			
$\alpha(1285\text{\AA}, 3023\text{\AA})$	vs.	$\alpha(3023\text{\AA}, 5100\text{\AA})$		0.69	4.4×10^{-9}			
$\alpha(1285\text{\AA}, 2200\text{\AA})$	vs.	$\alpha(4200\text{\AA}, 5100\text{\AA})$		0.49	1.0×10^{-4}			
$\alpha(1285\text{\AA}, 1460\text{\AA})^a$	vs.	$\alpha(4200\text{\AA}, 5100\text{\AA})$		0.16	0.63			

^aStatistics involving α_{23} exclude Q0134 + 329 from the sample.